W. M. Keck Institute for Space Studies Postdoctoral Fellowship Final Report

Nicolas Lee

April 2013 – September 2015

Introduction

The W. M. Keck Institute for Space Studies (KISS) postdoctoral fellowship provided a unique opportunity to pursue my research goals and participate in a wide range of projects. The environment at Caltech and its proximity to JPL fosters a high degree of collaboration, leading to partnerships with other research groups and exposure to their expertise. Additionally, the KISS community played a major role through the availability of workshops, short courses, seminars, and panels on a variety of interesting topics. These events allowed the graduate student and postdoctoral fellows to interact with each other and with many distinguished scientists and engineers.

Research Summary

During my postdoctoral appointment as a member of Professor Sergio Pellegrino's Space Structures Laboratory, my goal was to study enabling technologies for large deployable space systems. To this end, my work focused on three main topics: deployable truss modules for robotic assembly, packaging and deployment of ultra-light membrane structures, and high-voltage low-power electronics design for small satellites.

In-space robotic assembly of modular trusses is a critical technology for the construction of large, rigid space structures. An example of this is the International Space Station, whose primary structure consists of ten truss components launched separately and assembled in low Earth orbit. We collaborated with the Mobility and Robotic Systems section at JPL and with Professor Joel Burdick's research group at Caltech to develop an architecture and conceptual design for a formation-flying, modular space telescope with a primary mirror backplane that is constructed from lightweight hexagonal truss modules [*Lee et al.*, *in prep*; *Hogstrom et al.*, 2014 (attached)]. My contributions to this project included initial trade studies on truss module geometry, prototype construction, and an assessment of space environment effects on the performance of the telescope. Additionally, I developed a design algorithm to prescribe the locations of hexagonal segments over a spherical surface, which is a non-trivial problem because of the effect of variable gap width between segments [*Lee et al.*, 2015 (attached)]. These gaps have an impact on the optical performance of the telescope and on the geometry of the backplane structure.

For space structures that are relatively flat, an attractive option for mass reduction is to construct much of the surface using membranes that can be folded or rolled for efficient packaging during launch. Applications include solar sails and drag sails, which require only a thin membrane, as well as more complicated systems such as patch antenna arrays and solar panels, which may incorporate rigid elements or multiple membrane layers. My work in this area focused on membrane structures with integrated electronics, such as the design of a curved crease pattern for packaging a two-layer membrane antenna array [*Lee and Pellegrino*, 2014a, b (attached)], and structural concepts including antenna and photovoltaic elements for a space-based solar power application [*Arya et al.*, *in prep.*]. A key membrane-packaging concept we explored is the use of a slipping fold that accommodates the thickness of the membrane. Our collaborators for the space-based solar power project include Professors Harry Atwater and Ali Hajimiri and their research groups at Caltech, as well as Northrop Grumman.

A continuing project in our research group is the Autonomous Assembly of a Reconfigurable Space Telescope (AAReST) mission, which will fly several technology demonstrations on a small satellite. A key technology for the reconfigurable space telescope is the use of thin deformable mirrors whose shapes can be adjusted and controlled using an arrangement of piezoelectric elements. My focus within this project was to design, build, and test high-voltage electronic subsystems that drive the piezoelectric elements while satisfying the severe power and volume constraints of the small satellite.

Acknowledgments

First and foremost, I wish to thank the W. M. Keck Institute for Space Studies, Michele Judd, and Tom Prince for supporting my postdoctoral appointment, and Sergio Pellegrino, my postdoctoral advisor, for his guidance. My time at Caltech would not have been as pleasant without the community of KISS fellows and the students and postdocs of the Space Structures Lab with whom I interacted on a daily basis. I would also like to thank the many colleagues at Caltech and JPL who collaborated on projects and proposals, as well as all of the administrative staff at KISS, the International Scholar Services, GALCIT, and EAS who make our work possible.

Refereed Journal Articles

Lee, N. et al., Architecture for robotic in-space assembly of a modular space telescope, *Journal of Astronomical Telescopes, Instruments, and Systems* (*in preparation*).

Arya, M., N. Lee, and S. Pellegrino, Packaging thick membranes with slipping folds for crease-free compaction, *AIAA Journal* (*in preparation*).

Goel, A., N. Lee, and S. Close (2015), Estimation of hypervelocity impact parameters from measurements of optical flash, *Int. J. Impact Eng.*, *84*, 54–63, doi: 10.1016/j.ijimpeng.2015.05.008.

Lee, N., S. Pellegrino, and Y.-H. Wu (2015), A design algorithm for the placement of identical segments in a large spherical mirror, *Journal of Astronomical Telescopes, Instruments, and Systems*, *1*(2), 024002, doi:10.1117/1.JATIS.1.2.024002.

Close, S., I. Linscott, N. Lee, T. Johnson, D. Strauss, A. Goel, D. Lauben, R. Srama, A. Mocker, and S. Bugiel (2013), Detection of electromagnetic pulses produced by hypervelocity micro particle impact plasmas, *Physics of Plasmas*, *20*, 092102, 1–8, doi:10.1063/1.4819777.

Conference Papers

Arya, M., N. Lee, and S. Pellegrino (2016), Ultralight structures for space solar power satellites, *AIAA Space Structures Conference* (*in preparation*).

Arya, M., N. Lee, and S. Pellegrino (2015), Wrapping thick membranes with slipping folds, *AIAA Space Structures Conference*, Kissimmee, FL.

Hogstrom, K., P. Backes, J. Burdick, B. Kennedy, J. Kim, N. Lee, G. Malakhova, R. Mukherjee, S. Pellegrino, Y.-H. Wu (2014), A robotically-assembled 100-meter space telescope, *Proc. IAC*, Toronto, Canada.

Lee, N. and S. Pellegrino (2014), Packaging and deployment strategies for synthetic aperture radar membrane antenna arrays, *URSI-GASS*, Beijing, China.

Tarantino, P., N. Lee, S. Close, and D. Lauben (2014), Faraday Plate Array analysis of hypervelocity impact experiments, *Spacecraft Charging and Technologies Conference*, Pasadena, CA.
Lee, N. and S. Pellegrino (2014), Multi-layered membrane structures with curved creases for smooth packaging and deployment, *AIAA Space Structures Conference*, National Harbor, Maryland.
Lee, N., S. Close, and R. Srama (2013), Composition of plasmas formed from debris impacts on spacecraft surfaces, *Sixth European Conference on Space Debris*, Darmstadt, Germany.

Talks and Posters

Impact plasma measurements using deployable CubeSat sensors, *National Academies Community Symposium on Achieving Science Goals with CubeSats*, Irvine, CA, September 2, 2015.
Asteroid surface resource characterization through plasma analysis of meteoroid impact ejecta, *Stanford Meteor Environment and Effects*, Stanford, CA, July 16, 2015.
In-space robotic assembly of a modular telescope structure, *Caltech Solid Mechanics Symposium*, Caltech, Pasadena, CA, February 13, 2015.
Membrane packaging techniques for space applications, *KNI/MDL Seminar Series*, Caltech, Pasadena, CA, October 7, 2014.
Studying space rocks!, *Summer Science Program*, Socorro, NM, July 14, 2014.
Medicine, meteoroids, and membrane structures, *GALCIT Colloquium*, Pasadena, CA, February 28, 2014.

IAC-14-C2.2.6

A ROBOTICALLY-ASSEMBLED 100-METER SPACE TELESCOPE

Main Author
Ms. Kristina Hogstrom
California Institute of Technology, United States, khogstro@caltech.edu

Co-Authors
Dr. Paul Backes
Caltech/JPL, United States, Paul.G.Backes@jpl.nasa.gov
Prof. Joel Burdick
California Institute of Technology, United States, jwb@robotics.caltech.edu
Mr. Brett Kennedy
Jet Propulsion Laboratory, United States, Brett.A.Kennedy@jpl.nasa.gov
Dr. Junggon Kim
Jet Propulsion Laboratory, United States, Junggon.Kim@jpl.nasa.gov
Dr. Nicolas Lee
California Institute of Technology, United States, nnlee@caltech.edu
Ms. Galina Malakhova
Jet Propulsion Laboratory, United States, Galina.V.Malakhova@jpl.nasa.gov
Dr. Rudranarayan Mukherjee
Jet Propulsion Laboratory, United States, Rudranarayan.M.Mukherjee@jpl.nasa.gov
Prof. Sergio Pellegrino
Caltech/JPL, United States, sergiop@caltech.edu
Mr. Yen-Hung Wu
Jet Propulsion Laboratory, United States, James.Wu@jpl.nasa.gov

The future of astronomy may rely on extremely large space telescopes in order to image Earth-sized exoplanets or study the first stars. In-Space Telescope Assembly Robotics (ISTAR) is a new paradigm for developing large telescopes while overcoming some of the most limiting constraints of current designs. The ISTAR project has developed a concept for an optical space telescope with a collecting area of nearly 8000 m², launched in pieces from the ground, and assembled by a dexterous robot in space. The proposed concept breaks the cost curve by using unique optical layouts, a high degree of modularity, bulk manufactured parts, lightweight structures, and formation flying. Preliminary analysis shows that the design meets high-level optical requirements to yield diffraction-limited images with a wavefront correction system.

This paper focuses on the concept and structural analysis of the telescope. Presented first is the optical scheme, which utilizes a spherical mirror 131 m vertex-to-vertex. Structural requirements are then derived from the limitations of the wavefront control system. The remainder of the paper details the concept of the primary mirror, the largest and most complex component, consisting of two layers: mirror segments and a supporting truss structure. Because the mirror is spherical, every mirror segment is identical, which facilitates a highly modular structure. The 6289 segments in the mirror layer are grouped into 331 *mirror modules,* each containing 19 segments and all associated actuators. Each mirror module is backed by a deployable truss module. The robot builds the mirror by deploying and connecting all truss modules first, then crawling on the resulting stiff surface to place each mirror module. The truss module provides stiffness and support to the mirror, and thus it must be designed to meet and maintain precision requirements under operational loads. The effect of the following loads on the structure are analyzed: fabrication and assembly errors, gravity gradients, thermal effects, and vibrations. A concept of the truss module that meets requirements is derived and presented.

I. INTRODUCTION

The bigger the telescope, the deeper we can probe, the fainter we can detect, the wider we can survey, and thus the better we can understand the universe. In 2018, the James Webb Space Telescope (JWST) is scheduled to become the largest ever built, and concepts for its even bigger successor are already being formulated[1]. At just 6.5 m in aperture diameter, JWST is already too large to fit in a payload fairing in its final configuration, and must instead be assembled on Earth, folded for launch, and unfolded in space. The most innovative foldable concepts, like DARPA's MOIRE and NASA's

ATLAST, are sized at the 20 m range[2, 3]. The achievable size of deployable telescopes is then strictly limited by the size of the payload fairing. While advances in lightweight and flexible materials can push this limit, folding up and deploying a telescope many times larger may not be realistic. The progression of space telescopes thus necessitates a new strategy.

One solution is In-Space Telescope Assembly Robotics (ISTAR). To reach larger scales, the telescope can be assembled in space, rather than on the ground, no longer limiting the aperture size by launch capacity. The ISTAR concept presented here outlines an architecture for a robotically-assembled optical space telescope that can reach up to the 100-m class. The architecture is entirely modular, enabling an expandable and evolvable system that can be suited to meet a range of missions and aperture sizes. This paper is focused on the development and feasibility of the 100-m class telescope to stretch the limits of the architecture. The complexity of constructing a large aperture is addressed through symmetry and modularity in the structure and use of robotic assembly. The concept is based on a set of precision requirements and correction methods using currently available technology. In this paper, the concept of the primary mirror, the largest component of the system, is described in detail, including component design and assembly plan. Preliminary structural and thermal analyses demonstrate that the precision requirements can be met.

II. TELESCOPE CONCEPT

II.I Observatory Components

The ISTAR concept is a segmented, steerable, UV to near IR telescope robotically assembled in space. Fig. 1 shows the basic layout of the telescope and its four main components: the sunshade, primary mirror, Spherical Aberration Corrector (SAC) unit, and metrology system. Given the large size of the telescope, each of these components is structurally separate and formation flown. Each component is a self-contained unit with its own power, thermal control, and propulsion system that maintains formation.

The optical design borrows from that of the ground-based Hobby-Eberly Telescope (HET) and Southern African Large Telescope (SALT) by utilizing a spherical

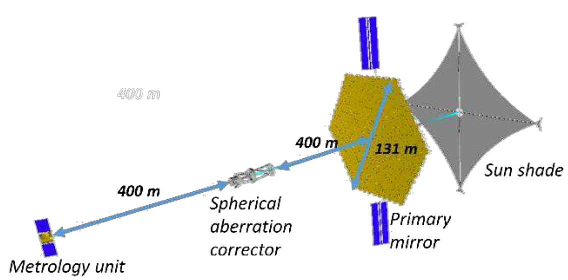

Fig. 1: Diagram of ISTAR optical scheme.

curvature primary mirror[4, 5]. The primary mirror acts as a "precision light bucket", and is phased into a diffraction-limited telescope at the exit pupil inside the SAC using a technique described in Reference 6. One key advantage of this design is that the majority of the wavefront sensing and control (WFSC) and the only active deformable mirrors are offloaded from the primary mirror to the much smaller optics in the SAC. The primary mirror segments are identical, manufactured in bulk, and only require tip-tilt control, sharply reducing mirror fabrication costs, which is one of the most significant cost drivers in observatories. The SAC mirror segments have the same basic characteristics, but are deformable with μm-level actuation range and correctable down to nm-level. The baseline mirror segments are drawn from currently available technology, and are assumed to have a hexagonal shape with vertex-to-vertex length of 1.35 m. Because the segments are hexagonal, the full primary mirror will also be approximately hexagonal. The primary mirror parameters are summarized in Table 1. The light-collecting area is equal to that of a 97.3-m filled circular aperture.

Vertex-to-vertex length [m]	131.88
Light collecting area [m^2]	7444
Radius of curvature [m]	800
Number of segments	6289
Segment vertex-to-vertex length [m]	1.35
Total areal density [$\mathrm{kg/m}^2$]	< 30
Field of view [arc minutes]	4.2x4.2

Table 1: Primary mirror (M1) parameters.

Structurally connected to the primary mirror is also the driving spacecraft and two solar panels similar to the ones used on the International Space Station, as determined by a preliminary power budget. The solar panels are connected to the spacecraft, which is located below the primary mirror in the center. The fully assembled unit is shown in Fig. 2.

Fig. 2: Fully assembled primary mirror with central spacecraft and solar panels.

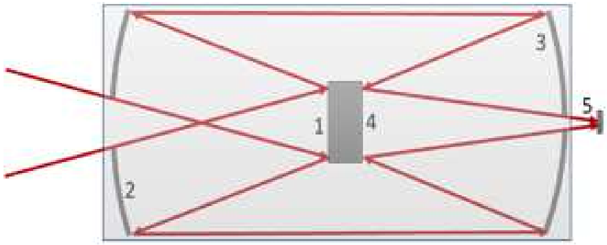

Fig. 4: Ray trace diagram of the SAC.

The SAC is located halfway to the center of curvature of the primary mirror, for a separation distance of 400 m. It includes two 8.6-m clamshell aspheric mirrors, separated by 24.4 m. A ray trace diagram is shown in Fig. 4. Another major advantage of the spherical aperture is that the SAC can be moved relative to the primary mirror to observe a new target within a 7.16 deg field of regard without having to move the massive primary mirror. This enables rapid transition to a new observation without the overhead of time and fuel otherwise required to slew the primary mirror and wait for its dynamics to settle. The locus of motion of the SAC with respect to the primary mirror is a spherical surface of 400-m radius of curvature and 50-m diameter, as shown in Fig. 5. In the nominal position, the SAC is at the center and the entire primary mirror is visible. However, when it is moved to the limit of its range of motion, only about 40% of the primary can be seen, as shown in Fig. 3.

The metrology system is located at the center of curvature of the mirror. It contains a Zernike wavefront sensor and an Array Hetroydyne Interferometer to precisely measure the shape and phase of the primary mirror segments.

The sun shade design borrows from deployable solar sails such as Sunjammer, which is 38 m square and is scheduled to be launched in 2015[7]. Four deployable masts extend from a central hub radially outward, carrying the corners of the sun shade to a full distance of 70 m, as shown in Fig. 6. The Shuttle Radar Topology Mission, launched in 2000, used a 60-m mast built by ATK[8]. Thus, 70 m appears feasible with current

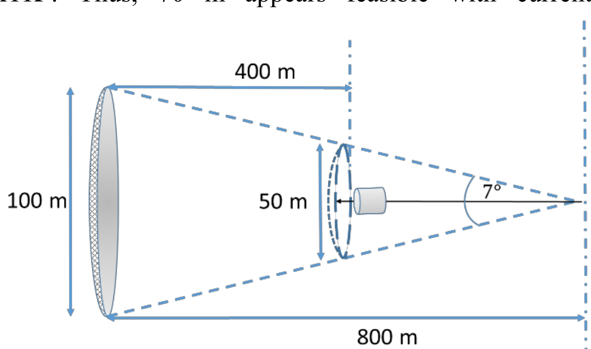

Fig. 5: Sketch highlighting the eyepiece motion required to point to a new target without slewing the primary mirror.

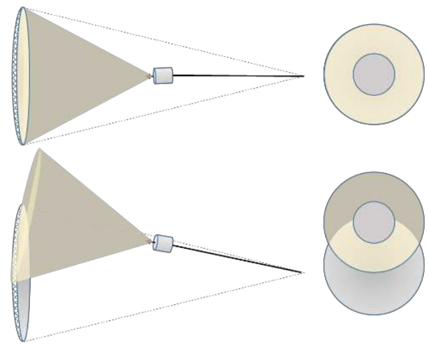

Fig. 3: Diagram of what portion of the primary mirror the eyepiece sees when it is at the center (top) and 3.5 deg from center. A side view of the telescope is shown left and a top view is shown right.

technology. The shade membrane will be chosen based on thermal constraints described in Section IV.III.

II.II Primary Mirror Assembly Plan

The primary mirror is the largest component of the telescope and thus the focus of robotic assembly. A representation of the ISTAR robot needed to assemble the mirror is shown in Fig. 8. The robot will be commanded from Earth, but with significant on-board autonomy to minimize the bandwidth of communications to a human operator. The resulting supervised autonomy system will enable the Earth-based operator to specify high-level commands, while the robot performs all sensor-based motion and complex tasks autonomously.

Drawing upon the development of the Lemur and RoboSimian robots at JPL, the ISTAR robot is anticipated to have six appendages [9, 10]. During assembly, two of these appendages can be used for dexterous manipulation while the other appendages remain attached to the structure. All six appendages can be used to walk on the structure. Perception and dexterous manipulation

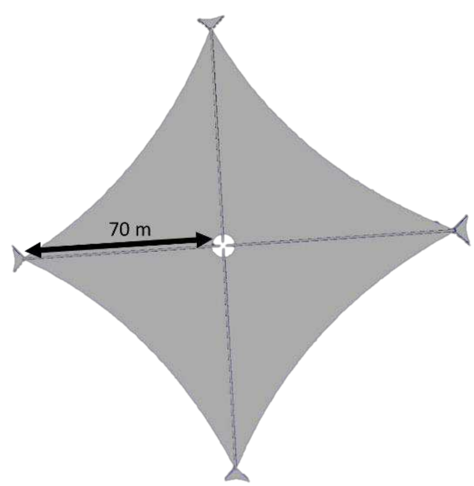

Fig. 6: Model of the sun shade.

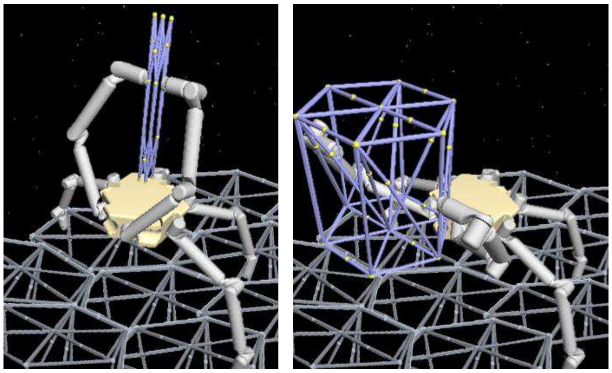

Fig. 8: Depiction of robot deploying a truss module.

technologies that will be needed have been demonstrated in a laboratory environment at JPL[11]. The robot is battery powered and can be charged from the primary mirror power grid.

The primary mirror consists of two layers: the mirror segments, which includes rigid body actuators and electronics, and a supporting truss structure. Because the primary mirror is spherical, all mirror segments are identical, which enables a highly modular structure. Groups of segments and their actuators are hexagonally packed into a cluster called a *mirror module*. Each mirror module is backed by a rigid plate which features structural and power connectors. Given the complexity and fragility of the segments and associated electronics, mirror modules are assembled on the ground by humans and launched as a package.

The truss layer is broken down into hexagonal *truss modules,* which are deployable structures sized to match one mirror module when fully deployed but can stow compactly for launch using internal hinges. An assembled mirror module and truss module are shown in Fig. 9. Each truss module is equipped with structural and power connectors located at the ends of each vertical member, with internal wiring throughout the members to transmit power. These connectors are structurally adjustable by the robot to ensure proper alignment between modules. The vertices of the main face of each

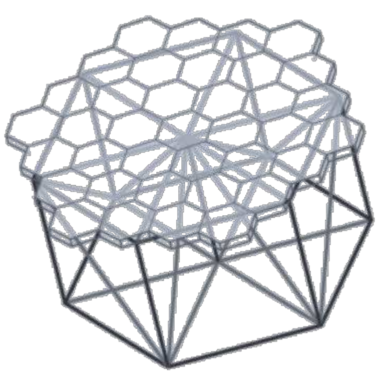

Fig. 9: Mirror module atop truss module.

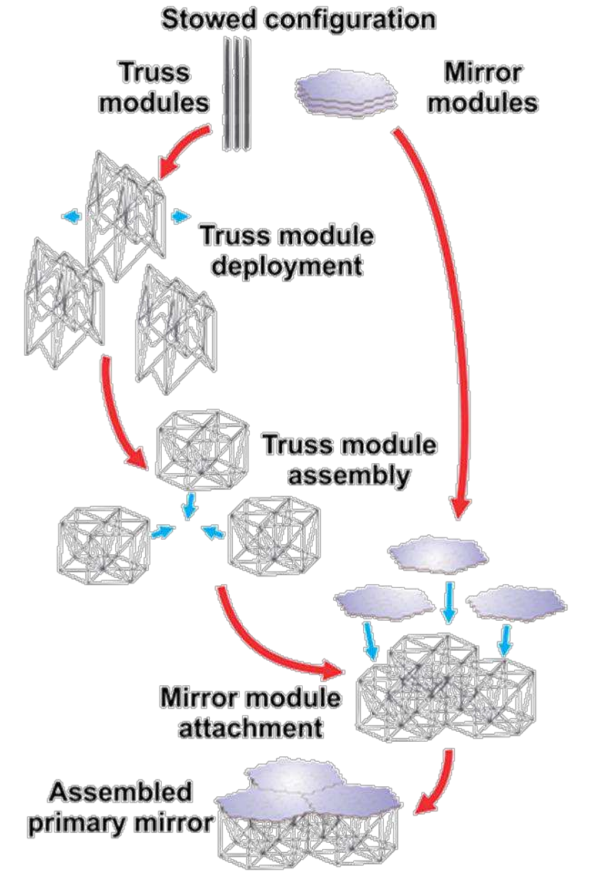

Fig. 7: Assembly concept showing how the truss modules and mirror modules are stowed for launch and assembled robotically in space.

module also features ball-like features which the robot can grasp while walking.

In space, the robot retrieves the first folded truss module from a central canister and deploys it so that the internal hinges lock. The robot then attaches the truss module at the connection points to a central hub that is rigidly mounted and wired to the spacecraft and solar panels. The robot then continues to assemble truss modules in concentric rings around the central hub. After each ring is assembled, a metrological measurement is made to check the assembly for adherence to alignment tolerances. The robot then uses this measurement to adjust the connectors and complete the ring. This pattern is repeated until the entire truss is built.

Once the truss is complete, the robot begins assembling mirror modules. The robot interfaces with the mirror module through the rigid plate, avoiding the sensitive mirror segments. In the same concentric ring pattern, the robot assembles mirror modules by attaching them to the underlying truss. Mirror modules are connected only to the truss, not to each other, to avoid stress build-up. The module assembly process is summarized in Fig. 7.

It is unlikely that truss modules will need to be serviced. However, mirror segments are sensitive and may encounter issues (e.g. meteoroid hits). Servicing of individual segments may be too complex for the robot, so instead the entire mirror module can be replaced. The connectors that attach the module to the truss will also be able to detach from the truss as needed.

II.III Mission Requirements

The wavefront sensing and control system has three levels of correction. First, as mentioned in the assembly concept, the truss will be robotically adjustable during construction. This corrects for fabrication and assembly errors. Second, the primary mirror segments are backed by rigid body actuators for removing quasistatic errors such as thermal loads. Finally, the active mirrors in the SAC remove any additional effects, including dynamic errors. The correction levels, defined below, are consistent with the current state-of-the-art.

- Robotic truss adjustment: 30 mm to 3 mm
- Rigid body actuators: 10 mm to μm -level
- Active mirrors: μm -level to nm-level
    - Also corrects up to 240 mm of change in radius of curvature

The telescope design must ensure that errors remain within the range of correction.

Along with the precision requirements, the following other functional requirements must be met:

- The telescope shall be functional no more than three minutes after a slew maneuver.
- The telescope shall operate at temperatures between 240 K and 300 K.
- The primary mirror shall have an areal density less than $30\,\mathrm{kg/m^2}$. Since the mirror segments and actuators have a density of $25\,\mathrm{kg/m^2}$, this leaves $5\,\mathrm{kg/m^2}$ for the truss.
- Mirror segments shall have a gap of 100 ± 10 mm to facilitate the ball-like features that the robot uses to walk on the mirror surface.
- The telescope shall nominally operate in a geosynchronous orbit (GEO).

The ISTAR baseline to operate at GEO was chosen with the expectation the telescope would then also be suited for Lagrange point operation with few modifications, because the environment at GEO is more severe and thus produces more stringent design requirements.

The most customized parts of the architecture are the truss and mirror modules. Their design, described in the remainder of the paper, is based on these requirements.

III. MIRROR MODULE DESIGN

The mirror modules are all identical. Their geometry is based on the following key considerations:

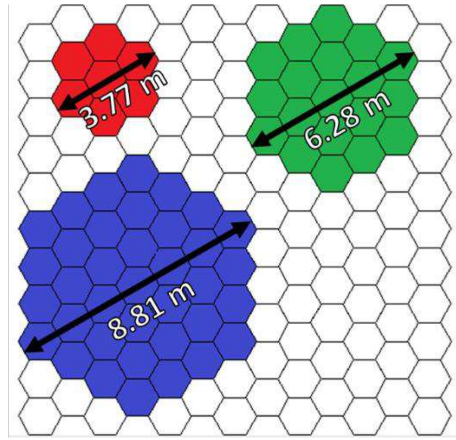

Fig. 10: Choices of number of mirror segments per mirror module.

- The module contains n identical, spherical mirror segments arranged according to a hexagonal tessellation.
- The value of n is chosen to be as large as possible to maximize launch capacity so that the modules can be stacked inside a payload fairing.
- The gaps between the mirror segments are 100 ± 10 mm to facilitate robotic mobility, as stated in Section II.III.
- The gap size between segments must vary to allow the hexagonal segments to lie on a spherical surface.

Fig. 10 shows three choices for n: 7, 19, and 37 segments. With the nominal 100-mm gap between segments, these designs yield maximum mirror module dimensions of 3.77 m, 6.28 m, and 8.81 m respectively. Since the proposed SLS launch vehicle will have a payload fairing with an outer diameter of 8.4 m, the $n = 19$ design was chosen[12]. With 6289 segments total, this design yields 331 mirror modules. Given their $25\,\mathrm{kg/m^2}$ areal density, the total mass of the mirrors and actuators is then 145,300 kg.

The curvature of the mirror requires variable gap sizes between the mirror segments. The distribution of the gap size is a design parameter that has been studied in detail. An algorithm to place the segments on a spherical surface while imposing different constraints on the gap variations was developed[13]. A solution was obtained in which the gap sizes between mirror segments *within a mirror module* vary by no more than 1.7 μm, with the distribution being *identical* for all mirror modules. The gaps between one mirror module and another mirror module were also minimized with this solution, with values ranging from 98 mm to 101.3 mm. This result is well within the required tolerance of $\pm$ 10 mm.

The mirror modules will be assembled on the ground, incorporating the variable gap distribution that has been calculated. The variation in the larger gaps between

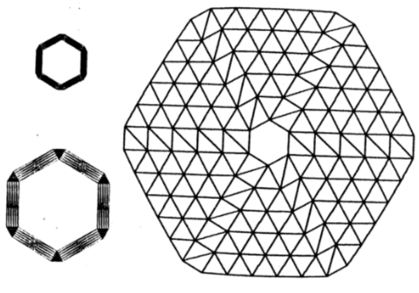

Fig. 11: Deployment of 20-meter hybrid Pactruss, deploying around a central hub[14].

modules will be created by the robot using the adjustable connectors on the truss modules described in Section II.II. Note that the gaps between the modules increase linearly with depth through the truss thickness, and hence will be larger on the back side of the truss than on the front. However, because the radius of curvature is much larger than the depth of the truss, the difference is still well within the range of the adjustable connectors.

IV. TRUSS MODULE DESIGN

The truss geometry must facilitate a compact storage profile and a smooth deployment. A modified version of the Pactruss deployment scheme has been selected. Pactruss was developed by Aerospace Corporation specifically for large precision telescope structures[14]. It was originally intended to provide an entirely deployable telescope backing structure, consisting of many triangular unit cells simultaneously unfolding. One flavor of the deployment scheme is shown in Fig. 11. This design was analyzed to show that it could maintain sub-micron precision under operational loads when fully deployed. However, there were issues in the deployment simulations controlling the order in which the many hinges were locked[14]. The ISTAR concept removes this uncertainty because only one hexagonal unit cell is required for the truss module, greatly reducing the

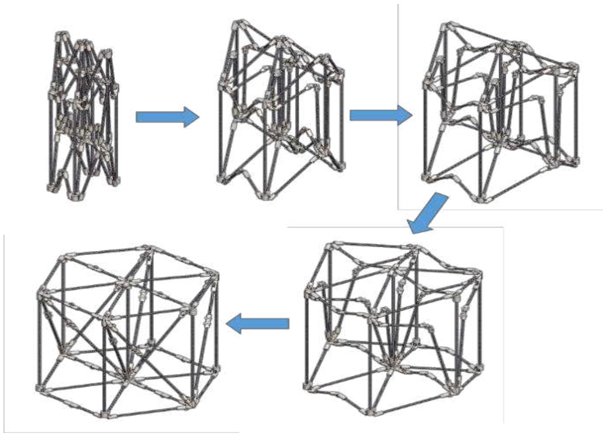

Fig. 12: Truss module deployment.

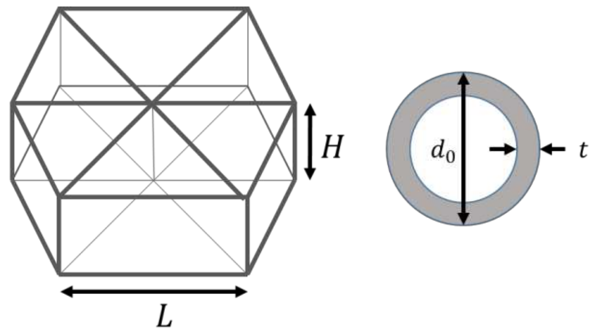

Fig. 13: Geometry variables of truss module, with the member cross-section shown right.

number of hinges that act simultaneously. The module and deployment scheme are shown in Fig. 12. The unit cell consists of 39 members: the 12 longerons that make the hexagonal face on each side (24 total), 7 verticals, 4 face diagonals, and 4 internal diagonals. The diagonals and 8 longerons are hinged in the center. In the compact state, the truss module folds like an umbrella, and thus the stowage footprint is determined by the hinge offsets and the outer diameter of the members.

The truss module dimensions are defined in Fig. 13. In order to reduce the number of redundant members, the truss modules are rotated with respect to the mirror modules, rather than hexagonally packed, as shown in Fig. 14. The value of the side length L must match this tesellation pattern, governed by the mirror module size. For $n = 19$ as chosen, $L = 2.6$ m.

M55J carbon fiber composite has been selected for the truss material, because of its high stiffness and low density[15]. The truss depth, H, and member cross-section properties, d_o and t, control the structural response to external loads, and thus must be chosen to ensure that all of the precision requirements for the primary mirror are met.

It is not known which source of shape error is in general the most demanding for a large space telescope. Thus, to determine the specific values of the design variables of the truss module, it is necessary to consider

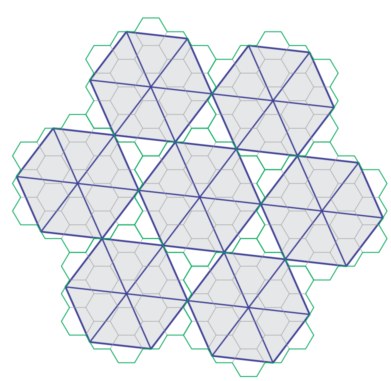

Fig. 14: Depiction of mirror module tiling (green outline) vs. truss module tiling (purple outline).

separately the requirements associated with each specific error source.

IV.I Fabrication and Assembly Errors

The fabrication and assembly errors must not exceed 30 mm (see Section II.III). The accuracy with which the truss can be built is currently unknown, as the joints, hinges, and connectors in the truss have yet to be designed, and the manipulation capabilities of the robot are not known in detail. Hence, assembly errors on the level of 10 mm, 1 mm, and 0.1 mm were considered to estimate the accuracy level needed to meet the 30 mm precision requirement. These errors were treated as length changes, δl, in the members of the truss to represent fabrication errors or slide in the hinges. A pin-jointed model of the truss was built in MATLAB. Each member was assigned a δl value from a random uniform distribution with maximum amplitude given by the accuracy level. The resulting displacements were computed and this process was repeated 10 times for each accuracy level to obtain average and maximum values.

IV.II Gravity Gradient

Gravity gradients arise when one part of the telescope is closer to the Earth than another part. This effect is negligible for small telescopes, but becomes more significant for larger Earth-orbiting telescopes. Gravity gradients cause quasi-static errors in the mirror figure, and thus the resulting distortion magnitude cannot exceed 10 mm, as discussed in Section II.III.

The magnitude of the gravity gradient distortion on the primary mirror depends on its orientation with respect to the Earth. The maximum gravity gradient occurs when the mirror is oriented radially along the line of gravity, as shown left in Fig. 15, causing an axial distortion. However, the truss is much stiffer axially than in bending, and thus other orientations that have less of a gravity gradient may still have greater distortion.

In general, the distorting force on any node within the primary mirror comes from the difference between the gravitational force and the centrifugal force, which is set by the orbit. If the vector between the center of mass of the mirror and the center of the Earth is $\boldsymbol{r}$, then the centrifugal force, $\boldsymbol{F_c}$, on a node i of mass m_i is given by:

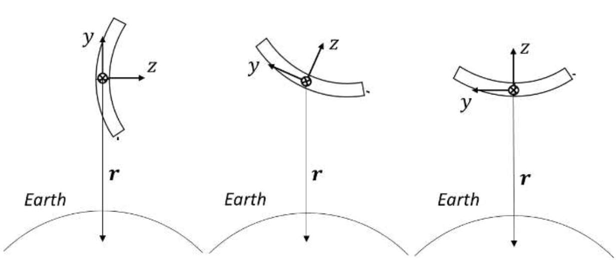

Fig. 15: Orientation of the primary mirror with maximum gravity gradient (left), intermediate gravity gradient (middle), and minimum gravity gradient (right).

$$\boldsymbol{F_c} = \frac{\mu m_i \boldsymbol{r}}{||\boldsymbol{r}||^3} \quad [1]$$

Letting $\boldsymbol{u_i}$ be the vector between the center of mass and the node i, the gravitational force, $\boldsymbol{F_g}$, is given by:

$$\boldsymbol{F_g} = \frac{\mu m_i (\boldsymbol{r} - \boldsymbol{u_i})}{||\boldsymbol{r} - \boldsymbol{u_i}||^3} \quad [2]$$

$\boldsymbol{F_{dist}}$ is then the difference between these forces.

The distortions due to gravity gradient loads were computed from a finite element model of the primary mirror structure, consisting of pin-jointed elements and lumped masses distributed throughout the top surface to represent the mass of the mirrors and actuators. The nodes associated with the center module were fixed. The mass matrix for the entire model was computed and the mass associated with each node was used to calculate the gravity gradient loads. The depth and member cross-section were varied until an acceptable solution was found.

IV.III Thermal Analysis

The bulk thermal requirement is that the primary mirror must operate at 270 ± 30 K, as stated in Section II.III. However, one of the most detrimental thermal effects is a change in curvature of the primary mirror, which arises from a temperature difference through the mirror thickness, or from the mirror surface to the backside of the truss. The rigid body actuators, with a range of 10 mm, can correct for this type of error. In addition, the wavefront control in the eyepiece can counteract 240 mm of additional change in the radius of curvature from the nominal 800 m.

When the curvature changes, the *sag* of the mirror changes. The sag x is the height difference between the mirror edge and mirror center, as shown in Fig. 16. The aperture diameter D is defined in this picture as an arclength on the circle of radius R that subtends angle ϕ. This is to ensure that, as R changes, the length of the mirror neutral axis stays constant. If ϕ is small (only about 3.5 ° in the nominal case), the sag x is approximately $(D/2)^2/(2R)$. The rigid body actuators can account for change in sag dx of 10 mm. Given that the average diameter of the hexagon is about $D = 122$ m,

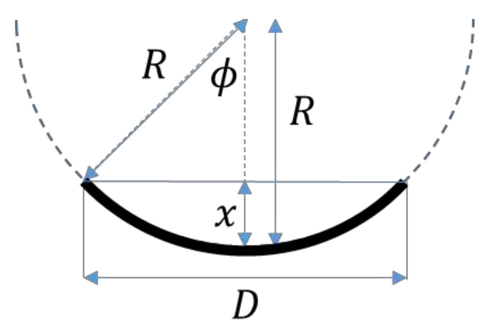

Fig. 16: Definition of the sag value x. D is the arclength defined by angle ϕ on the circle of radius R.

the maximum change in curvature ΔK that can be removed by the rigid body actuators is given by:

$$\Delta K = \Delta(1/R) = \frac{2dx}{\left(\frac{D}{2}\right)^2} = 5.37 \times 10^{-6}\mathrm{m}^{-1} \quad [3]$$

The wavefront correction system can account for an additional curvature change of $\Delta K = \Delta(1/R) = (1/800\text{ m} - 1/800.240\text{ m}) = 3.74 \times 10^{-7}\mathrm{m}^{-1}$. Thus the total allowable curvature change is $\Delta K_{max} = 5.70 \times 10^{-6}\ \mathrm{m}^{-1}$.

The curvature is then related to the temperature differential by the truss depth H and material expansion coefficient α_{TRUSS}:

$$\Delta T_{max} = \frac{\Delta K_{max} H}{\alpha_{TRUSS}} \quad [4]$$

Given $\alpha_{TRUSS} = 1.1 \times 10^{-6}/°\mathrm{C}$ for M55J carbon fiber composite and the curvature change obtained above, Equation [4] yields the maximum allowable temperature difference in terms of the truss depth, $\Delta T_{max} = 5.23 \cdot H$ [°C].

In GEO, there are three distinct thermal environments, shown in Fig. 18. The temperature gradient in each case was estimated using energy balance on a simple thermal model. Fig. 17 shows a module of the model, where surface 1 is the mirror surface and surface 2 is the back surface of the truss, consisting of a triangular tessellation of members with large gaps in between them.

In case 1, the telescope is pointed at the Earth with the Sun behind the sun shade. Surface 2 receives heat from the Sun that leaks through the sun shade. Surface 1 receives heat from the Earth's surface radiation and albedo reflection from the Sun, as well as heat from the Sun that leaks through the sun shade and is not blocked by Surface 2. In addition, both surfaces exchange heat through radiation and conduction. By defining each of these inputs, the temperatures of both surfaces were found from the energy balance. The geometric parameters of the truss, the optical properties of the materials, and the fraction of heat blocked by the sun shade were varied until the temperatures were within 270 ± 30 K and the difference between the temperatures was less than the requirement. The full energy balance derivation can be found in Appendix A.

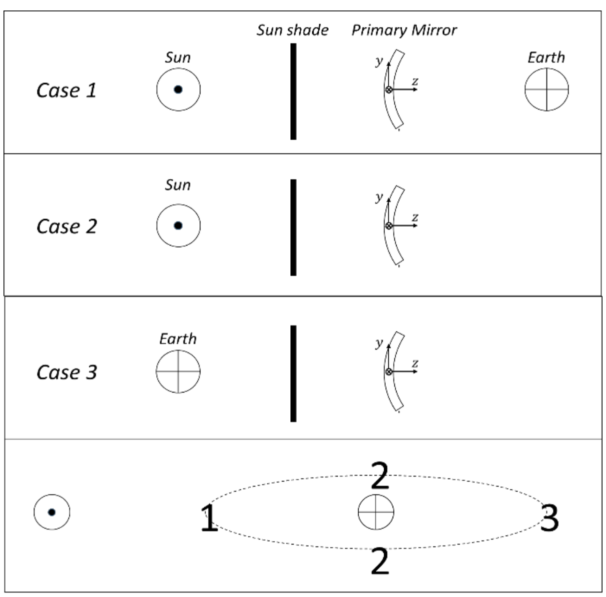

Fig. 18: GEO thermal environment cases. Case 3 represents the eclipse condition.

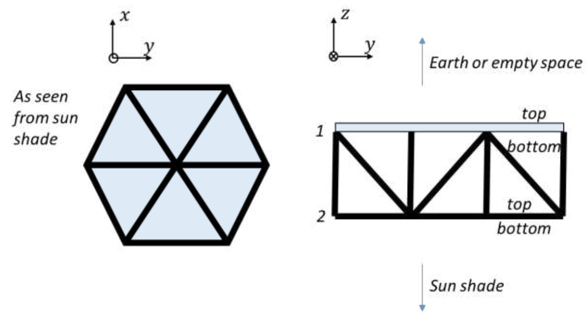

Fig. 17: Thermal model of one module of primary mirror.

IV.IV Dynamics

It is assumed that, in order to passively reject vibrations and maintain the required dynamic precision of 1 μm, the fundamental frequency must be higher than the frequency of vibrations. One of the major sources of vibrations are reaction wheels. From Reference 16, the requirement on the fundamental frequency of the structure to reject reaction wheel disturbances is given by:

$$f_0 > \begin{cases} f_c\sqrt{v_c - 1}, & v_c \geq 1 \\ f_c, & v_c < 1 \end{cases} \qquad v_c = \frac{n_{RWA} U_s}{2\zeta M_{total}\delta_{max}} \quad [5]$$

where f_0 is the telescope fundamental frequency, f_c is the cut-off frequency of the isolation system, n_{RWA} is the number of reaction wheels, U_s is the static reaction wheel imbalance, ζ is the damping coefficient, M_{total} is the total mass of the telescope and spacecraft, and δ_{max} is the maximum allowable deformation.

In the present case, δ_{max} =1 μm, and the damping coefficient was conservatively chosen as 0.005. Reference 16 states that a typical value for U_s is $5 \times 10^{-6}\mathrm{kg} \cdot \mathrm{m}$. It can be assumed that $v_c < 1$, and the fundamental frequency of the structure only needs to exceed the isolation cut-off frequency in order to maintain precision under reaction wheel imbalance loads. Isolation systems can achieve cut-off frequencies on the order of 0.1 Hz[17].

There are many other possible sources of vibrations on the spacecraft, such as the mirror actuators and joint settling. Control moment gyros may also be used instead of reaction wheels, which will have different vibration characteristics. Rather than addressing each source individually, it is practical to assume a spectrum of random vibrations. The minimum fundamental frequency to reject random disturbances is given by:

$$f_0 > \frac{1}{2\pi}\left(\frac{G_0}{8\zeta\delta_{max}^2}\right)^{\frac{1}{3}} \quad [6]$$

where G_0 is the RMS amplitude of the disturbance power spectral density over the bandwidth of their frequencies[17]. Assuming a $1\mu g$ amplitude and a 0-100 Hz bandwidth, $G_0 = (9.8 \times 10^{-6}\,\mathrm{m/s^2})^2/100\,\mathrm{Hz} = 9.6 \times 10^{-13}\,\mathrm{m^2/s^3}$, which yields a minimum fundamental frequency of the telescope of 0.459 Hz.

Finally, one functional requirement is that the telescope shall be usable no more than three minutes after a slew maneuver. The exact response of the structure to a slew maneuver depends on the torque profile, the propulsion system, and other parameters not specified at this design stage. However, the settling time T_s required for structural distortions to fall below 2% of the initial distortion amplitude can be estimated by considering a single-degree-of-freedom system: $T_s = 3.9/\zeta\omega_0$, where $\omega_0 = 2\pi f_0$. Again assuming $\zeta = 0.005$ and requiring that $T_s < 3$ minutes implies that the fundamental frequency must be larger than 0.69 Hz, which is the most stringent dynamic requirement.

The fundamental frequency was estimated from the finite element model described in Section IV.II.

IV.V Analysis Results

After an iterative process that included each of the loading types outlined above, the design converged to the parameters presented in Table 2.

Truss side length, L [m]	2.6
Truss depth, H [m]	2.6
Member outer diameter, d_o [mm]	45
Member wall thickness, t [mm]	3
Truss areal density [kg/m^2]	4.01
Truss mass [kg]	23352
Primary mirror mass [kg]	168690

Table 2: Truss module design parameters

Firstly, as described in Section II.III, the truss areal density is confined to less than $5\,\mathrm{kg/m^2}$. This requirement is met with a margin of $1\,\mathrm{kg/m^2}$, which may be allotted to the mass of the truss hinges and connectors. This design has a fundamental frequency of 1.0 Hz, which satisfies the dynamic requirements with a good margin. Despite the size of the telescope, the effect of gravity gradient was still negligible. The maximum distortion occurred when the mirror was oriented approximately 45 deg to the line of gravity (as roughly shown middle in Fig. 15), but this distortion did not exceed 46 nm.

Assembly errors on the level of 10 mm, 1 mm, and 0.1 mm were applied to the truss. The resulting distortions of the truss were computed to obtain the RMS and maximum distortion on the mirror surface in the direction normal to the curvature, as well as the RMS and maximum overall distortion, which are shown in Table 3. The maximum distortions indicate that the input error can be greatly amplified in the structure, in some cases by a factor of almost six, demonstrating the effect of error build-up. It follows that, in order to meet the maximum 30-mm requirement, the structure must be built to a precision of at least 5 mm.

Error level	10	1	0.1
RMS Surface Distortion	92.51	0.91	0.12
Max Surface Distortion	55.70	1.56	0.69
RMS Total Distortion	9.73	0.96	0.12
Max Total Distortion	57.10	5.63	0.71

Table 3: Results of fabrication error analysis. The units are all in millimeters.

From Equation [4], given $H = 2.6$ meters, the maximum allowable temperature difference through the truss thickness is $\Delta T = 13.59$ K. The thermal analysis was performed using the parameters given in Table 4, where α_i and ε_i are the absorptivity and emissivity of surface i respectively, which can vary between the top and bottom of the surface (refer to Fig. 17).

Solar flux $\dot{q}_{solar}$ [W/m^2]	1370
Earth surface heat flux $\dot{q}_{IR}$ [W/m^2]	237
Earth albedo a	0.3
Orbit altitude A_{orbit} [m]	35786
Earth radius R_E [m]	6378
$\alpha_{1,top}$ (Polished aluminum)	0.02
$\alpha_{1,bottom}$ (Paint)	0.6
$\alpha_{2,top} = \alpha_{2.bottom}$ (CFC)	0.96
$\varepsilon_{1,top}$ (Polished aluminum)	0.03
$\varepsilon_{1,bottom}$ (Paint)	0.87
$\varepsilon_{2,top} = \varepsilon_{2.bottom}$ (CFC)	0.88
CFC thermal conductivity k [W/m]	156
Fraction of solar flux blocked by shade γ	0.6

Table 4: Parameters used in thermal analysis. CFC stands for carbon fiber composite, assumed to be roughly matte black.

Note that the bottom of the mirror modules is coated with flat colored (red, green, or brown) paint to yield the desired optical properties, while the truss maintains the optical and thermal properties associated with black carbon fiber composite. The resulting temperatures of T_1 and T_2 for the three different environmental cases are shown in Table 5.

	T_1 [K]	T_2 [K]	ΔT [K]
Case 1	278.03	273.29	4.74
Case 2	277.96	273.26	4.70
Case 3	89.21	86.59	2.62

Table 5: Thermal analysis results.

The bulk temperature constraint of 270 ± 30 K is maintained in only two of the cases; the thermal analysis shows that the telescope will not be able to operate when it is eclipsed by the Earth. In GEO, eclipses only occur during 3 months of the year, lasting 72 minutes at maximum, so this is an acceptable mission constraint. When not eclipsed, a modest sun shade blockage factor of $\gamma = 0.6$ keeps the primary mirror within temperature bounds and with an acceptable gradient through the truss thickness to maintain precision requirements. The material of the sunshade will have to be chosen to obtain this blockage factor.

V. SUMMARY

This paper has outlined a solution for 100-m optical telescope that is robotically assembled. The concept breaks the cost curve by utilizing an optical design with a spherical primary mirror. The shape allows for the wavefront sensing and control system to be offloaded to an eyepiece, so that the primary mirror segments can be inactive and identical, sharply reducing the cost of the control system and mirror fabrication. The assembly process of the primary mirror efficiently balances deployable structures with robotic operations. The primary mirror is broken down into groups of mirror segments called mirror modules, backed by separate deployable truss modules. In orbit, the robot deploys and assembles the truss around a central hub connected to a spacecraft, then attaches the mirror modules to the truss. The mirror modules have been sized to fit in the proposed SLS payload fairing. The truss modules provide stiffness and support to the mirror surface. Preliminary structural and thermal analyses have been performed to design the truss module and demonstrate that it can provide precision levels within the range of the wavefront correction system to yield diffraction-limited images. Some important parameters of the telescope are summarized by Table 6.

The telescope presented here is currently in the concept stage. Results so far are promising, and work is ongoing to bring the concept to a higher level of maturity. This includes better characterization of the metrology, eyepiece, and sun shade, as well as continued development of the structural components and robotic assembly.

VI. ACKNOWLEDGEMENTS

The research was carried out in part at the Jet Propulsion Laboratory, California Institute of Technology, under a contract with the National Aeronautics and Space Administration. Part of this work was supported by the NASA Space Technology Research Fellowship #NNX13AL67H.

Primary Mirror vertex-to-vertex (V2V) length [m]	131.88
Light collecting area [m^2]	7444
Radius of curvature [m]	800
Field of view [arc min]	4.2x4.2
Field of regard [deg]	17.6
SAC to primary mirror distance [m]	400
SAC largest mirror dimension [m]	8.6
SAC clamshell mirror separation [m]	24.4
Number of primary mirror segments	6289
Number of mirror modules	331
Number of truss modules	331
Number of concentric rings	10
Mirror segment V2V length [m]	1.35
Truss module V2V length [m]	5.2
Mirror module V2V length [m]	6.28
Mirror segment aerial density [kg/m^2]	25
Truss aerial density [kg/m^2]	4.01
Sunshade diagonal dimension [m]	140
Operating temperature [K]	240-300
Sunshade blockage factor	0.6
Truss module mass [kg]	70.54
Mirror module mass [kg]	439.0
Truss member outer diameter [mm]	45
Truss member wall thickness [mm]	3
Truss module depth [m]	2.6

Table 6: Important parameters of the ISTAR telescope concept

APPENDIX A. THERMAL ENERGY BALANCE

The energy balance equations will be developed here for case 1, since all factors are present. Equations for case 2 and 3 can be derived by removing and rearranging the appropriate terms. In general, the balance for case 1 is as shown in Equation [7].

Surface 1:

$$\dot{Q}_{IR} + \dot{Q}_a + \dot{Q}_{1,SS} - \dot{Q}_{cond,1\to 2} - \dot{Q}_{rad,1\to 2} - \dot{Q}_{1,out} = 0 \qquad [7]$$

Surface 2:

$$\dot{Q}_{2,SS} + \dot{Q}_{cond,1\to 2} + \dot{Q}_{rad,1\to 2} - \dot{Q}_{1,out} = 0$$

$\dot{Q}_{IR}$	:=	heat from Earth internal radiation incident upon surface 1
$\dot{Q}_a$	:=	heat from Earth albedo reflection incident upon surface 1
$\dot{Q}_{cond,1\to 2}$	:=	heat conducted from surface 1 to surface 2

$\dot{Q}_{rad,1\to 2}$	:=	heat radiated from surface 1 to surface 2
$\dot{Q}_{1,SS}$	:=	heat from Sun leaking through the shade and incident upon surface 1
$\dot{Q}_{2,SS}$	:=	heat from Sun leaking through the shade and incident upon surface 2
$\dot{Q}_{1,out}$	:=	heat radiating from surface 1 to space
$\dot{Q}_{2,out}$	:=	heat radiating from surface 2 to space

Note that heat leaking through the sun shade can be incident upon surface 1 through the gaps between the truss members.

Each surface i has area A_i, with top and bottom emissivity and absorptivity of $\varepsilon_{i,top}$, $\varepsilon_{i,bottom}$, $\alpha_{i,top}$, and $\alpha_{i,top}$ respectvely. The total area of the top surface A_1 is equal to the number of modules n_m multiplied by the area of one module with side length L. The area of surface 2 is only the projected area of the truss members arranged in the triangular pattern shown left in Fig. 17. Each Module has 12 surface members with outer diameter d_0 and length L. A_1 and A_2 are given by:

$$A_1 = n_m \frac{3\sqrt{3}}{2} L^2 \quad [8]$$
$$A_2 = n_m(12 d_0 L)$$

Given this geometry, the external heat fluxes are:

$$\dot{Q}_{IR} = \dot{q}_{IR} A_1 \varepsilon_{1,top} \sin^2\rho$$
$$\dot{Q}_a = \dot{q}_{solar}\, a(.664 + .521\rho + .203\rho^2) A_1 \alpha_{1,top} \sin^2\rho$$
$$\dot{Q}_{1,SS} = (1-\gamma)\dot{q}_{solar}(A_1 - A_2)\alpha_{1,bottom} \quad [9]$$
$$\dot{Q}_{2,SS} = (1-\gamma)\dot{q}_{solar} A_2 \alpha_{2,bottom}$$
$$\dot{Q}_{1,out} = \sigma(\varepsilon_{1,top} + \varepsilon_{1,bottom})T_1^4$$
$$\dot{Q}_{2,out} = \sigma(\varepsilon_{2,top} + \varepsilon_{2,bottom})T_2^4$$

where $\dot{q}_{IR}$ amd $\dot{q}_{solar}$ are the surface heat flux from the Earth and the heat flux from the Sun at 1 AU respectively, and γ is the fraction of solar heat that is blocked by the sun shade[18]. The surface albedo of the Earth is a and $\sin^2\rho = R_E^2/(R_E + A_{orbit})^2$, where R_E is the radius of Earth and A_{orbit} is the altitude of the orbit. The Stefan-Boltzmann constant is σ and T_1 and T_2 are the temperatures of surfaces 1 and 2 respectively.

Conduction between the surfaces is carried through the 7 verticals of length H and 8 diagonals of length $\sqrt{L^2+H^2}$ in each module. The truss material has a conductivity k and the cross-sectional area of the members A is $\pi/4(d_0^2 - d_i^2)$, where d_i is the inner diameter. Thus the total conduction term is given by:

$$\dot{Q}_{cond,1\to 2} = n_m k A (T_1 - T_2)\left(\frac{7}{H} + \frac{8}{\sqrt{L^2+H^2}}\right) \quad [10]$$

The last term to define is the radiation between the two surfaces. Surface 2 can be treated as three arrays of parallel cylinders separated by $s = \sqrt{3}/2\, L$. The arrays are oriented at 30° angles to each other to comprise the full triangular grid. It is assumed that the surfaces are large enough with respect to the individual cylinders to be treated as infinite. The view factor from an infinite plate to an infinite array of parallel cylinders is shown in Equation [11][19].

$$F_{1\to 2} = 1 - \left[1 - \left(\frac{d_o}{s}\right)^2\right]^{\frac{1}{2}} + \frac{d_o}{s}\tan^{-1}\sqrt{\frac{s^2 - {d_o}^2}{{d_o}^2}} \quad [11]$$

The total projected area of each array is $4 n_m d_0 L$, because each module has four members of length L in each direction. The total radiative heat transfer from surface 1 to the six arrays in surface 2 is then given by:

$$Q_{rad,1\to 2} = \frac{3\sigma(T_1^4 - T_2^4)}{\frac{1-\varepsilon_{1,bottom}}{4 n_m d_0 L \varepsilon_{1,bottom}} + \frac{1}{A_1 F_{1\to 2}} + \frac{1-\varepsilon_{1,bottom}}{A_1 \varepsilon_{1,bottom}}} \quad [12]$$

Substituting Equations [8]-[11] into Equation [7] yields the full energy balance for the system, which can be solved to obtain T_1 and T_2. The temperature difference $T_1 - T_2$ must then be compared to that in Equation [4] to ensure requirements are met.

REFERENCES

[1] "James Webb Space Telescope", NASA, Web: http://www.jwst.nasa.gov/ (21 August 2014).

[2] M. Postman, T. Brown, K. Sembach, M. Giavalisco, W. Traub, K. Stapelfeldt, D. Calzetti, W. Oegerle, R. Michael Rich, H. Phillip Stahl, J. Tumlinson, M. Mountain, R. Soummer, T. Hyde, Advanced Technology Large-Aperture Space Telescope: science drivers and technology developments, OPTICE, 51 (2012) 1-11.

[3] "MOIRE", Ball Aerospace and Technologies Corp., Web: http://www.ballaerospace.com/page.jsp?page=259 (21 August 2014).

[4] "Hobby-Everly Telescope", The University of Texas - Austin, 2014, Web: http://www.as.utexas.edu/mcdonald/het/het.html (21 August, 2014).

[5] "Southern African Large Telescope", Southern African Astronomical Observatory, 2014, Web: http://www.salt.ac.za/ (21 August 2014).

[6] A.B. Meinel, M.P. Meinel, Two-stage optics: high-acuity performance from low-acuity optical systems, OPTICE, 31 (1992) 11.

[7] "Sunjammer", 2014, Web: http://www.sunjammermission.com/home (21 August 2014).

[8] "Articulated Mast Systems", Alliant Techsystems, 2014, Web: http://www.atk.com/products-services/articulated-mast-systems (21 August 2014).
[9] "RoboSimian", Darpa Robotics Challenge, Web: http://www.theroboticschallenge.org/teams/robosimian (21 August 2014).
[10] B. Kennedy, H. Agazarian, Y. Cheng, M. Garrett, G. Hickey, T. Huntsberger, L. Magnone, C. Mahoney, A. Meyer, J. Knight, LEMUR: Legged Excursion Mechanical Utility Rover, Autonomous Robots, 11 (2001) 201-205.
[11] N. Hudson, J. Ma, P. Hebert, A. Jain, M. Bajracharya, T. Allen, R. Sharan, M. Horowitz, C. Kuo, T. Howard, L. Matthies, P. Backes, J. Burdick, Model-based autonomous system for performing dexterous, human-level manipulation tasks, Autonomous Robots, 36 (2014) 31-49.
[12] "Space Launch System", NASA, Web: http://www.nasa.gov/exploration/systems/sls/ (21 August 2014).
[13] N. Lee, S. Pellegrino, Y.-H. Wu, A design algorithm for the placement of identical segments in a large spherical mirror, 2014, (*in preparation)*.
[14] J.M. Hedgepeth, Pactruss support structure for precision segmented reflectors, National Aeronautics and Space Administration, Langley Research Center, Hampton, Va., 1989.
[15] "M55J Data Sheet", Torayca, Web: http://www.toraycfa.com/pdfs/M55JDataSheet.pdf (21 August 2014).
[16] L. Peterson, G. Agnes, How the Mass of Large Gossamer Optical Telescopes Scales with Size and Disturbance Environment, 48th AIAA/ASME/ASCE/AHS/ASC Structures, Structural Dynamics, and Materials Conference, American Institute of Aeronautics and Astronautics, 2007.
[17] W.K. Wilkie, R.B. Williams, G.S. Agnes, B.H. Wilcox, Structural Feasibility Analysis of a Robotically Assembled Very Large Aperture Optical Space Telescope, 48th AIAA/ASME/ASCE/AHS/ASC Structures, Structural Dynamics, and Materials Conference, American Institute of Aeronautics and Astronautics, 2007.
[18] M.D.G. Griffin, J.R. French, Space Vehicle Design, American Institute of Aeronautics & Astronautics, 2004.
[19] Y.A. Çengel, Heat and mass transfer : a practical approach, McGraw-Hill, Boston, 2007.

Journal of
Astronomical Telescopes,
Instruments, and Systems

AstronomicalTelescopes.SPIEDigitalLibrary.org

Design algorithm for the placement of identical segments in a large spherical mirror

Nicolas Lee
Sergio Pellegrino
Yen-Hung Wu

Nicolas Lee, Sergio Pellegrino, and Yen-Hung Wu, "Design algorithm for the placement of identical segments in a large spherical mirror," Journal of Astronomical Telescopes, Instruments, and Systems, Mark Clampin, ed., 1 (2) 024002, (2015).

Journal of Astronomical Telescopes, Instruments, and Systems 1(2), 024002 (Apr–Jun 2015)

Design algorithm for the placement of identical segments in a large spherical mirror

Nicolas Lee,[a,*] Sergio Pellegrino,[a] and Yen-Hung Wu[b]
[a]California Institute of Technology, Graduate Aerospace Laboratories, 1200 East California Boulevard, Pasadena, California 91125, United States
[b]California Institute of Technology, Jet Propulsion Laboratory, 4800 Oak Grove Drive, Pasadena, California 91109, United States

Abstract. We present a design algorithm to compute the positions of identical, hexagonal mirror segments on a spherical surface, which is shown to provide a small variation in gap width. A one-dimensional analog to the segmentation problem is developed in order to motivate the desired configuration of the tiling patterns and to emphasize the desire for minimizing segment gap widths to improve optical performance. Our azimuthal equidistant centroid tiling algorithm is applied to three telescope architectures and produces mirror segment arrangements that compare favorably with existing and alternative designs. [DOI: 10.1117/1.JATIS.1.2.024002]

Keywords: segmentation; space telescope; point spread function; Fourier optics.

Paper 14031 received Nov. 6, 2014; accepted for publication Feb. 3, 2015; published online Mar. 16, 2015.

1 Introduction

Since the invention of the telescope, astronomical observatories have implemented increasingly larger apertures. More recently, designs for both ground- and space-based astronomical telescopes have included optical surfaces that exceed the manufacturing limits for a single monolithic mirror. These designs have necessitated the development of segmented mirrors forming a single large optical surface out of smaller elements. Typically, these segmented mirrors use a hexagonal tiling pattern to achieve a high fill factor. However, the curvature of the optical surface prevents the hexagonal tiling from being perfectly uniform. As a result, telescope designs are forced to use mirror segments that are not identical in planform (the outlined shape of the segment), or to accept nonuniform gaps between segments, which increases the complexity of the mechanical design and degrades signal-to-noise performance through increased diffraction effects.

The first telescopes to use a segmented primary mirror were the Keck telescopes,[1] completed in 1993 and 1996, followed by the Hobby–Eberly Telescope (HET)[2] and South African Large Telescope.[3] The James Webb Space Telescope (JWST) will be a space-based segmented telescope with 18 segments.[4] A concept study for the next-generation space telescope is considering three designs ranging from an 8 m monolithic mirror to a 16.8 m segmented primary with 36 segments.[5] Table 1 summarizes relevant parameters for these and other telescopes with segmented mirrors, including both existing and proposed designs. Most of these telescopes are designed with nonidentical segment geometries. The Thirty Meter Telescope (TMT), for example, uses six each of 82 unique mirror shapes to make up its 492 total segments.[6] In order to accommodate maintenance and occasional resurfacing to restore reflectivity, the telescope will require the fabrication of seven of each segment type such that each shape has one spare.

The aspherical surface figure of the primary mirror in these telescopes requires the segment figures not to be identical. As a result, there is little benefit to requiring identical planforms for the segments. The design choice of using nonidentical segment planforms allows these telescopes to implement a uniform gap width between all segments. This maximizes the capture area of the primary aperture, but becomes impractical for telescope designs with too many segments to individually manufacture and calibrate.

The use of unique segments becomes infeasible as the aperture size continues to increase. For the proposed and eventually canceled Overwhelmingly Large Telescope (OWL), the inclusion of >3000 segments drove the design toward a spherical primary mirror composed of identical segments.[13] The similarly sized In-Space Telescope Assembly Robotics (ISTAR) concept, with >5000 segments, is a design for a robotically assembled and serviceable space telescope.[14] For such a design, segments could be replaced in orbit when damaged, but not resurfaced. Having a large number of uniquely shaped, spare segments in this case would be extremely inefficient. Therefore, these large telescope designs tend to use a spherical primary mirror with mass-produced identical segments in both planform and figure. However, in the future, advances in highly deformable, thin mirrors could enable such identical mirror segments to achieve an adequate optical figure even for an aspherical primary design.[15,16]

This paper specifically addresses the problem of tiling identical hexagonal segments onto a spherical primary mirror. We present a design algorithm to compute the positions of these segments on the spherical surface, which is shown to provide a small variation in gap width. This design algorithm, which we will refer to in this paper as the azimuthal equidistant centroid tiling (AECT) algorithm based on the geometry developed in Sec. 4, is not computationally intensive and can be applied to a range of mirror geometries. We believe that it can be a valuable

*Address all correspondence to: Nicolas Lee, E-mail: nnlee@caltech.edu

2329-4124/2015/$25.00 © 2015 SPIE

Table 1 Hexagonally segmented telescope designs and relevant parameters.

Name	Primary aperture dimension	Number of segments	Date constructed
Ground-based telescopes:			
Keck 1[1]	10 m	36	1985 to 1993
Keck 2[1]	10 m	36	1991 to 1996
Hobby–Eberly Telescope (HET)[2]	11×10 m	91	1994–1997
South African Large Telescope (SALT)[3]	11×10 m	91	2000 to 2005
Large Sky Area Multiobject Fiber Spectroscopic Telescope (LAMOST)[7]	6.67×6.09 m	37	2001 to 2008
Gran Telescopio Canarias (GTC)[8]	10.4 m	36	2002 to 2008
Euro50[9]	50 m	618	Merged with European Extremely Large Telescope (E-ELT)
California Extremely Large Telescope (CELT)[10]	30 m	1080	Merged with Thirty Meter Telescope (TMT)
TMT[6,11]	30 m	492	2014 to 2022 (started)
E-ELT[12]	39.3 m	798	2014 to 2022 (started)
Overwhelmingly Large Telescope (OWL)[13]	100 m	3048	Canceled
Space-based telescopes:			
James Webb Space Telescope (JWST)[4]	6.5 m	18	Expected 2018 launch
Advanced Technology Large-Aperture Space Telescope (ATLAST)[5]	8 to 16.8 m	1 or 36	Preliminary
In-Space Telescope Assembly Robotics (ISTAR)[14]	100 m	>5000	Preliminary

tool for rapid computation of optical configurations for early design studies, without requiring the time or computational power for an optimization-based technique. By focusing specifically on the problem of finding the ideal positions for mirror segments, the AECT algorithm would complement an overall system study that accounts for additional effects, including but not limited to manufacturing and positioning error, secondary optical elements, and active control systems.

In the following section, we provide an overview of the background and prior work on the design and analysis of the three-dimensional geometries of highly segmented telescope mirrors. Section 3 introduces a one-dimensional analog to the tiling problem in order to provide insight into the effect of different tiling options on the optical point spread function (PSF) using Fourier optics. Section 4 presents the details of our new AECT algorithm for tiling segments onto a spherical surface. Section 5 demonstrates that the proposed tiling strategy produces results that are competitive with alternative methods. We show this by applying the AECT algorithm to designs based on the HET, OWL, and ISTAR concepts. Finally, Sec. 6 concludes and summarizes.

2 Background

There has been much prior work on the design and analysis of large segmented telescopes. In this section, we briefly highlight some specific work that is relevant or complementary to the problem of tiling identical segments on a sphere.

2.1 *Telescope Design*

The focus of this paper is on the effect of ideal positioning of segments on a primary mirror. However, the overall performance of a telescope is driven by many other factors. Many prior analyses have considered complete optical systems rather than just the primary mirror. For example, Jolissaint and Lavigne consider a 30 m design with adaptive optics,[17] and Chanan et al. consider active control of the mirror segments[18] in a full telescope system. The aberration introduced by a spherical primary mirror can be corrected through additional optical elements, such as the four-mirror, double Gregorian design used by HET.[19]

Additionally, operational techniques can be developed to mitigate performance limitations. Large ground-based telescopes are typically limited in angular resolution not by diffraction but by atmospheric distortion. This can be compensated by adaptive optics or by postprocessing. Speckle imaging techniques for postprocessing have been used to compensate for this effect and to achieve higher angular resolution. For example, the Keck telescope produced a 0.05 arc sec diffraction-limited near-infrared image.[20]

The design of nominal mirror geometry in telescopes using identical segments is not well documented in the literature.

Published reports provide average segment gap width and ranges of gap width variation for the HET and OWL designs, but no details on the specific design algorithms used.[2,13] The design of the TMT primary mirror segmentation, which uses variable mirror segments, was based on an optimization algorithm that started with a planar hexagonal grid and introduced a design variable that scales the tessellation as a function of distance from the optical axis to account for the mirror curvature.[6] This grid was then cylindrically projected onto the mirror surface to define the individual segment planforms.

2.2 *Optical Analysis*

Techniques for predicting and characterizing the optical performance of a telescope can be partitioned into analytical and numerical methods. Fourier methods are commonly used in optical diffraction theory to compute the PSF of an aperture.[21,22] Yaitskova et al. applied Fourier techniques to the study of large, highly segmented telescope mirrors.[23] The effects of errors from segment position and misfigure are described, while the variation in gap width is reported as having little effect on the PSF.

One approximation for the proportion of energy E_p outside the core PSF is

$$E_\mathrm{p} = \frac{A_\mathrm{F} - A_\mathrm{S}}{A_\mathrm{F}}, \tag{1}$$

where A_F is the surface area of the filled aperture and A_S is the total surface area of the segments not including the gaps.[24] This motivates the desire for a tightly packed arrangement of mirror segments to achieve the best image quality.

Numerical methods include ray-tracing techniques to model the optical behavior of a telescope and can be combined with numerical models of the telescope environment, structure, and other error sources to predict the overall system performance.[25]

3 One-Dimensional Segmentation Analog

As discussed in the previous section, the use of Fourier optics to analytically determine the optical performance of a telescope has been described extensively in the literature.[21–23] It is well known that segmentation of an optical aperture leads to a speckle pattern in the PSF. Variation in the width of gaps between mirror segments introduces intensity variations in the PSF, which increase the background intensity while diminishing the peak intensity of the speckles. This effect does not strongly influence the encircled energy of the PSF but does have a substantial effect on the ratio between the intensities of the central peak of the PSF and the nearest speckle peak. Reducing the average gap width between segments is an effective method for improving the contrast performance of a segmented telescope design by reducing the intensity of speckles near the central peak.

For readers who are less familiar with the conclusions presented in the previous paragraph, we provide, in this section, the following mathematical development demonstrating the effect of mirror segmentation on a PSF. In particular, we wish to characterize the effect of gap width variations between segments on the PSF of the aperture. This provides a direct connection between the geometry of the segments and a measure of the optical performance of the primary mirror. Considering Fraunhofer diffraction, the PSF $h(u, v)$ is computed from the two-dimensional Fourier transform of the aperture function $a(x, y)$ as

$$h(u, v) = |\mathcal{F}[a(x, y)]|^2. \tag{2}$$

In a segmented mirror, the full aperture function $a(x, y)$ can be expressed as the convolution of the segment aperture $s(x, y)$ with a grid factor $g(x, y)$, which is composed of an array of delta functions. The PSF can, therefore, be decomposed as the product of the individual Fourier transforms of the segment aperture and the grid factor:

$$h(u, v) = |\mathcal{F}[s(x, y)]\mathcal{F}[g(x, y)]|^2. \tag{3}$$

However, we find it worthwhile to consider first a simplified one-dimensional analog of the segmentation problem. This analog provides a more intuitive and easily visualized method to highlight the relevant features and constraints inherent in the two-dimensional transforms and three-dimensional geometries associated with real telescope systems. In the following sections, we adapt the two-dimensional notation introduced above for the one-dimensional cases of a fully filled aperture, a uniformly segmented aperture with gaps, and a segmented aperture with nonuniform spacing. For the last case, we quantitatively show that the effect of gap width variation is small relative to the effect of the average gap width.

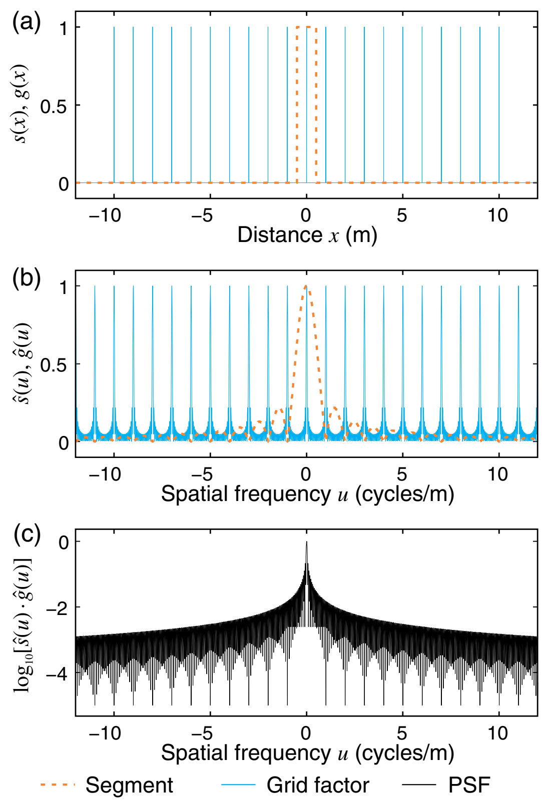

Fig. 1 Point spread function (PSF) of a fully filled linear aperture, composed of 21 segments each 1 m wide at a spacing of exactly 1 m. (a) Segment aperture (in dotted orange) and grid factor (in solid blue), plotted as a function of distance; (b) modulus squared Fourier transforms of the segment aperture and grid factor, plotted as a function of spatial frequency and normalized to a maximum of 1; (c) PSF computed as the squared product of the individual Fourier transforms, plotted logarithmically as a function of spatial frequency and normalized to a maximum of 1.

3.1 *Fully Filled Aperture*

For a one-dimensional, fully filled aperture, a segment of width d can be represented as

$$s(x) = \mathrm{rect}(x/d), \tag{4}$$

and the corresponding grid function for an aperture size of D can be represented as

$$g(x) = \mathrm{rect}(x/D)\mathrm{III}(x/d), \tag{5}$$

where $\mathrm{III}(x)$ is the Dirac comb function. The segment aperture and grid factor are plotted in Fig. 1(a) in orange and blue, respectively, for a numerical example with 21 segments each 1 m wide.

The Fourier transforms of these functions are

$$\hat{s}(u) = \mathcal{F}[s(x)](u) = \mathrm{sinc}(\pi du), \tag{6}$$

$$\hat{g}(u) = \mathcal{F}[g(x)](u) = \mathrm{sinc}(\pi Du)\mathrm{III}(du), \tag{7}$$

with the sharp delta functions in the grid factor transforming into sinc functions because the total aperture does not extend to infinity. This is shown in Fig. 1(b), where the modulus squared of these two functions are plotted as functions of the spatial frequency. Given a defined optical system with focal length f, aperture diameter D, and operating wavelength λ, 1 m^{-1} in the frequency coordinate u is equivalent to λ/D in the angle of observation or $\lambda f/D$ in spatial distance on the image plane.

When the two functions are multiplied together, the peaks of $\hat{g}(u)$ align exactly with the zeros in $\hat{s}(u)$. Accordingly, as shown in Fig. 1(c), the envelope of the PSF has a single peak and smoothly decays with increasing spatial frequency, though lobes in the PSF do occur, corresponding to the $\mathrm{sinc}(\pi Du)$ component of the grid factor, exactly as if the PSF were computed for a single aperture $A(x) = \mathrm{rect}(x/D)$.

3.2 *Uniformly Segmented with Gaps*

When gaps are introduced in the segmentation, the spatial frequency of the grid factor is scaled lower, and the peaks in the Fourier transform appear more closely spaced. Figure 2(a) shows the segment aperture and grid factor for a numerical example with the same 1 m segments as in the previous section, but spaced at a uniform interval of 1.1 m. As seen in Fig. 2(b), the grid factor peaks no longer align with the zeros in the transformed segment function. These result in speckles surrounding the central peak, which can be seen in the PSF in Fig. 2(c).

The effect of gap width on the optical performance of a telescope can be characterized by the encircled energy at a given radius and by the ratio of the central peak to the next largest peak in the PSF. The optical application determines the particular metric that is relevant for characterizing a given system. For example, exoplanet characterization applications using ultrahigh contrast imaging can require detection of light levels on the order of 10^{-6} to 10^{-10} times the central peak, using techniques such as coronagraphy.[26,27] In Fig. 3, the encircled energy is plotted as a function of spatial frequency for a range of gap widths, and the ratio of the two highest peaks is plotted as a function of gap width, using the same one-dimensional example of a 21-segment array with 1 m segments.

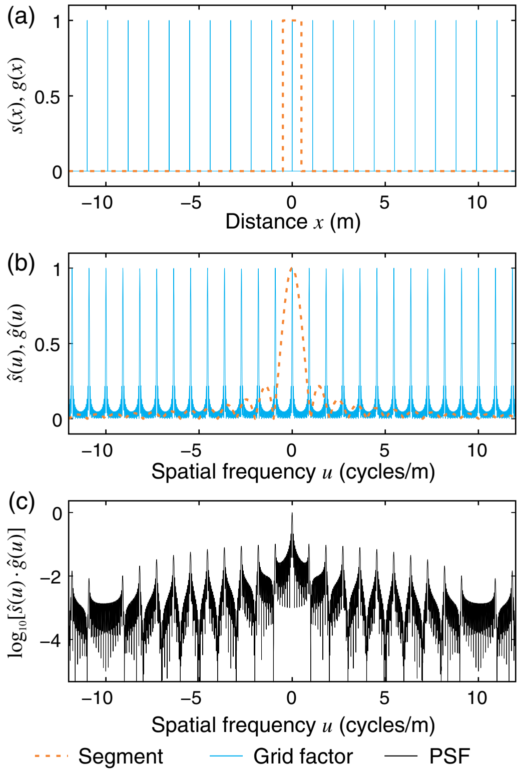

Fig. 2 PSF of a uniformly segmented aperture. The segments are 1 m wide but spaced at intervals of 1.1 m. The individual plots show (a) the segment aperture and grid factor, (b) the modulus squared Fourier transforms of the segment aperture and grid factor, and (c) the PSF computed as the squared product of the individual Fourier transforms. Here, the PSF shows a series of speckles, which are not present in the fully filled case.

For small gaps, the spatial frequency associated with 90% encircled energy is over an order of magnitude smaller than for larger gaps; this effect holds in general for encircled energy percentages of 50 through 99%, but the effect diminishes when considering encircled energies $> \sim 99.5\%$. The trend toward a higher percentage of encircled energy at a smaller spatial frequency implies that the cases with smaller gaps lead to better imaging resolution. The ratio of the peaks also shows a strong dependence on gap width, with the central peak being ~2000 times larger for a gap width of 10 mm, falling to a ratio of ~2.5 with a gap width of 1 m. The ability to distinguish a central spot from its speckle pattern is, therefore, improved at a smaller gap width. Both of these results support the conclusion that minimizing gap width is essential for limiting the effect of diffraction on optical performance.

3.3 *Nonuniform Segmentation*

If the grid factor is not uniformly spaced, the Fourier transform includes a slowly varying envelope attenuating the height of some peaks. This is shown in Fig. 4 for variable segment spacing uniformly sampled from a range of 1.075 to 1.125 m (gap widths of 75 to 125 mm), with the equivalent uniform segmentation shown lightly shaded for comparison.

However, from Parseval's theorem, the energy in the Fourier transform must remain the same as for the uniformly spaced configuration. The additional energy transferred from the

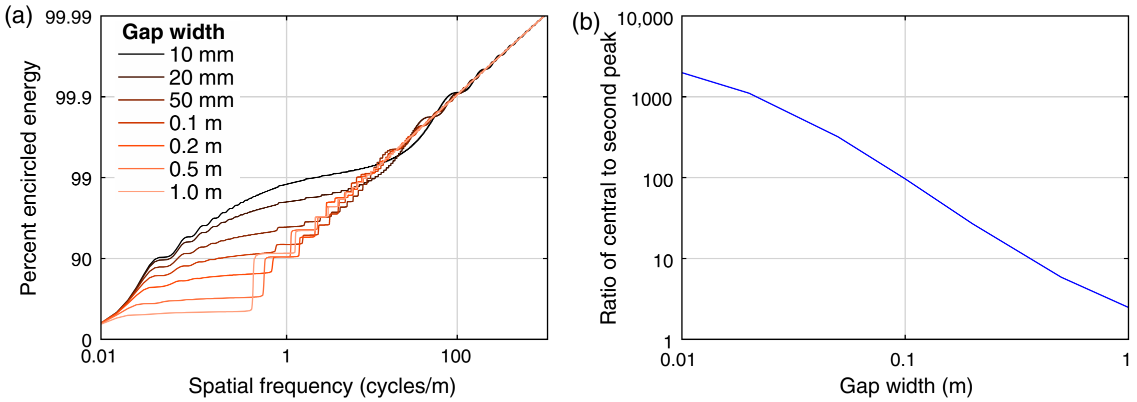

Fig. 3 Dependence of encircled energy and PSF peak ratio on gap width. (a) Percent encircled energy is plotted as a function of spatial frequency for gap widths ranging from 10 mm to 1 m. For a fixed value of encircled energy, smaller gaps tend toward lower spatial frequency, which is indicative of better imaging resolution. (b) The intensity ratio of the central peak to the next highest peak is plotted as a function of gap width, showing that larger gaps are associated with a speckle pattern that is less distinguishable from the central peak.

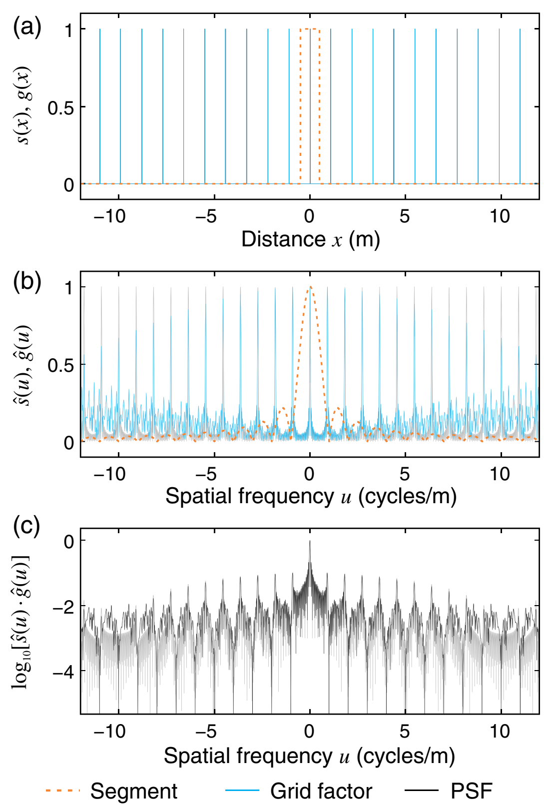

Fig. 4 PSF of an aperture with nonuniform segmentation, with the equivalent uniformly spaced segmentation shown lightly shaded for comparison. The segments are 1 m wide with random spacing sampled from a uniform distribution within a range of 1.075 to 1.125 m. The individual plots show (a) the segment aperture and grid factor, (b) the modulus squared Fourier transforms of the segment aperture and grid factor, and (c) the PSF computed as the squared product of the individual Fourier transforms. The speckles associated with the random segmentation fall off in amplitude with higher spatial frequency, but does not change much at low spatial frequency, while the energy between speckles seems to increase slightly at higher spatial frequency.

attenuated peaks is evident in the growing energy of the intermediate spatial frequencies between peaks.

In order to characterize the effect of random gap variation on the encircled energy and ratio of peak intensities, PSFs were considered using different ranges of gap width variation, from 1 to 100 mm for a mean gap width of 100 mm. For each range value, 200 sampled PSFs were computed. The standard deviation of the percent encircled energy over each population of 100 samples was computed as a function of spatial frequency, and the maximum standard deviation for each range is plotted in Fig. 5(a). The maximum standard deviation increases over the range of gap width variation, but even with the greatest variation considered, the encircled energy profiles do not deviate more than 0.2% from their mean values. The intensity ratio between the first and second peaks was also computed, and the maximum, minimum, and quartile values for each distribution are plotted in Fig. 5(b).

The maximum and minimum ratios remain relatively constant over the range of gap width variation, but the quartiles tend toward lower ratios for low variation, reach a maximum ratio for greater variation, and then decrease again. This is a relatively surprising result and indicates that a moderate level of randomness in the gap width may yield a greater likelihood of providing good contrast between the central and second peaks.

The conclusion that can be drawn from this one-dimensional exercise is that while the encircled energy profile is not influenced strongly by variations in gap width, the contrast performance can actually be enhanced by nonuniform spacing. However, the average gap width is a much stronger driver of both performance characteristics.

4 Segment Tiling Algorithm

The results presented in the previous section using the one-dimensional analog motivate a tiling strategy that minimizes the average gap width when positioning the mirror segments. However, most optical designs must also accommodate practical constraints accounting for factors including fabrication tolerances, mechanical clearances for motion of the segments under active control, or accessibility for construction and servicing. Typically, these impose a hard constraint on minimum gap width, but do not strongly penalize larger gap widths. With

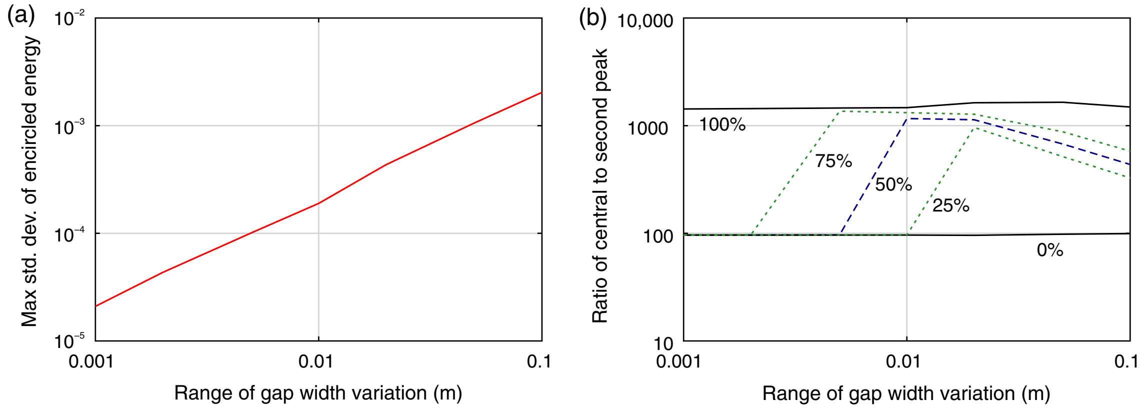

Fig. 5 Variation of encircled energy and peak ratio as functions of the gap width range over 200 sampled configurations. (a) For each value of total range, 200 random aperture functions are generated and the standard deviation of encircled energy, normalized by its mean value, computed as a function of spatial frequency. The maximum standard deviation over spatial frequency is plotted for each value of total range. The low value of maximum standard deviation over the full range of gap width variation shows that the encircled energy profiles do not change much with slightly perturbed segment positions. (b) The ratio of central to second peak amplitude was computed for each PSF, and the maximum, minimum, and quartiles of the distribution are plotted for each value of total range. While the maximum and minimum values do not vary much with gap width variation, the distributions are more heavily weighted toward a low ratio for small variation and tend toward higher ratios for greater variation.

these considerations in mind, we developed a tiling algorithm that demonstrates good performance in minimizing the range of gap width variation, which allows the mean gap width to be as close as possible to the minimum gap constraints. In this section, we start by specifying the geometry used in the tiling algorithm and then discuss the computation of mirror segment positions. Several performance metrics used to evaluate the algorithm are discussed, as well as alternative tiling methods used to determine segment position.

4.1 *Mirror Geometry*

The primary design parameters we used here for a segmented spherical mirror include the radius of curvature R, the side length of a hexagonal segment r, the nominal gap spacing w, and the number of rings of hexagons N around the central segment.

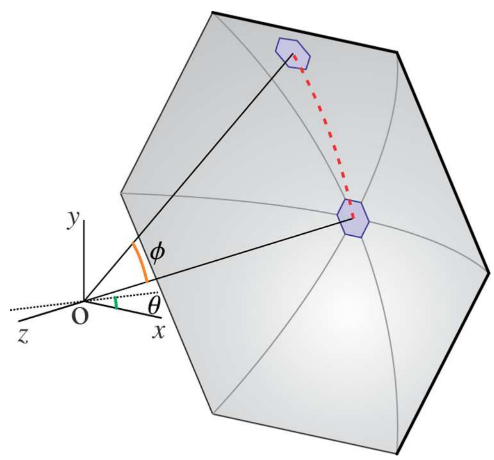

Fig. 6 Geometry used to describe mirror segment locations. A segment initially positioned at the center of the spherical optical surface is rotated about an axis passing through the origin O to reach its final position. The angle of the axis is defined by the spin angle θ and the rotation of the segment is defined by the pitch angle ϕ.

The geometry for describing mirror segment positions is shown in Fig. 6.

First, we define a fixed reference frame with origin O at the center of curvature of the spherical surface. Without loss of generality, we choose the z axis to be pointing away from the mirror surface and the x axis to be aligned with a vertex of the central segment. In this reference frame, the central segment has vertices located at points described in the fixed reference frame by the three-dimensional coordinates:

$$\mathbf{r}_v = \left[r \cos\left(\frac{\pi v}{6}\right) r \sin\left(\frac{\pi v}{6}\right) R \cos\left(\frac{r}{R}\right) \right], \qquad v = 1,2, \dots, 6. \tag{8}$$

All other segments can be fully defined as a sequence of three Euler angle rotations of this central segment about O, ensuring that the vertices remain on the spherical surface. While many rotation sequences are possible, the tiling geometry is most amenable to a 3-1-3 rotation sequence of a reference frame fixed to the segment geometry, which is defined as a spin angle θ about the fixed z axis, a pitch angle ϕ about the intermediate rotated x axis, and a clock angle ψ about the segment-fixed z axis. The rotated segment vertices are then located in the fixed reference frame at

$$\mathbf{r}'_v = \begin{bmatrix} \cos\theta & -\sin\theta & 0 \\ \sin\theta & \cos\theta & 0 \\ 0 & 0 & 1 \end{bmatrix} \begin{bmatrix} 1 & 0 & 0 \\ 0 & \cos\phi & -\sin\phi \\ 0 & \sin\phi & \cos\phi \end{bmatrix} \times \begin{bmatrix} \cos\psi & -\sin\psi & 0 \\ \sin\psi & \cos\psi & 0 \\ 0 & 0 & 1 \end{bmatrix} \mathbf{r}_v, \tag{9}$$

where $\mathbf{r}_v$ as defined above expresses the coordinates of the segment vertices in a reference frame that is rotated with the mirror segment.

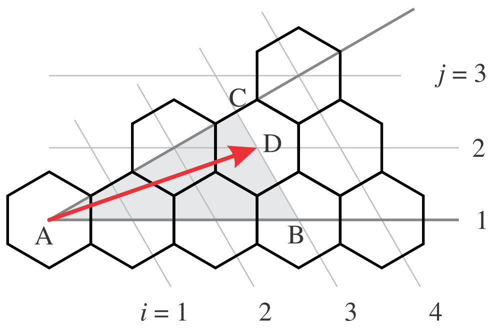

Fig. 7 One sector of the segmented mirror, indexed by ring number and position within each ring. The shaded triangle ABC is used to determine the location of a hexagon's centroid at D.

In order to maintain alignment of each segment with its neighbors, we choose the clock angle to be $\psi = -\theta$ and define each segment with only two angular parameters. This can mathematically be interpreted as a single rigid-body rotation of the pitch angle about the axis defined by the spin angle, as illustrated in Fig. 6.

The hexagonal tiling pattern inherently has 12-fold mirror symmetry. In the following section, we provide a solution for the rotation angles within a 30 deg sector, which can be replicated to fill the entire aperture.

4.2 *Tiling Angles*

We employ an approach to solve for spin and pitch angles based on a planar hexagonal tessellation. The distances between hexagon centroids in the radial direction on the plane are preserved in the azimuthal direction on the sphere, which is why we refer to this technique as the AECT algorithm. In contrast, the TMT algorithm applies a radial scaling to the planar tessellation and then projects cylindrically onto the sphere.[6]

The segments that are located with spin angles ranging from 0 to 30 deg are indexed by their ring number and position within the ring as shown in Fig. 7.

The first hexagon is the central hexagon, with angular coordinates $\theta = 0$ and $\phi = 0$. For each ring i from 1 to n, considering only a 30 deg sector, there are $j_{\max}$ new hexagons to be positioned, where $j_{\max} = \text{floor}(i/2 + 1)$. In order to accommodate the desired gap w, we define a tiling hexagonal side length

$$r_{\text{hex}} = r + \frac{w}{2\cos(\pi/6)}, \tag{10}$$

such that a tightly packed planar tessellation of tiling hexagons will accommodate a gap of w between segment hexagons. We use this planar tessellation to compute the spin angle and the linear distance between the central and rotated segments, and then solve for the pitch rotation that has an arc length equal to this linear distance. For example, the segment labeled D in Fig. 7 has indices $i = 3$, $j = 2$. The angle CAD is computed based on known side lengths AC and CD with $\angle\text{ACD} = 90$ deg, and the spin angle is equivalent to $\angle\text{BAD} = \pi/6 - \angle\text{CAD}$. With this method, the spin angles for each segment as a function of i and j are

$$\theta(i,j) = \frac{\pi}{6} - \tan^{-1}\left(\frac{i - 2j + 2}{i\sqrt{3}}\right), \tag{11}$$

for i from 1 to n and j from 1 to $j_{\max}$. The distance AD can be computed using the law of cosines from triangle ABD, with $\angle\text{ABD} = 60$ deg and known side lengths AB and BD. The corresponding pitch angles are

$$\phi(i,j) = \frac{\sqrt{3}r_{\text{hex}}}{R}\sqrt{i^2 + (j-1)^2 - (j-1)i}. \tag{12}$$

Each hexagon whose spin angle is not 0 or $\pi/6$ is then mirrored across the xz-plane to form a sector that spans 60 deg. Finally, all of the hexagons except the central one are patterned rotationally at intervals of 60 deg to fill the full field.

4.3 *Performance Metrics*

While the optical performance will ultimately depend on the full system configuration, we independently evaluate the performance of the AECT algorithm so that alternative methods can be compared. As with the one-dimensional example in Sec. 3, the PSF for the three-dimensional tiling can be computed. Additionally, a purely geometric evaluation can be made by considering the distribution of gap widths. In the following sections, we discuss the computation of both.

4.3.1 *Gap width distribution*

Mirror segments positioned on the spherical surface will be rotated in three dimensions and two adjacent edges will not necessarily be parallel or even coplanar. To avoid the ambiguity caused by this geometry, we approximate the continuously varying gap width by comparing distances between vertex pairs rather than distances between edges. Because these distances are more closely associated with the mechanical constraints of the telescope rather than the optical performance, we use the three-dimensional distances computed from the segments on the sphere rather than a projection onto a flat plane in front of the aperture.

For a tiling result where the segments are relatively well positioned and with a large enough gap, these vertex-to-vertex distances are adequate for characterizing the distribution of gap widths. However, if segments are positioned more closely, the vertex-to-vertex distances can be skewed and will result in an overestimate of the gap width. Additionally, this method will not discriminate between vertices that are spaced apart appropriately and those that are actually overlapping but spaced apart the same distance in the opposite direction. To address this

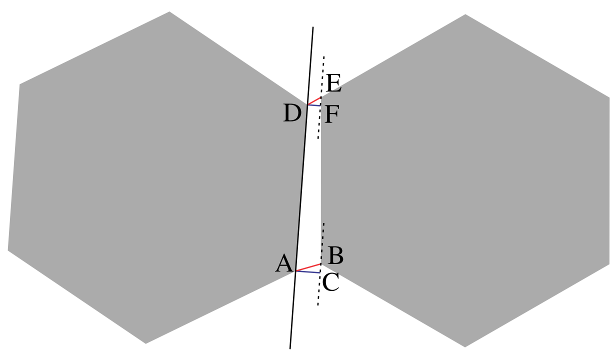

Fig. 8 Gap width represented by vertex-to-vertex distances between two hexagons. The actual vertex-to-vertex distance AB and DE are projected in the direction of the edge normal to obtain projected distances AC and DF.

limitation, each vertex-to-vertex distance can be projected onto a unit vector in the direction of the segment edge normal, within a plane tangent to the spherical surface, as depicted in Fig. 8. This provides a signed distance metric that is a more accurate representation of the gap widths.

In optical designs where the positions of the optical elements are globally fixed, the center of the primary element is often obscured. For such designs, the AECT algorithm can be applied without modification to compute only the positions of the mirror segments that are present. The resulting distribution of gap widths will have the same range but a lower average, since the segments in the central region have gap widths that are close to the maximum value on all sides while the segments near the edge are more closely spaced to adjacent segments in the same ring.

Once the distribution of gap widths is computed, it can be used to modify the parameters of the tiling angles in order to achieve a specific minimum, mean, or other metric. Specifically, the computed value for r_{hex} can be iterated to shift the gap width distribution without distorting the overall pattern.

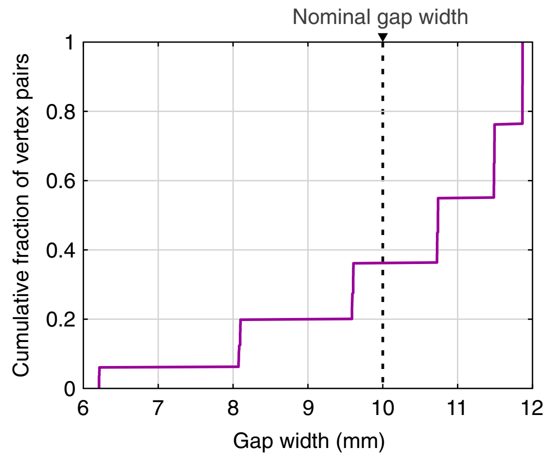

Fig. 10 Cumulative distribution of gap widths for the HET design. The stepped shape of the distribution shows that the gap widths are clustered around six values (the near-vertical segments) between 6.2 and 11.9 mm, with the median (cumulative fraction of 0.5) at 10.7 mm.

4.3.2 *Point spread function*

The distribution of gap widths provides a verification that geometric design constraints are met, but does not directly provide a measure of optical performance. In order to provide a more direct optical measure of performance, the PSF of the aperture function is computed. However, in this paper, we consider only the geometry of the primary mirror, and as a result, there is no well-defined image plane on which to project the aperture function. In order to maintain consistency in comparisons between designs, we evaluate the PSFs based on an aperture function, which is the vertical projection of the mirror segments onto the xy-plane, in front of the primary aperture. In Sec. 5, we present PSFs for several aperture functions, computed using a gray-pixel technique to mitigate the effect of square pixels on the hexagonal structure.

4.4 *Alternative Tiling Methods*

Several alternative tiling methods were considered and are discussed in this section. One intuitive method is to use a 1-2-3 rotation sequence with constant angular increments. This places mirror segments along lines of constant latitude and longitude, but suffers from loss of 12-fold symmetry. With this method, the rows at extreme latitudes are compressed more closely together such that the segments on the equator must be spaced further apart to compensate. While this effect is also present in the AECT method described in Sec. 4.2, it is mitigated by the fact that 12-fold symmetry is enforced, so that this compression occurs more uniformly around the entire edge of the segmented mirror.

With the AECT method above, the triangle ABC in Fig. 7 is well defined on a plane with three known angles and three known side lengths. Another alternative is to work directly with spherical triangles defined on the optical surface. However, the planar relations between the side lengths and angles break down due to the angular defect of the curved surface. By imposing that triangle ABC is a spherical triangle (i.e., composed of great circle arcs), we can choose three known quantities and solve for the remaining three using spherical trigonometry. In order to maintain consistency with the 12-fold symmetry of the full mirror, we require that ∠BAC remains 30 deg. We consider three alternative methods that can be applied, by using prescribed lengths AC and AB, one length AB and angle ∠ABC, or one length AB and angle ∠ACB. The spherical laws of sines and cosines provide the remaining three quantities. The constraint that this geometry imposes on rows of segments to lie on great circle arcs results in a tiling pattern that is less compact

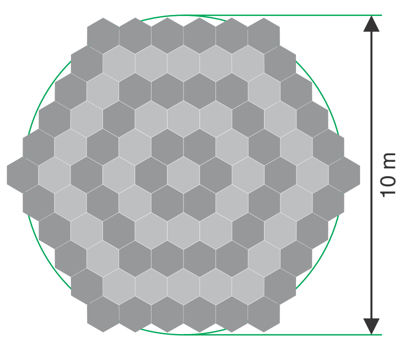

Fig. 9 Segment tiling configuration based on Hobby–Eberly Telescope (HET) parameters. This mirror configuration contains 91 segments, arranged with five rings (shown in alternating shades of gray) around the central segment.

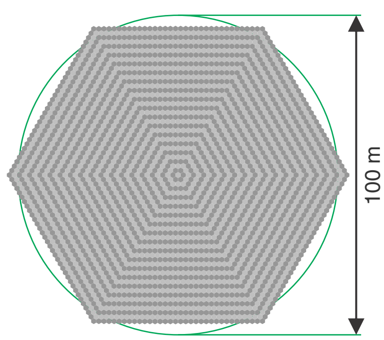

Fig. 11 Segment tiling configuration based on Overwhelmingly Large Telescope (OWL) parameters. This mirror configuration contains 3367 segments, arranged with 33 rings (shown in alternating shades of gray) around the central segment.

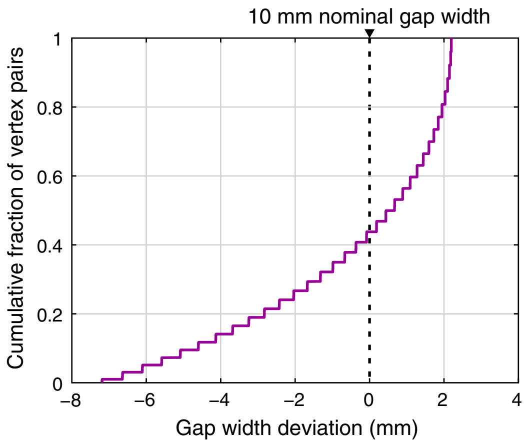

Fig. 12 Cumulative distribution of gap widths for the OWL design. Compared to the HET distribution in Fig. 10, the greater number of rings in the OWL design results in a more continuous distribution of gap widths. However, these widths are still clustered around specific values, as shown by the stepped shape of the plot.

than with the method above, resulting in a larger range of gap width variation. This is shown for a particular example in Sec. 5.2.

5 Application to Telescope Architectures

Using the AECT algorithm presented in Sec. 4, we generated possible mirror segmentation geometries for three telescope architectures. The first architecture is based on the optical parameters of the HET design in order to evaluate the tiling performance against an existing telescope. The second compares the tiling algorithm to the segmentation presented for the OWL phase A design, to exercise its performance with one of the largest proposed telescope primary mirrors. We use this design study to provide comparisons between our AECT algorithm and some of the alternatives discussed in Sec. 4.4. Finally, we apply the algorithm to the ISTAR architecture, which is a less mature design. Because the optical design for ISTAR has not yet been frozen, parametric studies can be used to explore a range of geometries. With the ISTAR architecture, we present an extension to the AECT algorithm by leveraging the hierarchical structure described below.

For each of these architectures, mirror segment positions are computed based on the AECT algorithm, and the gap widths between segments are computed to evaluate the algorithm's performance. Using a MATLAB® script on a modern laptop computer, the mirror segment positions were computed in 0.6 to 3.9 ms depending on the number of segments, and the gap width distributions were computed in 3.9 to 130 ms. The principal computational benefit of this algorithm is that it produces satisfactory results through a single iteration or through optimization of a single parameter r_{hex}. In contrast, a general optimization of the segment positions would require potentially thousands or millions of evaluations of the gap width distribution.

5.1 Comparison with Hobby–Eberly Telescope Design

The HET is composed of 91 identical mirror segments, where each segment is 1 m flat-to-flat.[2] The spherical primary has a radius of curvature of 26.165 m, and the gaps between segments vary from 6.2 to 15.8 mm. By applying the AECT algorithm and targeting the same minimum gap width, we achieved a design, shown in Fig. 9, with gaps that ranged in width from 6.2 to 11.9 mm and a mean gap width of 10.3 mm. The distribution of gap widths is shown in Fig. 10.

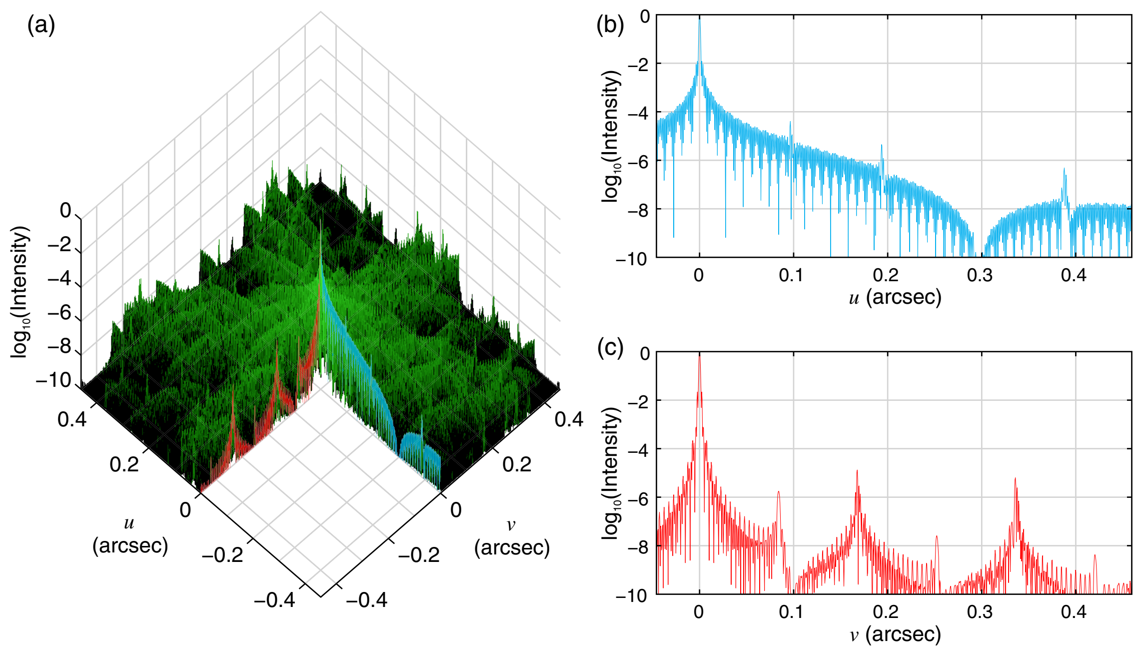

Fig. 13 PSF of a 100 m aperture based on the proposed OWL geometry. (a) Isometric view of the central portion of the PSF spanning a box size of 0.9 arc sec for $\lambda = 0.65$ μm. The color and height scale logarithmically with intensity. (b) and (c) Orthogonal cross-section profiles of the PSF, with directions selected to capture the neighboring peaks from the speckle pattern. The directions are indicated by the cutaway on the isometric plot.

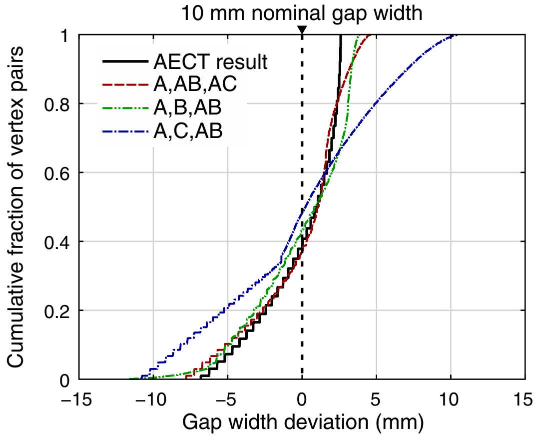

Fig. 14 Cumulative gap width distributions based on the baseline azimuthal equidistant centroid tiling (AECT) algorithm and the three alternative tiling methods using spherical trigonometry. The legend indicates the angles and side lengths that are prescribed, based on the notation in Fig. 7 and the spherical triangular tiling methods described in Sec. 4.4.

In this analysis and for the designs presented below, cumulative distributions of the gap widths are used rather than histograms in order to avoid sensitivity to binning. In each case, perpendicular projected distances between vertex pairs are computed as described in Sec. 4.3.1 and plotted in order of magnitude to obtain the cumulative distribution. The resulting gap width distribution using the AECT algorithm has a 40% reduction in the total range compared to the original HET design. Assuming a similar distribution of gap widths, the mean gap width can be reduced by ~20%, leading to a reduction in diffraction effects as discussed earlier.

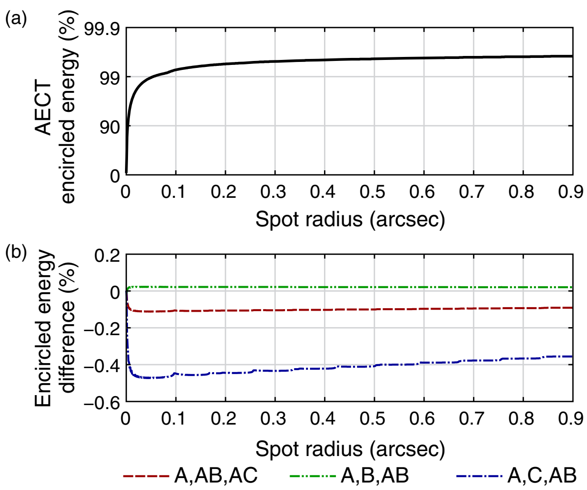

Fig. 15 Encircled energy profiles computed from the OWL PSFs. (a) Percent encircled energy of the baseline AECT design for the OWL configuration, plotted on a logarithmic vertical scale as a function of spot radius in arc seconds for $\lambda = 0.65$ μm. (b) Difference in encircled energy between the three spherical triangular tiling designs and the baseline AECT design, in percentage points. The legend indicates the angles and side lengths that are prescribed, based on the notation in Fig. 7. One alternative design shows slightly greater encircled energy than the AECT design, and the other two show much lower encircled energy in comparison.

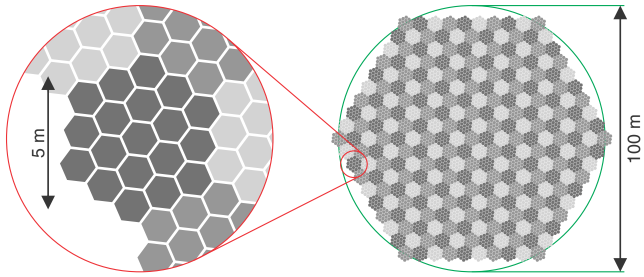

Fig. 16 Hierarchical segment tiling configuration for the In-Space Telescope Assembly Robotics (ISTAR) design, with 19 segments in a module (left) and 271 modules in the full primary (right). Individual modules are shaded in alternating shades of gray for clarity. All segments are identical to each other, and all modules are also identical to each other, which decreases the complexity of manufacturing and assembly.

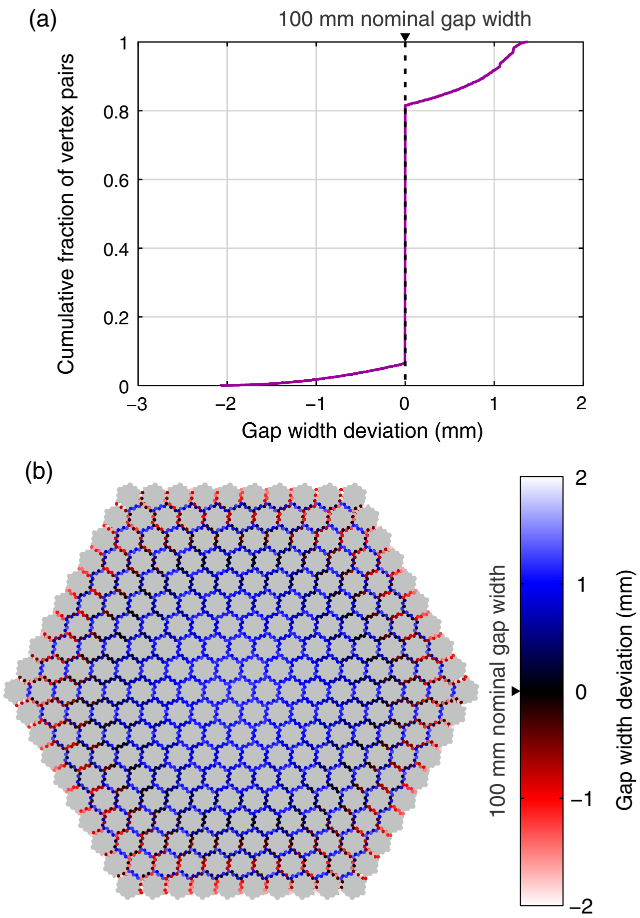

Fig. 17 Cumulative distribution of gap widths for the ISTAR design. (a) The total distribution of gap widths considering all adjacent segments regardless of their module. Here the intramodule gaps are seen as the large near-vertical segment that appears at zero deviation from the nominal width. The intermodule gaps, considering adjacent segments in different modules, comprise the remainder of the distribution and follows a trend similar to the OWL distribution. (b) The spatial configuration of intermodule gaps are plotted and color-coded based on deviation from the nominal 100 mm gap width. Smaller gaps are plotted in red and larger gaps in blue. Note that gaps between adjacent rings remain large from the center to the edge, while the gaps between modules in the same ring decrease in width from the center to the edge. Intramodule gaps are not plotted because of their small variation relative to intermodule gaps.

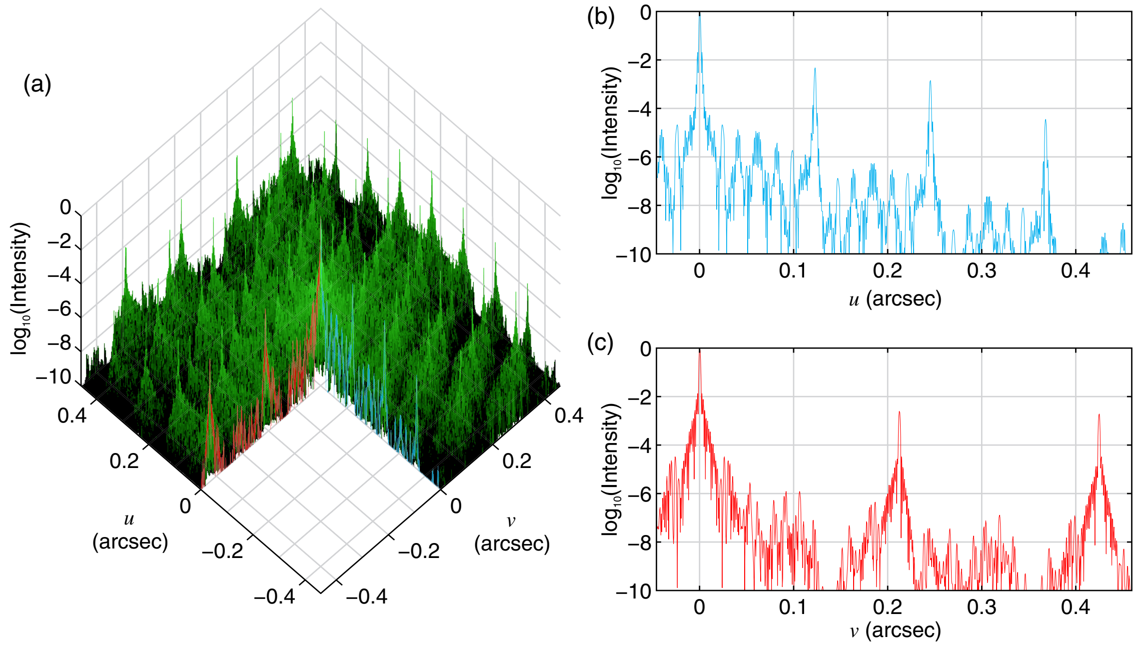

Fig. 18 PSF of a 100 m aperture based on the proposed ISTAR geometry. (a) Isometric view of the central portion of the PSF spanning a box size of 0.9 arc sec for $\lambda = 0.65$ μm. The color and height scale logarithmically with intensity. (b) and (c) Orthogonal cross-section profiles of the PSF, with directions selected to capture the neighboring peaks from the speckle pattern. The directions are indicated by the cutaway on the isometric plot.

5.2 *Comparison with OWL Phase A Design*

In the OWL phase A study, an optical configuration was presented for a 100 m spherical primary mirror with a 250 m radius of curvature, composed of 3048 mirror segments with a flat-to-flat dimension of 1.6 m (hexagonal side length of 0.92 m).[13] The design of this primary mirror included variable gap widths ranging from 4 to 14 mm.

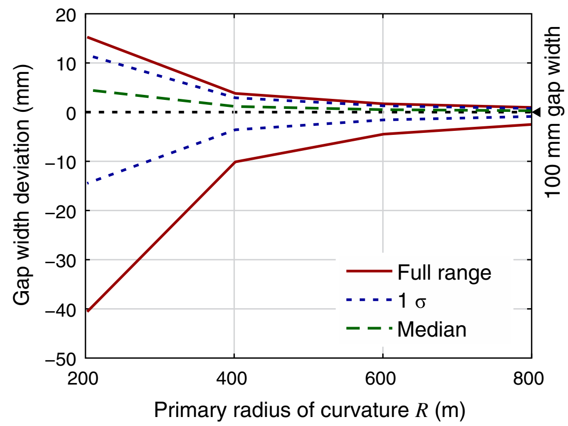

Fig. 19 Distribution of intermodule gap widths for ISTAR design as a function of primary mirror radius of curvature. Because of the large fraction of intramodule gaps and their small variation relative to the intermodule gaps, we show only the intermodule gaps here. As was evident in the upward curvature of the point design cumulative distributions above, the median and quartile values are biased toward the upper end of the distribution. The total range satisfies the project-imposed constraint of 10% maximum deviation from the nominal 100 mm gap only for mirror radius of curvature >400 m.

Using the proposed design algorithm with the OWL geometry, a fully filled configuration including 33 rings was generated, as shown in Fig. 11.

This design includes 3367 segments filling the entire hexagon, whereas the phase A design eliminated segments lying outside the circular aperture or behind an obscuration, leaving a total of 3048 segments. As a result, the distribution of gap widths presented here is conservative relative to a more complete design that accounts for removed segments. As discussed in Sec. 4.3.1, the elimination of the central segments behind the obscuration will result in a further reduction of the average gap width. The cumulative distribution of gap widths, computed as

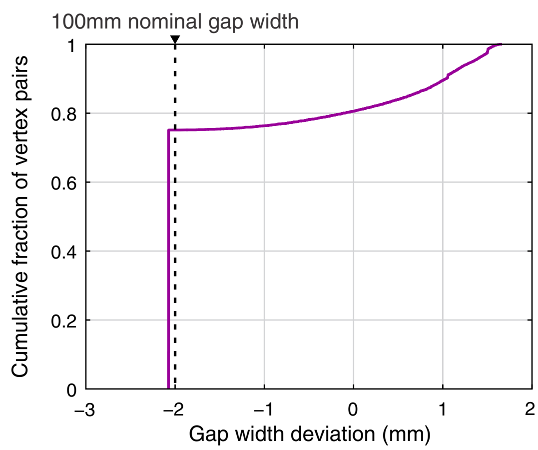

Fig. 20 Cumulative distribution of gap widths for alternative ISTAR design, minimizing the average gap width while keeping all gaps larger than the smallest in the original configuration. Here, the intramodule gaps appear at the bottom of the distribution, and the intermodule gaps comprise the upper curved portion of the distribution.

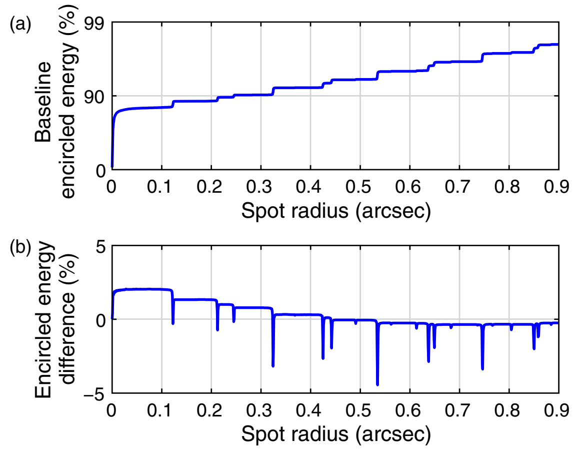

Fig. 21 Encircled energy profiles computed from the ISTAR PSFs. (a) Percent encircled energy of the baseline AECT design for the ISTAR configuration, plotted on a logarithmic vertical scale as a function of spot radius in arc seconds for $\lambda = 0.65\ \mu$m. (b) Difference in encircled energy between the modified AECT design and the baseline design, in percentage points. The positive values at smaller spot radius indicate a higher percentage of encircled energy in the modified design.

the vertex-to-vertex distance projected onto the normal direction, is shown in Fig. 12.

An average gap width of 10 mm was targeted by iteratively modifying r_{hex}, and a total range of 9 mm in gap width variation was achieved, which is 10% better than the 10 mm range reported in the OWL phase A study.

The PSF for this aperture was computed using a gray-pixel bitmap image with 7.33 mm spatial resolution and 16-bit intensity resolution. This image was padded to a total of 40,000 pixels spanning a spatial dimension of 293 m. The central portion of the computed PSF is shown in Fig. 13 as an isometric view with two orthogonal cross-section profiles.

In order to compare the AECT design algorithm with alternatives using spherical trigonometry as described in Sec. 4.4, each of the three competing spherical triangular methods was used to compute a gap width distribution as well as PSFs. Figure 14 shows a comparison of the gap width distributions, with all three alternatives resulting in a wider range of gap widths than the baseline AECT design.

Figure 15 compares the difference between the encircled energy profiles of the baseline AECT design and the alternative spherical triangular designs.

The second alternative method shows a slightly greater encircled energy than the baseline design, despite the greater range in gap widths. However, the other two alternatives show much a lower encircled energy in comparison. Overall, the total percentage point difference in encircled energy is less than half a percentage point, which indicates a small effect on optical performance. The total range of gap widths is likely a more significant design driver, because the small range of the AECT design allows for a more aggressive reduction of the mean gap width.

5.3 *Proposed Hierarchical Design for ISTAR*

The robotically assembled concept proposed for the ISTAR project includes a 100 m spherical primary mirror assembled from modules of mirror segments.[14] An objective of the design is to produce a mirror segment configuration that achieves an average gap width of 100 mm with no greater than 10% variation and to simplify the manufacturing and assembly process by leveraging symmetry and modularity.

To achieve these goals, we developed a hierarchical extension to the AECT algorithm, where the positions of 19 segments were first computed to form a module with $n = 2$ rings, and then the module itself was treated as a larger hexagon and tiled to form the primary with $N = 9$ rings, totaling 5149 mirror segments. These are shown in Fig. 16. In order for the modules to tile such that the individual segments align properly, the module is rotated about its z axis by

$$\psi_{\text{mod}} = \tan^{-1}\left[\frac{1}{\sqrt{3}(2n+1)}\right] + \frac{\pi}{2}. \tag{13}$$

The effective size of the module tiling hexagon is defined by

$$r_{\text{mod}} = r_{\text{hex}}\sqrt{3n^2 + 3n + 1}, \tag{14}$$

and the spin and pitch angles are computed as described in Sec. 4.2.

Because the modules span a relatively small solid angle within the primary, there is very little variation in the intramodule gaps, spanning a range of <2.5 μm. This results in a total distribution, including both intermodule and intramodule gaps, where a large fraction of the gaps is very close to the desired gap width. In the ISTAR configuration, ∼75% of all gaps are intramodule gaps, as can be seen in the distribution in Fig. 17(a). The total range of gap width variation, however, suffers slightly as a consequence, compared to a configuration where all mirror segments are tiled in a single large array as in the OWL design described in Sec. 5.2. Figure 17(b) shows how the gap widths are spatially distributed over the surface of the full primary. Because of the low variation of intramodule gaps, only the intermodule gaps are plotted, showing the larger gap widths near the center of the primary and the smaller gap widths near the rim.

The PSF for this aperture was computed using the same technique described above for the OWL PSF. The central portion of the computed ISTAR PSF is shown in Fig. 18 as an isometric view with two orthogonal cross-section profiles. Because of the imposed larger minimum gap width for robotic servicing, diffraction effects are much greater than in the OWL design, with speckle peaks approximately two orders of magnitude less intense than the central peak, compared to almost five orders of magnitude for OWL.

The design process was repeated for several values of the primary radius of curvature R, ranging from 200 m up to the baseline 800 m for the design described above. The range of intermodule gaps, plotted in Fig. 19, shows that the gap variations increase slowly as R decreases from 800 down to 400 m, but then grows more rapidly for smaller values of R. This parametric study demonstrated the value of using the AECT algorithm to quickly produce viable mirror geometries, without the need for intensive computation or optimization routines.

A feature of the hierarchical segmentation method is that an extra degree of freedom is introduced by separately tiling first a module and then the full mirror. This allows the gap width distribution to be manipulated. As discussed in Sec. 3.3, we would ideally like to produce a tiling geometry that has minimum average gap width subject to constraints. In the hierarchical method, we are able to more aggressively tile the segments within each module and achieve a distribution very close to the minimum width constraint. The intermodule gap distribution would then target a larger gap width in order to avoid violating this constraint. An example of a possible gap width distribution is shown in Fig. 20. Here, the total range of gap widths has increased by 8.3% from 3.45 to 3.74 mm, but the average gap width has been reduced from the original configuration by 1.4 mm. While the original AECT scheme had an average gap width that was 2.07 mm (60% of the full range) above the minimum, this modification achieves an average gap width that is only 0.67 mm (18% of the full range) above the same minimum.

Figure 21 shows the encircled energy of the original design and the difference with the modified design. From this result, it appears that the modified design has up to two percentage points greater encircled energy at small radii, but that this effect does not persist beyond a radius of ~0.4 arc sec. Depending on the imaging application, one design may be preferable over the other, or a further parametric study using the AECT algorithm can be applied to characterize the range of possible designs.

6 Conclusions

In this paper, we presented the AECT algorithm to determine the positions of identical hexagonal mirror segments on a spherical surface. We used a one-dimensional analog to motivate the desire for a small range in gap widths and to bias the mean toward the low end of that range. We showed through comparison with HET and OWL designs that the algorithm compares favorably to prior techniques in terms of the total range of gap widths and presented a hierarchical concept based on the ISTAR geometry that is effective for biasing the gap width distribution and could potentially lead to improved designs for other large telescopes. The utility of the algorithm for use in a parametric design study was also demonstrated using the ISTAR concept.

From the one-dimensional analog, we verified that the PSF is not strongly influenced by variation in gap width and also found that the contrast performance could be enhanced by nonuniform spacing. Through the design studies with three telescope configurations, we showed that the AECT algorithm is capable of satisfying mirror segment placement constraints over a wide range of geometries and is well suited for use in early design studies. The HET study demonstrated that the AECT design could reduce the mean gap width by ~20% compared to the actual design. The OWL study demonstrated that the AECT algorithm can handle several thousand individual segments and showed a 10% reduction in total gap width range from the previously reported design. The ISTAR study demonstrated several approaches for using the AECT algorithm for preliminary design.

In future work, the AECT algorithm would also be a viable candidate to provide starting points for optimization of a final design. As future ground- and space-based telescopes target increasingly large apertures, the need for computationally efficient design algorithms will become more essential in order to manage the large number of mirror segments required.

Acknowledgments

We thank Marie Laslandes for helpful discussions and James Breckinridge for valuable and detailed feedback about the manuscript. N. Lee was supported through this work by a postdoctoral fellowship from the W. M. Keck Institute for Space Studies. The research was carried out in part at the Jet Propulsion Laboratory, California Institute of Technology, under a contract with the National Aeronautics and Space Administration.

References

1. J. E. Nelson, T. S. Mast, and S. M. Faber, "The design of the Keck Observatory and Telescope," Technical Report Keck Observatory Report No. 90, Caltech (1985).
2. V. L. Krabbendam et al., "Development and performance of Hobby–Eberly Telescope 11-m segmented mirror," *Proc. SPIE* **3352**, 436–445 (1998).
3. R. Stobie, J. G. Meiring, and D. A. H. Buckley, "Design of the Southern African Large Telescope (SALT)," *Proc. SPIE* **4003**, 355–362 (2000).
4. P. A. Sabelhaus and J. E. Decker, "An overview of the James Webb Space Telescope (JWST) project," *Proc. SPIE* **5487**, 550–563 (2004).
5. M. Postman et al., "Advanced Technology Large-Aperture Space Telescope: science drivers and technology developments," *Opt. Eng.* **51**(1), 011007 (2012).
6. C. Baffes et al., "Primary mirror segmentation studies for the Thirty Meter Telescope," *Proc. SPIE* **7018**, 70180S (2008).
7. Y. Chu, "The large sky area multi-object fibre spectroscopy telescope (LAMOST) project," in *Wide-Field Spectroscopy*, E. Kontizas et al., Eds., Vol. 212, pp. 67–72, Springer, Netherlands (1997).
8. L. Jochum, J. Castro, and N. Devaney, "Gran Telescopio Canarias: current status of its optical design and optomechanical support system," *Proc. SPIE* **3352**, 621–631 (1998).
9. T. Andersen et al., "The Euro50 extremely large telescope," *Proc. SPIE* **4840**, 214–225 (2003).
10. T. S. Mast and J. E. Nelson, "Segmented mirror control system hardware for CELT," *Proc. SPIE* **4003**, 226–240 (2000).
11. J. Nelson and G. H. Sanders, "TMT status report," *Proc. SPIE* **6267**, 626728 (2006).
12. European Southern Observatory, "The E-ELT construction proposal," Technical Report, ESO (2011).
13. European Southern Observatory, "OWL concept design report: phase A design review," Technical Report OWL-TRE-ESO-0000-0001, ESO (2005).
14. K. Hogstrom et al., "A robotically-assembled 100-meter space telescope," presented at *International Astronautical Congress*, IAC-14-C2.2.6, International Astronautical Foundation, Toronto, Canada (2014)
15. M. Laslandes et al., "Optimization of electrode configuration in surface-parallel actuated deformable mirrors," *Proc. SPIE* **9148**, 914843 (2014).
16. J. Steeves et al., "Design, fabrication and testing of active carbon shell mirrors for space telescope applications," *Proc. SPIE* **9151**, 915105 (2014).
17. L. Jolissaint and J.-F. Lavigne, "An analytic model for the study of the impact of mirror segmentation on AO performance and application to a 30-m segmented telescope," *Proc. SPIE* **5497**, 349–360 (2004).
18. G. Chanan et al., "Control and alignment of segmented-mirror telescopes: matrices, modes, and error propagation," *Appl. Opt.* **43**(6), 1223–1232 (2004).
19. D. O'Donoghue, "Correction of spherical aberration in the Southern African Large Telescope (SALT)," *Proc. SPIE* **4003**, 363–372 (2000).
20. K. Matthews et al., "The first diffraction-limited images from the W. M. Keck Telescope," *Publ. Astron. Soc. Pac.* **108**(725), 615–619 (1996).
21. J. W. Goodman, *Introduction to Fourier Optics*, McGraw-Hill Series in Electrical and Computer Engineering, 2nd ed., McGraw-Hill, New York (1996).
22. E. Hecht, *Optics*, 4th ed., Addison-Wesley Publishing Company, San Francisco, California (2001).
23. N. Yaitskova, K. Dohlen, and P. Dierickx, "Analytical study of diffraction effects in extremely large segmented telescopes," *JOSA A* **20**(8), 1563–1575 (2003).
24. J. B. Breckinridge, *Basic Optics for the Astronomical Sciences*, SPIE Press, Bellingham, Washington (2012).
25. C. Nissly et al., "High-resolution optical modeling of the Thirty Meter Telescope for systematic performance trades," *Proc. SPIE* **7017**, 70170U (2008).
26. M. Troy and G. Chanan, "Diffraction effects from giant segmented-mirror telescopes," *Appl. Opt.* **42**(19), 3745–3753 (2003).
27. D. Spergel et al., "Wide-field infrared survey telescope-astrophysics focused telescope assets WFIRST-AFTA final report," Technical Report, WFIRST Project (2013).

Nicolas Lee is a W. M. Keck Institute for Space Studies postdoctoral scholar in aerospace at Caltech and received his PhD in aeronautics and astronautics from Stanford University in 2013. Current research

interests include deployable space structures, small spacecraft systems, and space environmental monitoring.

Sergio Pellegrino is the Joyce and Kent Kresa professor of aeronautics and professor of civil engineering at Caltech and a Jet Propulsion Laboratory senior research scientist. He received his laurea in civil engineering from the University of Naples in 1982 and his PhD in structural mechanics from the University of Cambridge in 1986. His general area of research is the mechanics of lightweight structures, with a focus on packaging, deployment, shape control, and stability.

Yen-Hung Wu received his MS in optical engineering in 2007 from the University of Arizona. Since 2007, he has been a staff engineer at the Jet Propulsion Laboratory, California Institute of Technology. He is a member of the Optical Design & Engineering group and was the optical and opto-mechanical engineer for the NuSTAR metrology laser.

Multi-Layered Membrane Structures with Curved Creases for Smooth Packaging and Deployment

Nicolas Lee* and Sergio Pellegrino†

California Institute of Technology, Pasadena, CA 91125

We present a design for a deployable multi-layered membrane structure that uses a curved crease pattern to enable smooth wrapping around a spool. The crease pattern is parameterized to enable a variety of designs, and a specific implementation was selected based on an existing patch antenna array design. We constructed a prototype structure based on this geometry, and conducted deployment tests to measure the deployment force profile required to unfold the structure and to unwrap it from a spool. We find that the deployment force for unwrapping is significantly higher than for unfolding. These force profiles are repeatable over multiple deployments and the global trends do not depend on deployment rates over the range tested, between 1 and 8 mm/s. However, the local dynamic behavior can depend on deployment rate.

I. Introduction

In this paper, we present a design for a multi-layered membrane structure that can be deployed from a cylindrical spool. This type of deployable membrane structure has potential applications in spacecraft systems. Deployable systems in general are a crucial aspect of spacecraft design because of their ability to address and satisfy constraints imposed during different mission phases. During launch, the rocket fairing and the acoustic environment impose geometric and stiffness constraints that are often incompatible with the performance requirements for large area systems during the operational phase. Maximizing the area of a spacecraft component is essential for many systems where performance is directly related to a captured flux quantity. Obvious examples include solar arrays and communications antennas, but deployed area is also a factor for systems including but not limited to telescopes, radar, and in situ dust detectors and collectors. While many spacecraft use deployable technology, it remains a significant risk with a history of many failures and anomalies. These include jammed solar panel hinges (e.g. Intelsat 19[1]) and dish antennas (e.g. Galileo's high gain antenna[2] and SkyTerra 1's 22-meter L-band antenna[3]), incomplete tether deployments (e.g. MAST[4]), and broken tethers and booms (e.g. ARTEMIS, TSS-1R[5]). Membrane systems in particular are prone to unexpected behavior during deployment, including for example the tearing of the Znamya 2.5 solar reflector,[6] and premature expansion of components of the Inflatable Antenna Experiment.[7] The dependence of future spacecraft on deployable systems necessitates a better understanding of their behavior through all mission phases in order to characterize and reduce overall mission risk.

Deployable spacecraft systems can range from extremely lightweight, such as solar sails that use membranes only several microns thick, to relatively thick rigid panels such as the solar arrays deployed on communications satellites. For some applications, the rigidity of a panel is not required and the complexity of hinges undesirable. In some cases, like proposed large radar arrays for Earth observation, discrete panels are too heavy to be feasible but the thin membranes used in solar sails are too thin to support the electronic components associated with each antenna.

In this paper, we present a design for a deployable thick-membrane structure for applications that require an intermediate solution between thin membranes and rigid panels, using a membrane that is thick enough to support electronics but is thin enough to be flexible. In particular, we focus on the implementation of a planar structure that is compatible with an existing design for a membrane patch antenna array for synthetic aperture radar (SAR), as illustrated in Figure 1. This structure is composed of two parallel membrane surfaces joined to each other by a set of ribs that determine the thickness of the structure. The membranes are creased using a curved design to enable tight packaging around a hub such that the structure can be packaged for launch into a volume with dimensions smaller

*W. M. Keck Institute for Space Studies Postdoctoral Scholar, Graduate Aerospace Laboratories, 1200 E. California Blvd. MC 301-46. nnlee@caltech.edu

†Joyce and Kent Kresa Professor of Aeronautics and Professor of Civil Engineering, Graduate Aerospace Laboratories, 1200 E. California Blvd. MC 301-46. AIAA Fellow. sergiop@caltech.edu

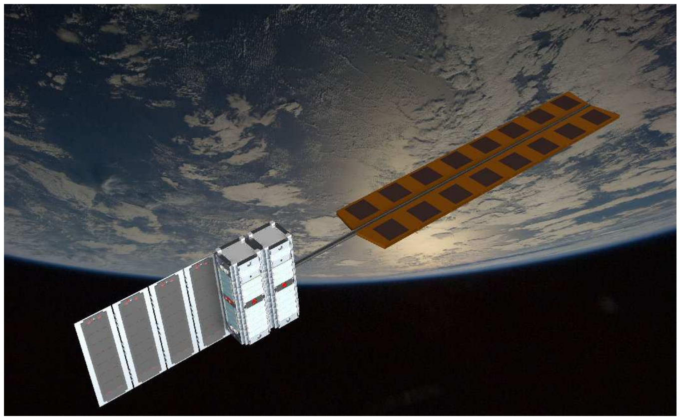

Figure 1. Rendering of a 6U CubeSat concept with membrane antenna array. In this image, the membrane antenna is shown with 16 patch antenna elements and is supported by a longitudinal boom. The membrane would theoretically deploy out of a 3U volume, with the spacecraft bus occupying the other 3U. Background image courtesy NASA.

than the length of an uncreased panel. The full structure is 29.2 cm in width and 124.8 cm in length, with a 1.27 cm separation between the two layers. A full-size prototype structure was constructed (Figure 2) and used to conduct deployment experiments.

Through these experiments, we found that the dominant force resisting deployment as the structure is unfolding results primarily from the unwrapping of the membrane from a hub, but that this deployment force can be exceeded by the tension required at the end of deployment to ensure that the structure is adequately flat. The measured force profiles were repeatable over multiple deployments and the global trends did not appear to depend on deployment rates over the range tested, between 1 and 8 mm/s. We also found that the deployment rate can affect the dynamic behavior of the membrane, even at relatively low rates.

Section II provides an overview of relevant background to the work described in this paper. Section III describes mathematically the crease pattern used to enable smooth wrapping of the folded structure on a cylindrical hub, including a general derivation for a parameterized structure with arbitrary dimensions and a specific design for the antenna array configuration. Section IV presents the techniques used to assemble a prototype membrane structure consistent with the geometry of the design from Section III. Deployment experiments that characterize the force profile using the prototype in a materials testing machine are described in Section V, with results presented and discussed in Section VI. Finally, Section VII provides a summary of the key findings and directions for further work in this area.

II. Background

This section highlights previous work on membrane packaging and deployment, as well as on the existing membrane antenna array configuration that our membrane structure is designed to support.

A. Membrane Packaging and Deployment

Previous work on membrane packaging and deployment spans the range between theoretical models and empirical observations. In particular, much work has been done on the problem of wrapping a membrane around a hub. Guest and Pellegrino[8] provided an algorithm for a crease pattern to wrap a membrane around a polygonal hub by determining the 3D geometry of the crease vertices. Furuya et al.[9] described experiments in centrifugal deployment of a wrapped membrane from a spinning hub. Recently, Zirbel et al.[10] performed experiments demonstrating the deployment of a membrane with embedded rigid panels from a polygonal hub.

In order to enable wrapping around a round hub, Lee and Close[11] presented an algorithm to compute a crease pattern composed of equally spaced curved creases. In that work, creases are restricted to lie on a horizontal plane as they are wrapped around the hub. This paper extends the technique to account for the more general case where creases may not lie only on a horizontal plane. The crease pattern is applied to a membrane geometry such that multiple membrane layers can be attached to each other at a specified distance to form a thicker global structure once deployed. This membrane structure design is targeted to support a planar patch antenna array described in the following section.

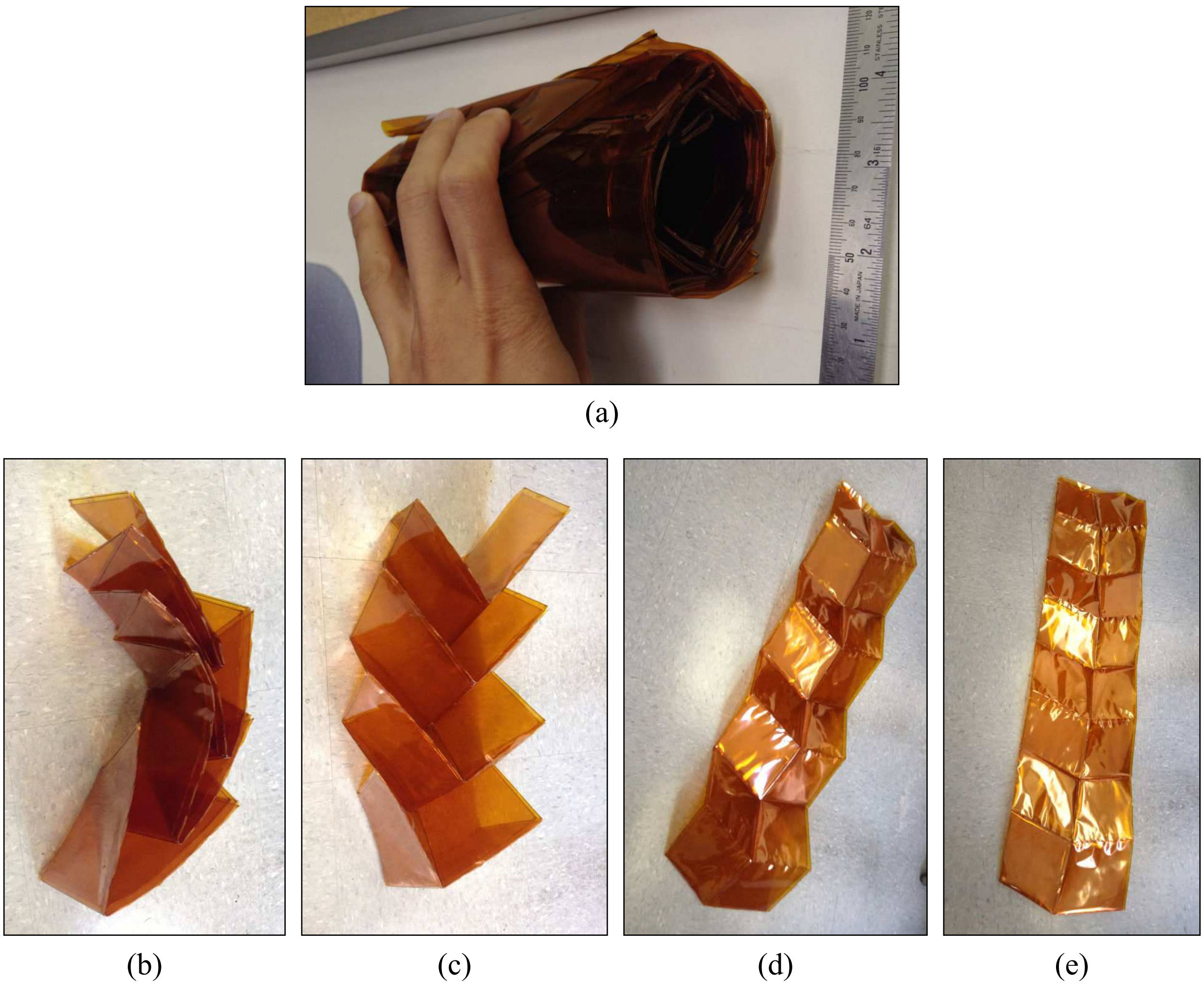

Figure 2. Prototype membrane structure in several stages of deployment. (a) The packaged structure can be coiled into a package with diameter less than 10 cm. (b)-(e) As the membrane unfolds, it flattens into a structure 29.2 cm in width and 124.8 cm in length with the two membranes separated by 1.27 cm.

B. Membrane-based Patch Antenna Array

A phased array patch antenna system has been developed at the Jet Propulsion Laboratory for L-band (1.26 GHz) SAR applications.[13] These antenna systems are envisaged for Earth-observation missions at medium or geostationary Earth orbit (MEO or GEO), where larger arrays are required than at low Earth orbit (LEO). The higher altitude allows for revisit times on the order of minutes suitable for disaster response or future study of earthquake physics.[12]

Active arrays of up to 256 elements (in a 16 × 16 rectangular array) have been tested using phase-shifting transmit/receive (T/R) modules to electronically steer the main beam up to 30°.[13] This antenna array is composed of two membrane layers, with the radio frequency feed network, T/R electronics and ground plane on one membrane, and radiating patches on the other. Slots in the ground plane allow the feed network to couple with the radiating patches so that no *physical* electrical connection is required between the layers. The patch elements are 8.89 cm (3.5") square, positioned in a rectangular array with a spacing of 15.24 cm (6"). Previous passive antenna designs have also used a three-layer configuration so that the feed network is placed a greater distance away from the ground plane.[14]

These prototypes were designed with 50 μm DuPont™ Kapton® polyimide film[a] as the membrane substrate. Thinner membranes would require a corresponding decrease in the width of the feed network to maintain impedance, and is limited by fabrication constraints. The most recent prototypes have used conventional flexible printed circuit board (PCB) fabrication techniques by etching a copper foil layer. Potential avenues for overcoming this constraint could involve alternative circuit fabrication techniques, such as materials printing with conductive inks.

We used the existing two-layer antenna array design to motivate the development of the multi-layered membrane structure described in this paper. This deployable structure, using the crease pattern described in the next section, provides one possible approach toward implementing the antenna array as a spacecraft payload.

III. Membrane Crease Design

In order to allow the membrane structure with multiple layers to collapse and lie flat, we chose to use the same crease pattern on all layers. The crease pattern for each membrane is based on the beech leaf fold described by Kobayashi et al.[15] and shown in Figure 3. In this section, we describe the general parameters governing the folding behavior of this crease pattern, as well as the modifications necessary to allow the folded membrane to wrap smoothly around a spool while accounting for the membrane thickness τ. We then describe the specific crease pattern selected to be compatible with the antenna array design. Finally, we discuss alternative possibilities for arranging multiple membrane layers in the structure.

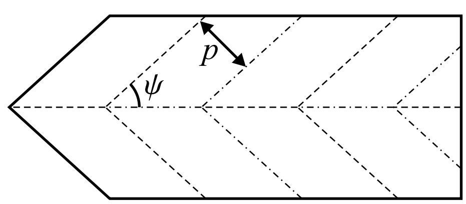

Figure 3. Kobayashi's beech leaf folding pattern with relevant parameters illustrated. Valley folds are denoted with dashed lines and mountain folds with dash-dotted lines. Parameters that can be varied include the crease spacing p and the crease angle ψ.

A. General Crease Pattern

The beech leaf folding pattern has two sets of diagonal creases. Each crease intersects with one from the opposite set at a centerline crease, which alternates between mountain and valley folds. The fold pattern is determined only by the spacing between the diagonal creases and by the angle they make with the centerline crease. This angle ψ between the centerline crease and the diagonal creases is constrained between 0° and 90°, with 0° corresponding to the degenerate case where the diagonal creases are parallel to the centerline and folding does not occur, and 90° corresponding to the case of maximum longitudinal compression along the centerline. To attach membrane layers to each other, vertical ribs can be attached along the diagonal creases. However, this requires that the crease angles remain constant so that the creases are parallel. The crease separation distance p is also usually constant and can be selected to provide a height $p \sin\psi$ of the folded membrane configuration.

[a]DuPont™ and Kapton® are trademarks or registered trademarks of E.I. du Pont de Nemours and Company

By keeping the parameters constant over all creases, the folded configuration will have a uniform height, which simplifies the packaging process. Additionally, for some applications such as solar panels, components of a constant size must be embedded on the membrane between creases, and is more straightforward to implement on a membrane with creases at a constant spacing. However, by allowing the crease angles and separation distances to vary, it is possible to achieve favorable deployment dynamics. The kinetic energy associated with deployment varies as the deployment angle θ goes from 0° to 90°, and is greatest near the end of deployment when $\theta \approx 90°$.[16] With a folding pattern that has smaller crease angles at the root of the membrane and larger angles at the tip, the deployment energy profile can be tuned for greater uniformity.

The straight line crease patterns can then be adapted using curved creases to coil smoothly so that they can be packaged on a spool. The technique to determine the crease curvature has been developed previously by Lee and Close[11] and is based on the principle of computing the crease length in the coiled configuration to determine its required curvature in the unfolded configuration. A similar finding was determined through empirical folding experiments by Satou and Furuya.[17] However, the algorithm needs to be adapted to the properties of this particular crease pattern. Specifically, the reference center line for the beech leaf crease pattern does not remain horizontally in the same plane; it zig-zags across the height of the pleat as depicted in Figure 4. This produces a longitudinal compression in the folded membrane, and results in a crease that must lie along a helical spiral in the coiled configuration.

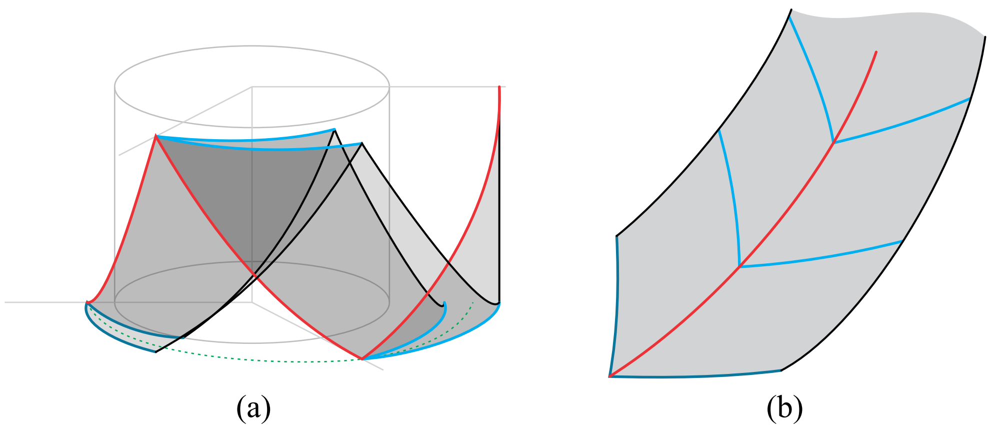

Figure 4. Sketch of the curved crease geometry in its (a) wrapped and (b) flattened configurations. The center line crease (in red) traverses along helical spiral segments as the membrane wraps around a hub. The diagonal creases (in blue) remain in a horizontal plane, but alternate creases lie on different planes.

For a structure geometry where the length is greater than the width, we can assume that the thickness of the folded membrane configuration is roughly constant and can approximate the coiled radius of the centerline as an Archimedes' spiral of the form

$$r(\theta) = r(0) + \frac{r(2\pi) - r(0)}{2\pi}\theta = r(0) + b\theta, \tag{1}$$

where θ is the angular coordinate around the hub, b is the spiral rate parameter, and $r(0)$ is the initial radius. For a total folded thickness $2h$, we have the rate parameter $b = h/\pi$. However, unlike the previous work, the path length of the crease must be projected in 3D such that

$$\begin{aligned} \xi(\theta)\cos\psi = &\frac{(b\theta + r(0))\sqrt{b^2 + (b\theta + r(0))^2}}{2b} \\ &+ \frac{1}{2}b\ln\frac{\sqrt{b^2 + (b\theta + r(0))^2} + b\theta + r(0)}{\sqrt{b^2 + r(0)^2} + r(0)} \\ &- \frac{r(0)\sqrt{b^2 + r(0)^2}}{2b}, \end{aligned} \tag{2}$$

where the right-hand side is the closed form path length of the Archimedes' spiral. The curvature of the spiral is

$$\kappa = \frac{(2 + (\theta + r(0)/b)^2)}{b(1 + (\theta + r(0)/b)^2)^{3/2}}, \tag{3}$$

which can be related to the crease radius of curvature R using the relation

$$R = \left(\frac{p}{\tau}\right)\frac{1}{\kappa}. \tag{4}$$

The diagonal creases in the folding pattern *do* remain in a horizontal plane when the membrane is folded, and their curvature is therefore described as above but without the $\cos\psi$ projection.

Figure 5 contains a folding pattern developed using this algorithm. A similar pattern was used to fold the paper model in Figure 6, which demonstrates the ability of the folded membrane to wrap tightly and smoothly. To assess the effectiveness of this folding strategy, the packing efficiency is estimated as the volume of membrane material divided by the smallest volume of an encompassing rectangular prism. A paper membrane with an area of 400 cm^2 and thickness of 0.11 mm has a volume of 4.4 cm^3, and was packaged into a roll with a diameter of 2.3 cm and a height of 1.5 cm, which can be contained within a rectangular volume of 7.94 cm^3. This is a packing efficiency of 55%, which includes volumes within the spool and in the corners of the box that remain usable.

B. Crease Pattern for Membrane Antenna Array

With the membrane antenna array described in Section II.B, a practical consideration is that the creases may degrade the performance of the antenna by affecting the geometry or even the conductivity of the radiating elements. Additionally, the existing design uses T/R modules that could not be creased with the membrane. We therefore designed a crease pattern choosing parameters that would avoid creases overlapping with either the T/R modules or the patches. The goal for this design was to fit a 2×8 array onto a membrane that could package inside a 3U CubeSat volume ($10 \times 10 \times 34.5$ cm). With the 15.24 cm antenna spacing in two dimensions, a rigid-foldable pattern based around the patches, where individual panels do not bend, would not fit within the prescribed volume. However, the

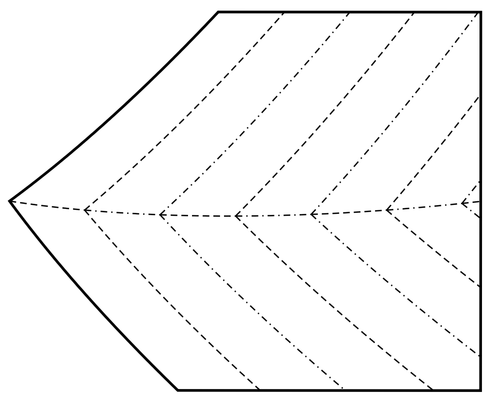

Figure 5. Beech leaf folding pattern with curved creases to enable wrapping in the folded configuration. Valley folds are denoted with dashed lines and mountain folds with dash-dotted lines. In this crease pattern, the crease angle ψ has been chosen to be 45°.

(a) (b) (c)

Figure 6. Paper prototype of a two-layer structure using a curved beech leaf crease pattern. These three photos show (a) the initial wrapped membrane, (b) an intermediate stage during deployment, and (c) the final deployed structure.

use of the curved crease pattern permits one linear dimension to wrap around a spool, while the other can occupy the longest dimension of the CubeSat volume.

For this crease design, the free parameters available in the design space include the crease angle ψ, the spiral parameter b, and the spool radius r_0. In order to fit the diagonal creases between the patches, the angle ψ must be greater than 54°. However, having a large crease angle will result in a thicker folded membrane package, which would be more difficult to coil. A crease angle of 75° was selected as a compromise between these two competing objectives. The spiral parameter was computed by estimating a total folded membrane thickness of 4 mm, accounting for the additional thickness necessary to embed electronics on the surface. This yields a spiral rate of 4 mm per revolution, or 0.64 mm per radian. Because of the limited space between the two rows of patches, we desired a centerline crease with as little curvature as possible. This was accomplished by selecting the largest possible spool radius that would result in a wrapped membrane still satisfying the 10 × 10 cm CubeSat constraint. These geometric constraints are depicted in Figure 7. A spool radius of 4 cm was found to be adequate to satisfy the design requirements. Using these parameters, the curved crease pattern was produced, and overlaid on the rectangular patch antenna array, as shown in Figure 8.

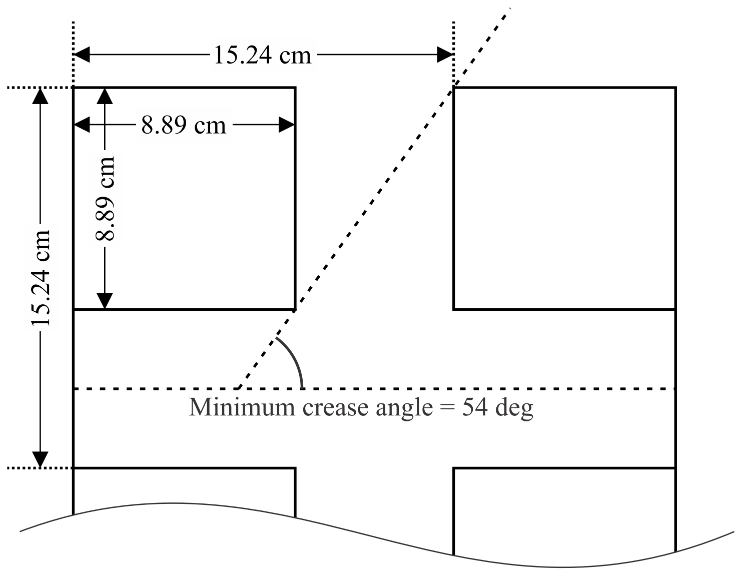

Figure 7. Antenna array dimensions and constraints on crease geometry. Each radiating patch is a square with a side length of 8.89 cm. The patches are spaced in a rectangular array at intervals of 15.24 cm in both directions. In order to avoid creasing the patch, the minimum crease angle possible using a straight-line beech leaf crease pattern is approximately 54°. When implementing a curved crease pattern, the centerline must lie within the 6.35 cm gap between patches.

C. Arrangement of Multiple Membrane Layers

Using the beech leaf folding pattern with a constant crease angle, the diagonal creases remain parallel and horizontal as the membrane folds. The corresponding diagonal creases on parallel membranes with the same crease pattern would therefore remain the same distance apart. In order to construct a multi-layered structure, these diagonal creases can be joined by a vertical rib. As the membrane structure folds, each of the rectangular cells formed by two horizontal membrane panels and the two ribs connecting them would be able to shear and flatten and the two membranes will nest inside each others folds. The overall thickness of the structure and the spacing between the membranes can be arbitrarily selected by choosing the appropriate rib height.

However, it is not necessary to place ribs on every diagonal crease, or even only on the creases. Depending on the geometry of the structure and the stiffness of the materials used, it may be more appropriate to place ribs at every other crease if the crease spacing is small, or to add additional ribs in between creases if the crease spacing is large. If ribs are placed only at ever other crease, then they will all stack together in the folded structure rather than in two separate groups in the case of ribs at every crease. If additional ribs are necessary, the design would be equivalent to reducing the diagonal crease spacing in the pattern but leaving some of these creases unfolded.

In the case of a two-layer membrane, another alternative arrangement would be to have the membranes folded in an opposite sense, with valley folds on one membrane corresponding to mountain folds on the other, and vice versa.

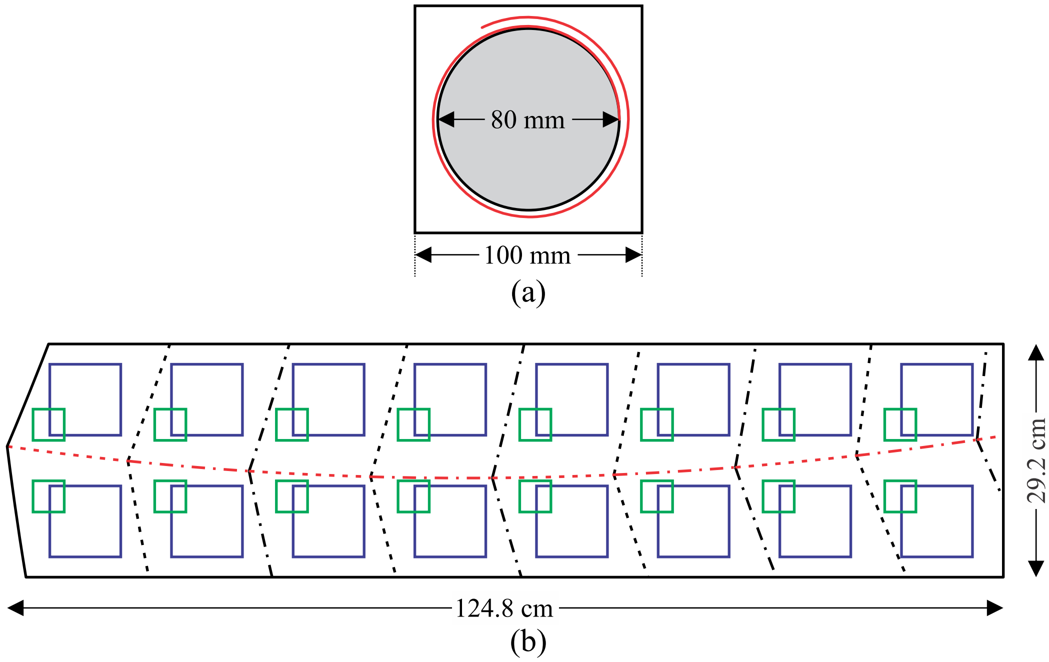

Figure 8. Design for a crease pattern compatible with the antenna array geometry. (a) Packaged configuration showing the centerline crease in red, the round spool (4 cm radius) in gray, and the CubeSat constraints (10 cm square). (b) The crease pattern with antenna components. The centerline crease is shown in red, the radiating patches in blue, and the T/R modules in green. Valley folds are denoted with dashed lines and mountain folds with dash-dotted lines.

This would result in a more symmetrical but taller folded package. This could be beneficial if certain parts of the membrane cannot be folded against each other or if the membrane contains thicker elements that do not stack well in the folded package.

IV. Prototype Fabrication

We used the crease pattern described in the previous section to construct a prototype membrane structure that could support a 2×8 patch antenna array based on the JPL design described in Section II.B. This prototype was constructed using 50 µm thick Kapton® polyimide film to be consistent with the JPL design. In order to assemble the components of the structure, we chose to use a continuous membrane for one layer, and to cut the other layer into separate panels based on the locations of the ribs. The ribs were attached first to the continuous layer, and then the second layer was attached segment by segment onto the ribs. This is representative of a potential assembly process for the antenna array, since the design includes one continuous layer with the feed network and ground plane, while the other layer only has radiating patches that do not require a physical electrical connection (such as a wire or microstrip trace) to the other membrane or to other locations within the same membrane.

Because of the geometry for this particular design, where the rib length is short relative to the rib spacing, there is a greater tendency for the membrane layers to buckle between the ribs than if the ribs were more closely spaced. To mitigate this effect, thin carbon fiber rods (0.50 mm diameter) were used to stiffen the edges of the membrane. These rods were cut to length based on the crease length of each segment, and were attached along the edges as well as on the longitudinal crease down the center of the structure. Each rod was bonded to the membrane using cyanoacrylate adhesive at the end points and the middle. The rods along the edge of the structure were reinforced with small tabs of polyimide tape to prevent delamination from the membrane. Photos of the prototype fabrication process are included in Figure 9.

The prototype design demonstrated qualitatively good ability to fold and wrap. In total, it was 59 g in mass and covered an area of 0.35 m^2. This areal density of 0.7 kg/m^2 does not include any supporting structure or the hub, but is very promising in reducing the mass of large planar structures from the current state-of-the-art rigid panel technologies. In order to quantify the deployment behavior of this structure, we conducted deployment experiments with a force sensor, described in the following section.

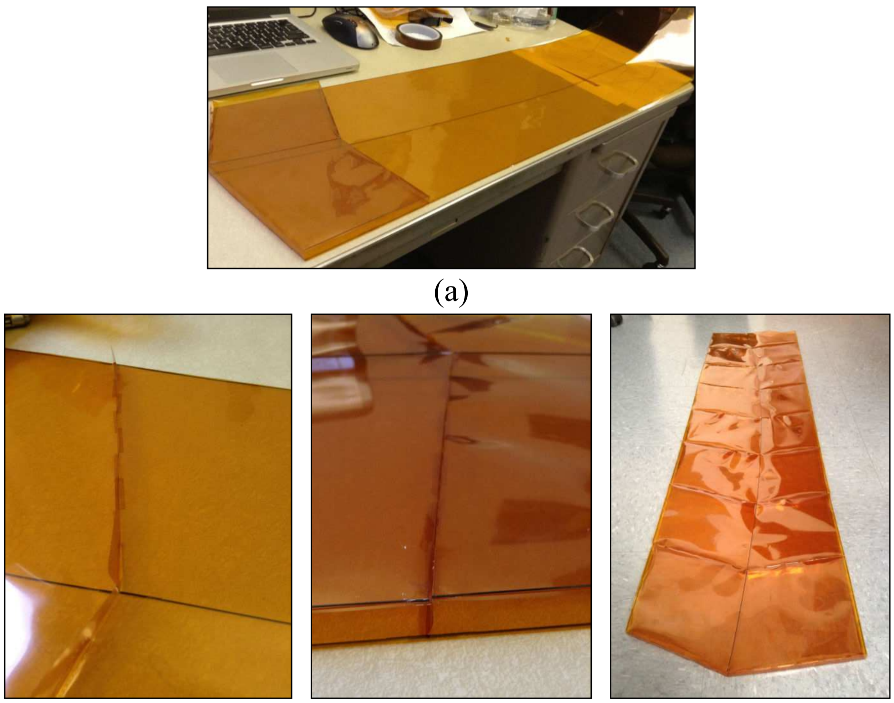

(a) (b) (c) (d)

Figure 9. Membrane structure fabrication. (a) The bottom membrane layer is a continuous sheet of Kapton® while the top layer is separated into eight panels. (b) Ribs are attached to the bottom layer with short segments of polyimide tape. The top panels are attached in a similar manner to the ribs. (c) Thin carbon rods are attached on the edge of the membrane structure and along the centerline crease in order to stiffen the individual panels. (d) The completed membrane structure.

V. Deployment Experiments

To study the deployment force profile of the membrane structure described in Section IV, the prototype was deployed using a materials testing machine. In order to characterize the forces associated with unwrapping the membrane from a spool, two configurations were tested: the membrane was deployed first from a folded state without being wrapped around a spool, and then from a wrapped and folded state around a rotating hub.

An Instron model 5569 materials testing machine was used to perform the deployment experiments. Because the total length of the membrane structure exceeded the total length of travel of the machine, different configurations were used to study the deployment. The load cell used (model 2525-808) has a range of ±10 N, with accuracy better than 2.5 mN for indicated loads below 1N, or 0.25% of the indicated load for values greater than 1 N.[18] The load cell can be sampled at an adaptive rate depending on the slope of the previous measurements, up to a maximum of 500 Hz.

The membrane was attached to the load cell using a screw and nut, with a total mass of 4.6 g, connected to a short tab at the tip (midpoint of the deployed end) of the membrane structure. For the unfolding configuration, the root of the membrane structure was fixed to the table surface in front of the machine (28 cm forward and 19 mm below the base of the machine's lowest point of travel). By anchoring the structure below the base of the machine, we were able to capture the end of deployment before reaching the upper limit of travel. However, at the start of the test, the membrane was already deployed to a length of 37 cm. Figure 10 shows the setup for this deployment configuration.

For the unwrapping configuration, a spool was mounted in the machine, centered below the load cell and with the axis of rotation horizontal and 10 cm above the machine's lowest point of travel. The spool is a 5.08 cm (2") diameter aluminum tube with plastic conveyer roller end caps mounted via bushings onto a threaded rod. The mass of the rotating part of the spool is 163.1 g. In order to prevent the membrane structure from unwinding off the spool, it was necessary to impart an external moment on the spool. This was implemented using the counterweight of a 100 g mass on a string, with a pulley used to allow the weight to extend beyond the edge of the table. The string was attached to the surface of the spool and wrapped around it in the opposite direction as the membrane structure. A schematic of the unwrapping configuration is shown in Figure 11 with photos of the setup in Figure 12. Neglecting the transient effect of accelerating the mass up and down as the spool rotates, this configuration provided a constant 25 mNm torque on the spool. Because the spool for the unwrapping configuration is mounted closer to the load cell than the root anchor point in the unfolding configuration, the deployments could start at a deployed length of 10 cm, but could only deploy to a length of 100 cm and not reach the fully deployed length of 125 cm. Deployments were performed at constant speeds ranging from 1 mm/s to 8 mm/s with force measurements sampled at the maximum rate of 500 Hz. During several deployments, video was captured simultaneously. In this paper, results will be discussed from fifteen deployments: eight that were performed from the unfolding configuration, and seven from the unwrapping configuration.

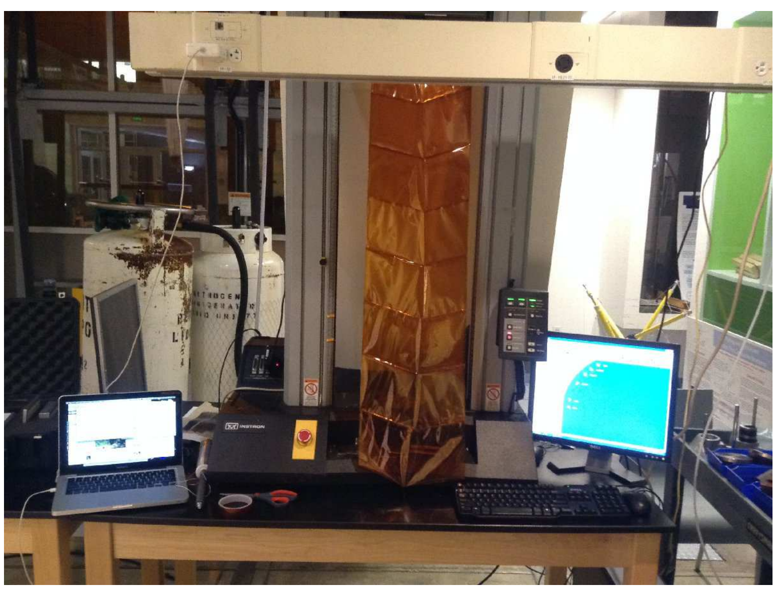

Figure 10. Photo of the membrane structure deployed from the unfolding configuration. The root of the structure was attached to the table in front of the materials testing machine. The tip was attached to the load cell in the machine.

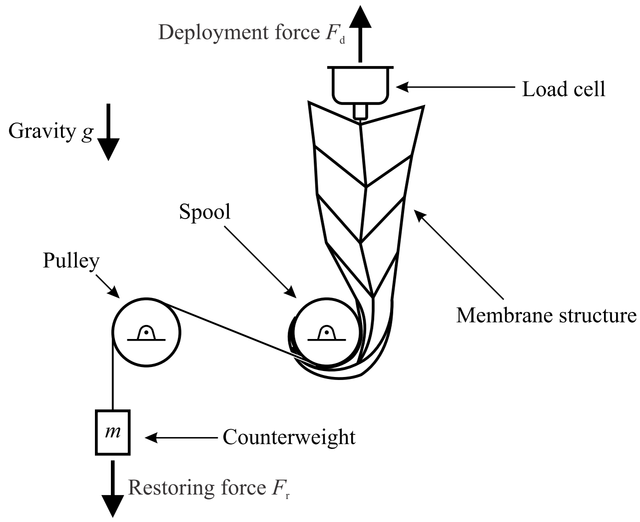

Figure 11. Drawing of the components in the unwrapping configuration. The membrane was attached at the tip to the load cell, and at the root to a spool. The spool was attached to a counterweight through a pulley in order to keep the membrane from unwinding around the spool.

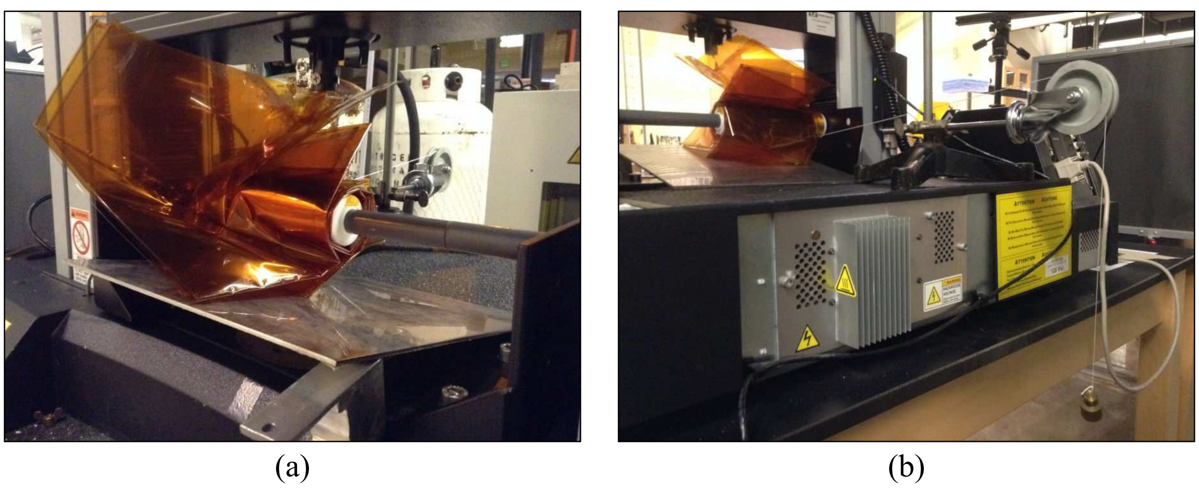

Figure 12. Two photos of the experimental setup for the unwrapping configuration, from the (a) front and (b) back of the materials testing machine. The counterweight and pulley can be seen at the back of the machine. An aluminum plate was used to provide a smooth base from which to deploy, so that the membrane would not catch on the fixtures present below the plate.

VI. Experimental Results

With the data collected as described in the previous section, the force profiles for the deployments showed several notable characteristics. The raw measurements are shown in Figure 13. First, the unfolding configuration resulted in a gradual increase in the measured deployment force with a transition to a sharper increase near the end. The gradual increase is attributed primarily to the self weight of the membrane. Second, the unwrapping configuration resulted in a deployment force profile that has several peaks corresponding to the unfolding of the lateral creases in the membrane structure. Finally, during the portions of the unwrapping deployment where the force is generally decreasing, the shape of the force profile is punctuated by a characteristic sawtooth shape with a rapid drop followed by a gradual increase. This can be seen in Figure 14, which shows the deployment force profile for an unwrapping deployment at a rate of 1 mm/s. There is one particular unfolding panel where this does not occur; this anomalous behavior occurred consistently over multiple deployments at a deployment length of 50 to 70 cm, always on the fourth out of seven panels deployed. The data were adjusted to account for disturbances and biases, including the self weight of the membrane and the moment applied to the spool. These were both approximated as linear functions with respect to deployed length. The corrected measurements are shown in Figure 15. Figure 16 shows one unfolding and one unwrapping deployment force profile, along with images of the deployment at 20 cm intervals.

In the following sections, we will look first at the global deployment force profile and how it varies throughout the deployment for the two experimental configurations, and then analyze in more detail the local dynamic behavior that can be seen in some of the measurements.

A. Global deployment force profile

The deployment force profiles appear quite different for the wrapped and unwrapped configurations. When the membrane is only folded but not wrapped around the hub, the deployment force remains quite small and relatively constant. When it is wrapped around the hub, a periodic spike in the deployment force appears, corresponding to the periodicity of the crease pattern. The reason for this increased deployment force compared to the unfolding configuration is that the crease pattern is derived from a Miura-ori design.[20] In a conventional Miura-ori fold pattern, the folded membrane behaves as a single degree-of-freedom mechanism: all panels unfold simultaneously. However,

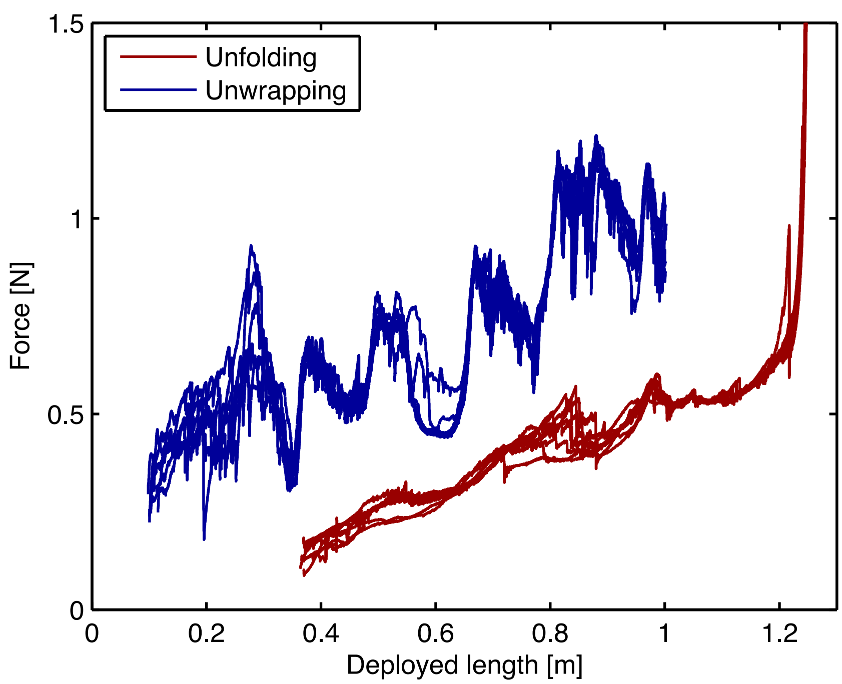

Figure 13. Plot of raw force measurements for all deployments with respect to deployed length. This includes eight unfolding deployments and seven unwrapping deployments.

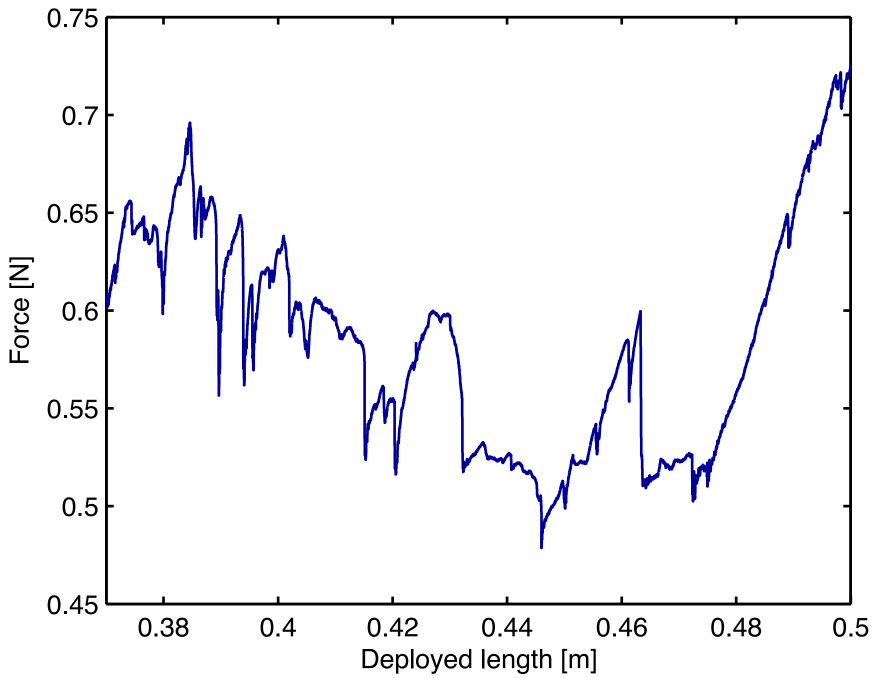

Figure 14. Plot of force measurements for an unwrapping deployment at 1 mm/s. From a deployed length of 37 cm to approximately 47 cm, the deployment force shows a global decrease with characteristic transient features. From 47 cm to 50 cm, the deployment force increases globally and shows fewer of the transients.

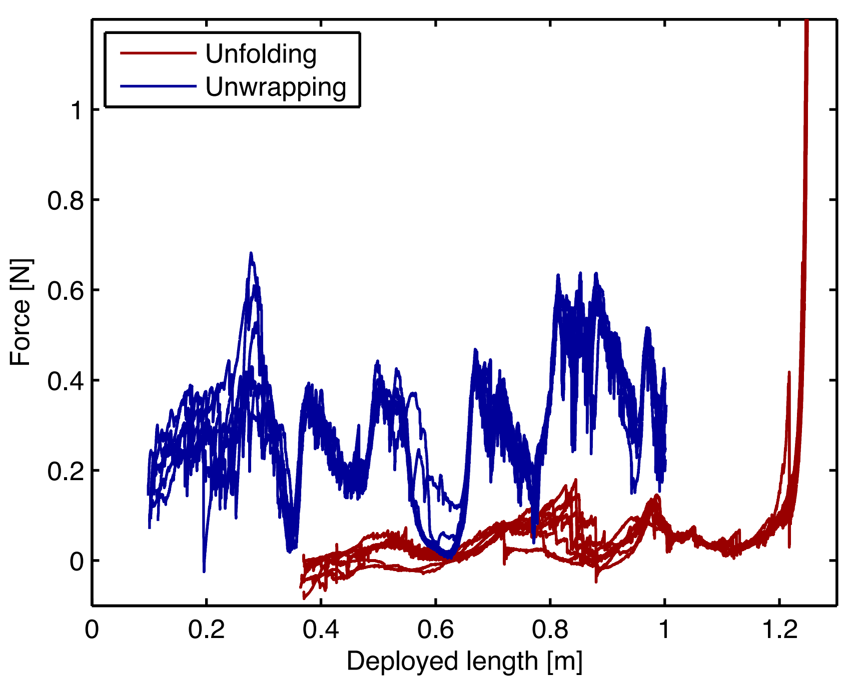

Figure 15. Plot of corrected force measurements for all deployments with respect to deployed length. This includes eight unfolding deployments and seven unwrapping deployments and have been adjusted to remove the effect of self weight of the membrane structure, and for the unwrapping configuration also the effect of the counterweight.

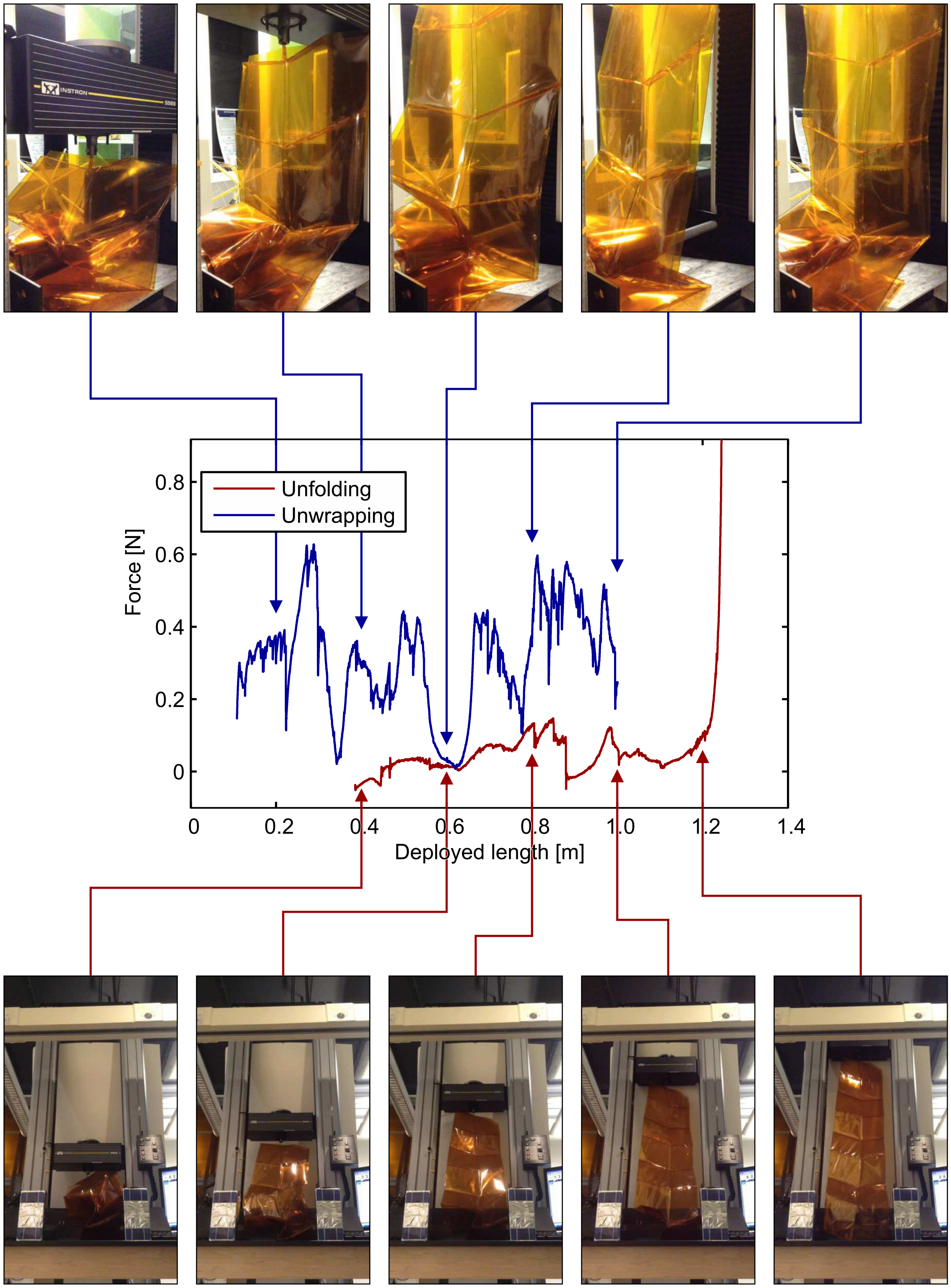

Figure 16. Plot of corrected force measurements for two deployments with respect to deployed length, with photos of the deployed membrane structure. The unfolding deployment, shown in red with the photos below the plot, was performed at 5 mm/s. The unwrapping deployment, shown in blue with the photos above the plot, was performed at 4 mm/s. The photos are shown at equally spaced intervals of 20 cm deployed length for each of the configurations.

in this curved design, the spool prevents the wrapped portion of the structure from unfolding. As a result, each panel must be peeled away from the adjacent panel on the spool, resulting in significant buckling of the membrane surface. As these buckles propagate and the panel lifts off of the spool, the deployment force decreases until the next panel starts to peel away from the spool and the cycle repeats.

The peeling behavior of the wrapped membrane structure results in a deployment force profile that has peaks typically ranging from 0.4 N to 0.8 N, with some spurious peaks up to 1.2 N. This is about an order of magnitude greater than the 0.1 N amplitudes observed in deployment profiles of the unfolding configuration. However, the force required at the end of deployment can greatly exceed the peaks observed in the unwrapping profile, depending on the desired tension or flatness of the membrane. For a practical design, the peaks determine the lower bound of a force profile that would be required to fully deploy the structure. If an actuator did not exert the required force throughout, the deployment would likely be arrested. For a constant force actuator, the deployment force would be determined by the required flatness at the end of deployment, and the fact that the wrapped configuration has a more complex force profile would not be a concern.

From the unfolding configuration, we can see that the deployment force during the final 5% of total deployed length exhibits a sharp increase in slope. This is indicative of the transition from an unfolding mechanism, where hinge moments and membrane buckling provide the dominant resistive force, to a structural process, where the elasticity of the membrane material becomes dominant, and is similar to results obtained for a different crease pattern by Papa and Pellegrino.[19]

B. Local dynamic behavior

Within the global behavior of the force profiles for the unwrapping configuration, the regions of decreasing deployment force are predominantly characterized by a sawtooth shape. To study the dynamics of the membrane deployment within this period, we used the spectrogram function in MATLAB® to visualize the frequency spectrum of the force profile over time for a series of deployments at rates of 1, 4, and 8 mm/s. These spectrograms use a series of discrete Fourier transforms within a sliding window over the temporal signal. The phase of the spectrogram highlights the characteristic sawtooth transients that occur during the periods of overall decreasing deployment force. Because of the impulsive nature of these features, we expect to see a short period of coherency (constant phase) across a large band in frequency. Spectrograms are plotted for five deployments in Figure 17. Each sawtooth feature corresponds to a transient dynamic event in the membrane deployment. This is attributed to kinks in the membrane that propagate along the surface in short spurts, each time producing a vibration in the structure. For the slowest deployment at 1 mm/s, it appears that many of these features are distinct; the response from one sawtooth is often mostly damped out before the next one occurs. In the faster deployments, there is more overlap between features. This can be seen in a closer view of the spectrogram phase plots in Figure 18. However, the amplitude of the features does not seem to be dependent on deployment rate within the range tested.

In order to better understand the "anomalous" smooth profile associated with the deployment of the fourth panel, the video of the deployment process was analyzed. This panel appears to have unfolded off the spool with significantly less wrinkling than the other panels, as can be seen in Figure 19. This was a result of at least two factors. First, the spool was aligned such that the root of the structure was directly underneath the load cell where the tip was attached. Every other panel was therefore pulled out of the spool at a slightly different angle. The even-numbered panels were unfolded with a force that was better aligned with the direction the panels were moving than the odd-numbered panels. Second, because of the curvature of the centerline crease, each panel width is slightly different on one side of the structure. With the fourth panel, the centerline crease was at its maximum offset from the true centerline of the structure, and there was correspondingly less interaction between that panel and the baseplate.

These findings provide several insights into the requirements for a practical deployment design. Within the range of deployment speeds tested, there does not appear to be any benefit to a slower deployment in reducing the amplitude of the deployment force profile. However, a slower deployment will cause more of the disturbance vibrations from a buckled membrane to damp out before the next impulsive event occurs. For a membrane design that is only characterized to be robust to specific vibration environments, it might be beneficial to avoid the more complex dynamics of interacting vibrations that occur with a faster deployment. Additionally, the housing around a packaged membrane can affect how much wrinkling and buckling will occur in the unfolding panels as the membrane structure deploys. A tight housing will keep the wrapped portion of the membrane closer to the spool and will force each panel to deform more significantly in order to unfold. Ideally, upon deployment, a container holding the membrane would retract completely to avoid adding additional constraints on the deployment process.

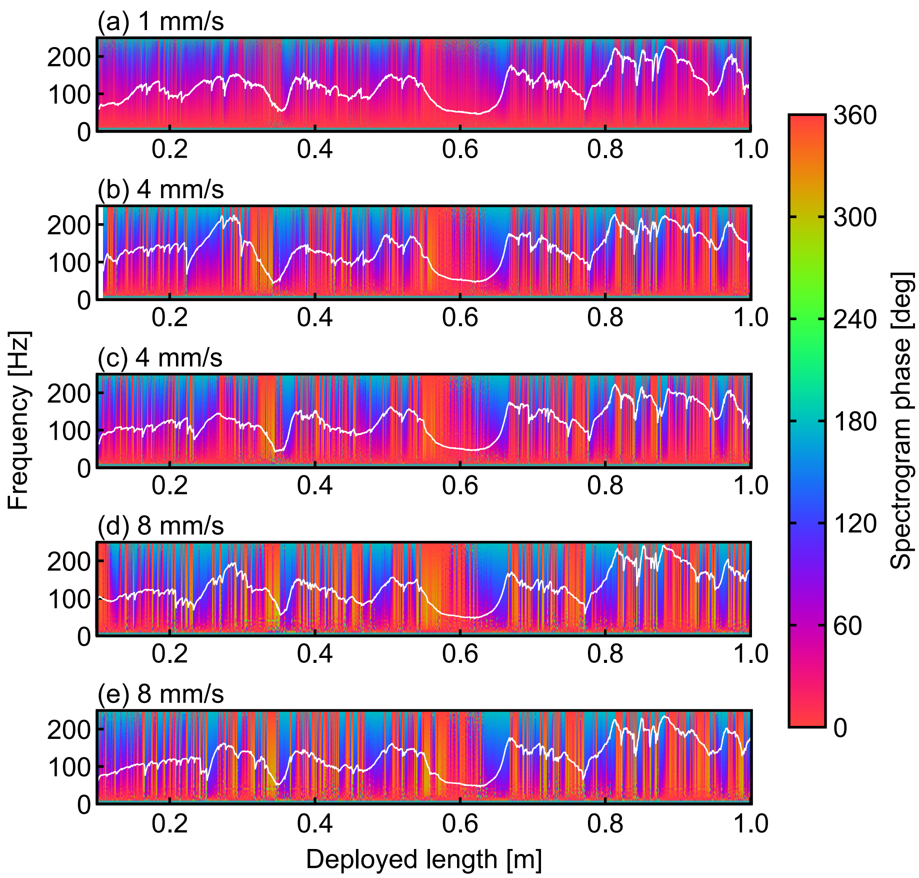

Figure 17. Plot of spectrogram phase for five unwrapping deployments, plotted against deployment length on the horizontal axis. From top to bottom, the deployment rates are (a) 1, (b) 4, (c) 4, (d) 8, and (e) 8 mm/s. The phases are computed from temporal spectrograms with a constant time sliding window of 100 data points, or 0.2 seconds. The slower deployments therefore show a higher spatial resolution over a longer total deployment time. The force measurement is overlaid as the white line on each corresponding spectrogram plot.

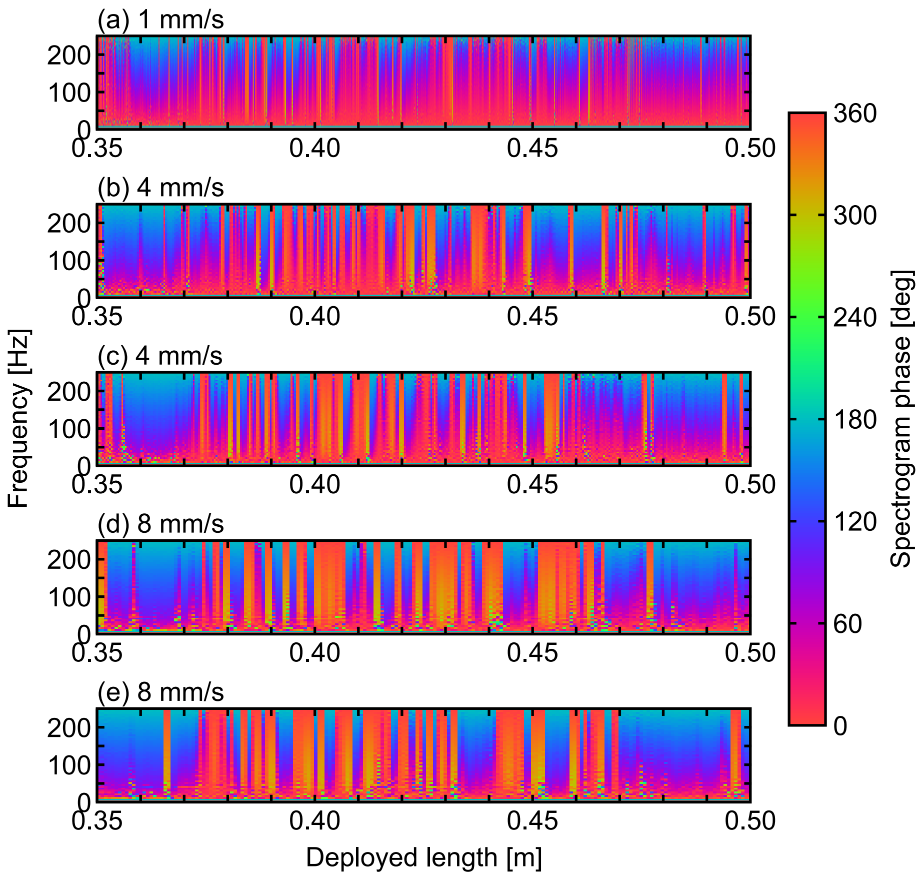

Figure 18. Close up of spectrogram phase for five unwrapping deployments, plotted against deployment length between 0.35 and 0.5 m on the horizontal axis. From top to bottom, the deployment rates are (a) 1, (b) 4, (c) 4, (d) 8, and (e) 8 mm/s. The data are the same as those shown in Figure 17.

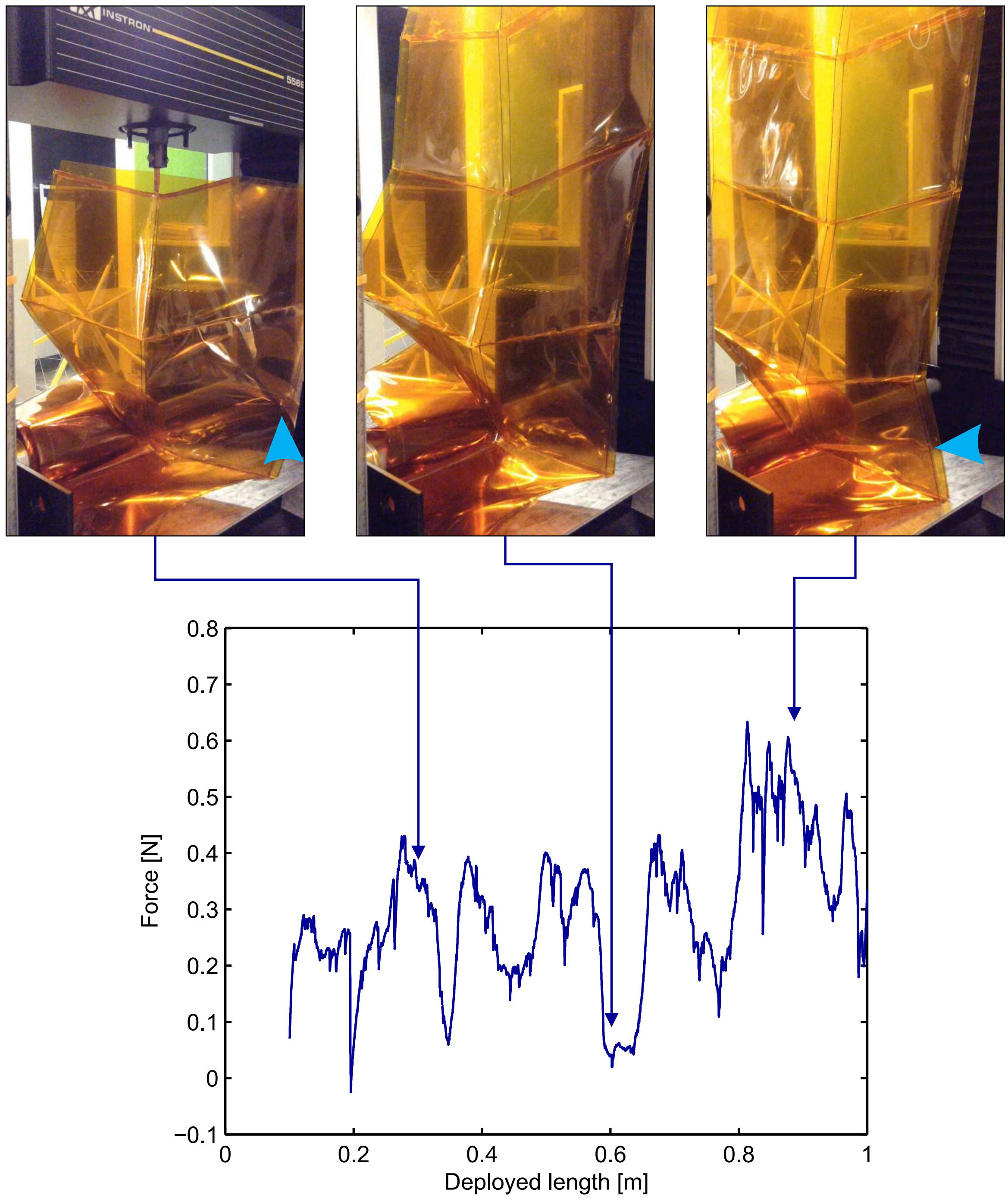

Figure 19. Plot of corrected force measurements for one unwrapping deployment with respect to deployed length, with photos of the deployed membrane structure. The three photos show the second, fourth, and sixth panels unfolding from the spool. In the first and third photos, membrane buckling can be seen, as indicated by the blue arrowheads. The deployment of the fourth panel, without as much buckling, resulted in a lower and smoother force profile.

VII. Conclusions

We have presented a potential membrane structure that is compatible with an existing antenna array design and can be folded and wrapped around a round hub. Through deployment experiments, we measured the deployment force profiles of a prototype membrane structure as it deploys from being wrapped around a spool and as it unfolds without any external constraints. We found that the deployment force required to unwrap the membrane from a spool was an order of magnitude greater than the unfolding force, and that the local dynamic behavior can depend greatly on small deviations in the crease pattern. In the future, we plan to study in more detail the phenomena that occur through the unwrapping process and to better understand the dynamics involved that can affect deployment success.

The membrane structure as designed shows promise in its ability to package panels into a small volume, but further experimentation is required to determine its suitability for deployment with embedded electronics. As a structure supporting an antenna array, the achievable flatness of the membrane surface will need to be characterized.

In addition to the antenna application discussed throughout this paper, this membrane structure design is suitable for other applications, and especially for small spacecraft such as CubeSats, where the size constraints drive many systems to depend on deployable structures. The use of a deployable membrane structure with flexible photovoltaic cells or embedded RF elements has the potential to greatly exceed the size of state-of-the-art hinged solar panels or communications antennas for CubeSats. The geometry of the general folding pattern, with continuous uncreased sections along the membrane exceeding the dimensions of the packaged volume, can be conducive to embedding electronic components within and on the surface of the structure. The thickness of these components is easily accommodated in the crease design in order to ensure optimal packing efficiency. Additionally, the flexibility in the crease geometry allows each design parameter (rib spacing, crease spacing, and crease angle) to be independently determined by the particular application.

A particular future application of this deployable structure is the capture of small space debris particles between 10 and 100 μm. The growing population of debris is gaining prominence as a significant threat to spacecraft operations, and many different technologies are being proposed to address the problem of active debris removal. The cellular nature of the deployable membrane structure can serve to catch and contain debris particles that a satellite encounters. The two membrane surfaces act as a Whipple shield, fragmenting particles as they penetrate one membrane such that they cannot exit the other side. The fragmented ejecta will therefore remain contained between the membranes and can be further contained by charging the ribs to sweep up the fragments electrostatically. Simultaneously, such a deployed lightweight system on a CubeSat will increase its aerodynamic drag, allowing the spacecraft to launch into higher orbits and maintain compliance with spacecraft lifetime guidelines.

Acknowledgment

N. Lee was supported through this work by a postdoctoral fellowship from the W. M. Keck Institute for Space Studies. We thank P. Arakelian for his assistance with the experimental setup.

References

[1]Clark, S., “"Solar panel shakes loose on Intelsat broadcast satellite," from Spaceflight Now,” See http://http://spaceflightnow.com/sealaunch/is19/120619array/, 2012.

[2]Miyoshi, K., “Aerospace mechanisms and tribology technology: case study,” *Tribology international*, Vol. 32, No. 11, 1999, pp. 673–685.

[3]de Selding, P. B., “"SkyTerra 1’s Antenna Nearly Fully Deployed," from Space News,” See http://www.spacenews.com/article/skyterra-1s-antenna-nearly-fully-deployed, 2010.

[4]Hoyt, R., Newton, T., Barnes, I., Shepherd, J., Frank, S. S., Slostad, J., Jaroux, B., Twiggs, R., et al., “Early Results of the Multi-Application Survivable Tether (MAST) Space Tether Experiment,” *21st Annual AIAA/USU Conference on Small Satellites*, 2007.

[5]Gilchrist, B. E., Bonifazi, C., Bilen, S. G., Raitt, W. J., Burke, W. J., Stone, N. H., and Lebreton, J. P., “Enhanced electrodynamic tether currents due to electron emission from a neutral gas discharge: Results from the TSS-1R Mission,” *Geophysical Research Letters*, Vol. 25, No. 4, 1998, pp. 437–440.

[6]Garner, C., Diedrich, B., and Leipold, M., “A Summary of Solar Sail Technology Developments and Proposed Demonstration Missions,” *AIAA/ASME/SAE/ASEE, 35th Joint Propulsion Conference and Exhibit*, 1999.

[7]Freeland, R. E., Bilyeu, G. D., Veal, G. R., Steiner, M. D., and Carson, D. E., “Large inflatable deployable antenna flight experiment results,” *Acta Astronautica*, Vol. 41, No. 4, 1997, pp. 267–277.

[8]Guest, S. D. and Pellegrino, S., “Inextensional wrapping of flat membranes,” *Structural Morphology: Proc. 1st Int. Sem. Struct. Morphol.*, Montpellier, September 1992, pp. 203–215.

[9]Furuya, H., Inoue, Y., and Masuoka, T., “Deployment Characteristics of Rotationally Skew Fold Membrane for Spinning Solar Sail,” *46th AIAA/ASME/ASCE/AHS/ASC Structures, Structural Dynamics, & Materials Conference*, AIAA, Austin, TX, 18–21 April 2005.

[10]Zirbel, S. A., Lang, R. J., Thomson, M. W., Sigel, D. A., Walkemeyer, P. E., Trease, B. P., Magleby, S. P., and Howell, L. L., "Accommodating Thickness in Origami-Based Deployable Arrays," *ASME IDETC*, No. DETC2013-12348, 2013.

[11]Lee, N. and Close, S., "Curved pleat folding for smooth wrapping," *Proceedings of the Royal Society A*, Vol. 469, 2013.

[12]Edelstein, W. N., Madsen, S. N., Moussessian, A., and Chen, C., "Concepts and technologies for synthetic aperture radar from MEO and geosynchronous orbits," *Fourth International Asia-Pacific Environmental Remote Sensing Symposium 2004: Remote Sensing of the Atmosphere, Ocean, Environment, and Space*, International Society for Optics and Photonics, 2005, pp. 195–203.

[13]Moussessian, A., Del Castillo, L., Bach, V., Grando, M., Quijano, U., Smith, P., and Zawadzki, M., "Large Aperture, Scanning, L-Band SAR," *Earth Science*, 2011.

[14]Huang, J., Lou, M., Feria, A., and Kim, Y., "An inflatable L-band microstrip SAR array," *Antennas and Propagation Society International Symposium, 1998. IEEE*, Vol. 4, IEEE, 1998, pp. 2100–2103.

[15]Kobayashi, H., Kresling, B., and Vincent, J. F. V., "The geometry of unfolding tree leaves," *Proceedings of the Royal Society of London. Series B: Biological Sciences*, Vol. 265, No. 1391, 1998, pp. 147.

[16]Kobayashi, H. and Horikawa, K., "Deployable structures in plants," *Advances in Science and Technology*, Vol. 58, 2008, pp. 31–40.

[17]Satou, Y. and Furuya, H., "Fold Line Based on Mechanical Properties of Crease in Wrapping Fold Membrane," *54th AIAA/ASME/ASCE/AHS/ASC Structures, Structural Dynamics, and Materials Conference*, AIAA, Boston, MA, 8–1 April 2013.

[18]Instron, *2525-800 Series Load Cells*, 2005.

[19]Papa, A. and Pellegrino, S., "Systematically creased thin-film membrane structures," *Journal of Spacecraft and Rockets*, Vol. 45, No. 1, 2008, pp. 10–18.

[20]Miura, K., "Method of packaging and deployment of large membranes in space," *Proc. 31st Congress of the International Astronautical Federation*, Institute of Space and Astronautical Sciences, Tokyo, Japan, September, 1980 1985.

Packaging and Deployment Strategies for Synthetic Aperture Radar Membrane Antenna Arrays

Nicolas Lee[1] and Sergio Pellegrino[1]*

[1]Graduate Aerospace Laboratories, California Institute of Technology,
1200 E. California Blvd. MC 301-46, Pasadena, CA, USA, 91125. nnlee@caltech.edu, sergiop@caltech.edu

Abstract

The performance of spaceborne synthetic aperture radar (SAR) is limited by the size and therefore the areal density of the antenna array. Conventional arrays consist of radiating elements mounted on hinged panels that are relatively heavy. In order to produce larger arrays capable of operating at higher altitudes, or to support comparable SAR payloads on smaller spacecraft, a lighter structure such as one using membranes must be used. Membrane antenna arrays have been developed, but deployment remains a challenge. This paper describes possible techniques to package and deploy membrane structures that can support these antenna arrays.

1. Introduction

Space-borne synthetic aperture radar (SAR) has numerous applications including environment monitoring, planetary science, and navigation. Earth observation using SAR has the potential to enable earthquake forecasting and improved disaster response, but this requires larger area antenna arrays at higher altitudes than existing systems – on the order of 700 m^2 for a platform at geosynchronous Earth orbit (GEO) [1]. Current SAR payloads use antennas deployed on rigid, hinged panels. These systems are not scalable to GEO antenna requirements, because the overall system mass would exceed available launch capability. For example, RADARSAT-2's 1.5 x 15 m antenna had a mass of 784 kg [2], resulting in an areal density of almost 35 kg/m^2. Conservatively assuming a linear scaling, a 700 m^2 array would require over 24,000 kg for only the antenna, already several times greater than the existing launch capability of modern EELV rockets to GEO. In order to achieve the lower areal densities required for large antenna arrays, an alternative structure must be used. One possibility is to use a membrane structure to support the antenna array. Membrane structures are challenging to package and to deploy, but recent advances in solar sail and other membrane-based technologies have provided a new impetus for overcoming these difficulties. In Section 2, we describe an existing membrane antenna array design that serves as a reference configuration for the following discussion. Sections 3 and 4 discuss the challenges associated with membrane packaging and deployment, respectively. In Section 5, we discuss possible compromises between RF and structural performance in order to establish a trade space for design. Finally, we summarize and conclude in Section 6.

2. Background

One membrane antenna array design that has been tested on the ground is an L-band (1.26 GHz) patch array designed to be supported by two parallel membrane layers [3]. The membranes are composed of a polyimide substrate with laminated copper foil layers on each side. The patch elements are 8.89 cm (3.5") squares spaced every 15.24 cm (6") in a rectangular array on one membrane surface with all copper removed on the opposite surface. The ground plane is on a second parallel membrane held at a distance of 1.27 cm (0.5") from the patches. The feed network is on the opposite surface of the membrane to the ground plane, and radiatively coupled to the patches through slots. A prototype of this antenna configuration has been constructed with an array of 16 x 16 elements [4] using membrane-compatible transmit/receive (T/R) modules for electronic beam steering. However, it is supported by a rigid framework and has not been designed to be packaged or deployed. A smaller (3 m^2) version of this antenna design, using three membrane layers but no active electronics for steering, was deployed using inflatable booms [5].

3. Membrane Packaging

In order to fit a large array into a spacecraft for launch, it must be smaller than the rocket fairing and be able to survive the acoustic environment during launch. Membrane structures are inherently flexible, and can be folded or rolled. However, with electronics, care must be taken to avoid affecting the RF performance. In this section, we discuss possibilities for packaging a membrane antenna into a more compact geometry such that it can be deployed once it is spaceborne.

3.1 Membrane Folding and Creasing

We define a fold to be a local bending in the membrane with radius of curvature much less than the planar dimensions of the membrane. When a membrane is folded tightly (with small radius of curvature), plastic deformation can occur, which we refer to as a crease. This plastic deformation can include material yield, delamination between layers, and crack formation. If a crease is formed, the material around the fold will not unfold completely. This can lead to loss of electrical continuity or changes in impedance, which would degrade RF performance. Because of this, the ideal solution is to position crease lines such that they do not cross over sensitive RF geometry, such as the radiating elements. However, concerns still remain regarding the possiblity of damage to feedlines or a ground plane, as well as overall loss of geometric precision of the array.

One possible solution to avoid the detrimental effect of creases is to avoid folding entirely, e.g., by rolling the membrane instead. However, this only enables compaction of one dimension of the antenna array. If the array can be physically partitioned into strips, these can be independently rolled, and then deployed in parallel. Alternatively, folding a membrane can be done elastically, if the membrane curvature over the fold does not result in material strain beyond the yield point. Using a thinner membrane substrate allows for tighter folding without introducing plasticity. However, this is much more difficult with a metal layer because of its more ductile material properties. Another challenge is that two elastic folds in different directions will still cause plastic deformation at the point of intersection. This can be avoided by removing enough material around this point, leaving a hole that accomodates the presence of the two folds [6].

3.2 Folding Patterns

A basic folding pattern that can be used even for rigid hinged panels is the Miura-ori pattern [7], as shown in Figure 1. Compared to a double accordion fold, where all the creases are perpendicular, the Miura-ori shifts the crease vertices so that they do not stack on top of each other. This reduces the strain introduced in the folds and enables larger membranes to be folded. This pattern is particularly well suited for rectangular arrays of antenna elements, because of the regular spacing of the crease lines. However, the dimensions of the antenna elements constrain the slant angle ψ in the folding pattern. For the array described in Section 2, ψ must be greater than 54˚ to fit between a single row of patches, but approaches 90˚ for larger arrays containing more patches per folded panel. As the angle increases, the packaging efficiency of the Miura-ori pattern diminishes.

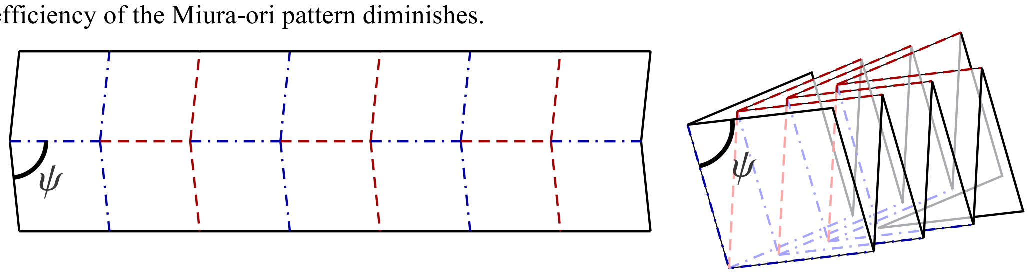

Figure 1. Unfolded (left) and folded (right) Miura-ori pattern, showing the slant angle ψ.

As mentioned in the previous section, an alternative is to roll the membrane, with the advantage of not forming any creases, but this only allows for one-dimensional deployment. A combination of these two approaches is to wrap a folded membrane around a spool. For membranes with significant thickness, this requires the fold pattern to be composed of curved, rather than straight lines [8]. A curved folding pattern, however, is more difficult to fit in between the radiating patches in a rectangular array, and cannot be folded elastically as described in the previous section.

Another family of folding patterns involves wrapping a membrane around a central hub. In contrast to Miura-ori-type patterns, wrapping patterns have major folds (where the membrane is folded close to 180˚) in a mostly radial direction, and less acute folds in other directions [9]. By wrapping around a polygonal rather than circular cylindrical hub, a folding pattern can be composed of straight line segments instead of curves. This allows for elastic folding as described above.

4. Membrane Deployment

Deploying membrane structures is challenging and prone to failure, as has been experienced on many previous space missions. Deployment dynamics are more complex than for structures composed of rigid elements, and the low areal density of membranes leaves them more susceptable to disturbance forces. The large size of many membrane structures also makes it difficult to test and characterize deployment on the ground in a suitable environment. In this section, we discuss the force profiles required to unfold a membrane, and the supporting structure that is required to deploy and maintain the membrane's geometry.

4.1 Unfolding

The force profiles of unfolding membranes are strongly dependent on the geometric constraints around the deployment system [10], as well as on the thickness of the membrane [11]. In particular, many folding patterns such as the Miura-ori pattern are designed to unfold as a single mechanism. However, the presence of a hub, housing, or other component of a deployment system can impose forces on some parts of the membrane, preventing it from unfolding all at once. These constraints can induce severe bending or even unintentional creasing in the membrane as it deploys. Even with a bare membrane, these effects can result in significantly higher deployment forces required and could result in jamming or stalled deployment, but in a membrane supporting RF elements in an active array, this is especially a concern because of the presence of rigid electrical components on the membrane, which might be pulled or scraped off as the the membrane unfolds. An example of a membrane deployment force profile (from a measurement in a laboratory setting) is shown in Figure 2, for a single-layered polyimide membrane. The membarne is 60 cm by 30 cm in area, and 50 μm thick. This profile highlights some of the dominant characteristics of deployment force profiles in general. First, the high frequency variation in the force profile, especially evident between 0.1 and 0.2 m deployed length, is indicative of friction as the membrane is deploying. Second, the larger periodic peaks in the profile between 0.2 and 0.5 m deployed length are a result of the geometric constraints forcing the membrane panels to unfold sequentially rather than simultaneously. Finally, the force profile increases drastically at the end of deployment, as the structure transitions from unfolding to membrane stretching.

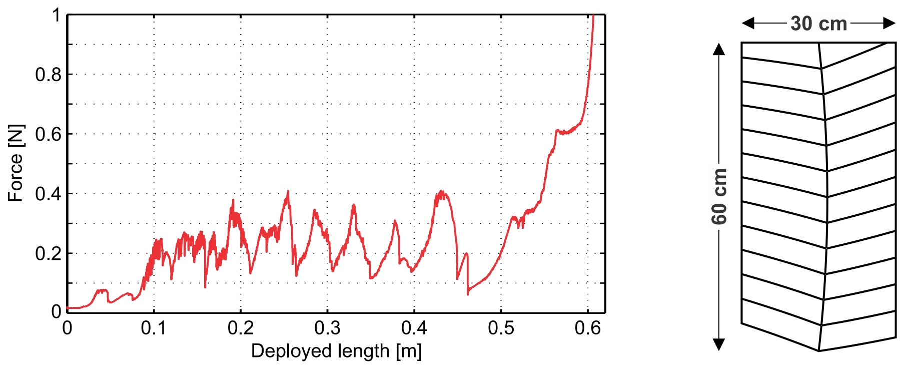

Figure 2. Deployment force profile (left) for a membrane wrapped around a spool and enclosed in a housing. The membrane (right) was folded using a curved crease pattern to wrap around a spool.

4.2 Structural Support

In order to provide the deployment force to unfold or otherwise unfurl a membrane, one or more stiff structural elements are often required. A typical geometry is to have a square array supported by four booms along the diagonals, extending from a central hub. These booms provide the force to pull the membrane out of its housing as well as to tension the deployed structure so that it remains flat. Because of the boom configuration, these membrane structures tend to be cut into quadrants, with a gap between quadrants where the boom is positioned. Centrifugal deployment without any booms is also possible and allows for a continuous membrane surface. However, given a deployment driven by an initial spin rate and no external torques, the centrifugal force is greatest at the start of deployment and lowest at the end. As a result, the required initial spin is determined by the force necessary to achieve and maintain adequate flatness at the end of deployment, and will provide more force than necessary at during the earlier stages of unfolding. This excess force could potentially damage the membrane as it deploys. Additionally, a centrifugally deployed membrane will require continued spin throughout its lifetime to provide the tension that maintains the array's geometry.

5. RF and Structural Performance Tradeoff

In the previous two sections, we discussed factors that must be considered when designing a membrane antenna array. Creasing and fold locations may affect the antenna positions as well as the geometry of the array feed network, in order to minimize folds over the transmission lines. For some fold patterns, it will not be possible to maintain a regular antenna spacing as well as avoid folding or creasing over the radiating elements. However, it may be possible to simultaneously optimize fold geometry and antenna locations in order to minimize the amplitude of grating or side lobes. A nonuniform antenna spacing could very well improve the array performance by reducing the largest lobes [12]. The structure supporting a membrane array could also influence the RF design by partitioning the membrane into discrete segments. This would affect the topology of the RF feed network, and might require a more complex design than the parallel corporate feed used in the existing membrane antenna prototype. Finally, the overall geometry of a membrane structure will not be as precise as an equivalent panel structure. This could lead to the choice of a lower operating frequency than would otherwise be desired.

6. Conclusion

In order for large SAR missions to be realized in GEO, membrane-supported antenna arrays must replace traditional rigid hinged panel structures. However, the challenges associated with both packaging and deployment of these membrane arrays are significant. A radar system using a membrane antenna array must account for these challenges and allow for flexibility (literally and figuratively) in the RF design in order to best leverage the mass savings that come with a membrane structure.

7. Acknowledgments

N. Lee was supported by a postdoctoral fellowship from the W. M. Keck Institute for Space Studies.

8. References

1. W. N. Edelstein, S. N. Madsen, A. Moussessian, and C. Chen, “Concepts and technologies for synthetic aperture radar from MEO and geosynchronous orbits,” International Asia-Pacific Environmental Remote Sensing Symposium, 2005, pp. 195–203.
2. C. E. Livingstone, I. Sikaneta, C. Gierull, S. Chiu, and P. Beaulne, “RADARSAT-2 System and Mode Description. In Integration of Space-Based Assets within Full Spectrum Operations,” Meeting Proceedings RTO-MP-SCI-150, Neuilly-sur-Seine, France, 2005, pp. 15-1–15-22.
3. J. Huang and A. Moussessian, “Thin-membrane aperture-coupled L-band patch antenna,” Antennas and Propagation Society International Symposium, 2004, pp. 2388–2391.
4. A. Moussessian, L. Del Castillo, V. Bach, M. Grando, U. Quijano, P. Smith, and M. Zawadzki, “Large aperture, scanning, L-band SAR,” *Earth Science*, 2011.
5. A. Moussessian, L. Del Castillo, J. Huang, G. Sadowy, J. Hoffman, P. Smith, T. Hatake, C. Derksen, B. Lopez, and E. Caro, “An active membrane phased array radar,” Microwave Symposium Digest, 2005, pp. 1711-1714.
6. W. D. Reynolds and T. W. Murphey, “Elastic spiral folding for flat membrane apertures,” AIAA Spacecraft Structures Conference, 2014.
7. K. Miura, “Method of packaging and deployment of large membranes in space,” Proc. 31st Congress of the International Astronautical Federation, Tokyo, Japan, 1980.
8. N. Lee and S. Close, “Curved pleat folding for smooth wrapping,” *Proceedings of the Royal Society A*, **469**, 2013.
9. S. D. Guest and S. Pellegrino, “Inextensional wrapping of flat membranes,” Proceedings of the First International Seminar on Structural Morphology, Montpelier, 1992, pp. 203–215.
10. N. Lee and S. Pellegrino, “Multi-layered membrane structures with curved creases for smooth packaging and deployment,” AIAA Spacecraft Structures Conference, 2014.
11. M. Arya and S. Pellegrino, “Deployment mechanics of highly compacted thin membrane structures,” AIAA Spacecraft Structures Conference, 2014.
12. R. F. Harrington, “Sidelobe reduction by nonuniform element spacing,” IRE Transactions on Antennas and Propagation, **9**, March 1961, pp. 187–192.

Wrapping Thick Membranes with Slipping Folds

Manan Arya[*], Nicolas Lee[†], and Sergio Pellegrino[‡]
California Institute of Technology, Pasadena, CA 91125

A novel method of packaging finite-thickness membranes tightly and with high packaging efficiency is presented. This method allows the membrane to be packaged without extension and without plastic creasing. As such, initially flat membranes can be deployed to a flat state. Membrane thickness is accommodated by removing material along fold lines and exploiting the slipping deformation mechanism thus created.

Also presented are methods for prestressing and deploying membranes packaged according to this technique. Initial tests demonstrate packaging efficiencies of 73% without plastic deformation. Experimental deployment tests of a meter-scale model showed controlled deployment with unfolding forces of less than 0.6 N.

Nomenclature

A	Area
a	Diagonal length along x-axis
$\bar{a}$	Partially deployed length along x-axis
b	Diagonal length along y-axis
$\bar{b}$	Partially deployed length along y-axis
E	Young's modulus
F	Tensioning or deployment force
f	Pitch of involute curve
$f(x)$	Edge profile
H_p	Packaged height
h	Thickness
i	Strip index
L	Side length
n	Number of strips
$\mathbf{n}(s)$	Normal to base curve
P	Prestress per unit length
$\mathbf{p}$(s)	Generator curve
$q(i)$	Strip offset from base curve
R	Radius of generator curve
R_{min}	Elastic radius of curvature
R_p	Packaged radius
$\mathbf{r}(s)$	Base curve
s	Arclength of the base curve
$\alpha(s)$	Involute angle
γ	Packaged radius normalized by h
η	Packaging efficiency
θ	Involute clock angle
$\kappa(s)$	Signed curvature
λ	Length normalized by h
ξ	Slip along fold line
ρ	Fold angle
σ_y	Yield stress
ϕ	Thickness multiplier
ψ	R_{min} normalized by h

I. Introduction

Membranes are widely used for space applications requiring large area surfaces with low areal density. Solar arrays, solar sails, drag sails, reflectors, transmissive optics, and thermal shields are all examples of

[*]Graduate Student, Graduate Aerospace Laboratories. MC 205-45. AIAA Student Member.
[†]W. M. Keck Institute for Space Studies Postdoctoral Scholar in Aerospace. MC 301-46. AIAA Member.
[‡]Joyce and Kent Kresa Professor of Aeronautics and Professor of Civil Engineering, Graduate Aerospace Laboratories. MC 301-46. AIAA Fellow.

large-area structures that may be constructed using membranes. Many applications require these structures to be tightly packaged for launch and deployed to their operational state after launch into space, which raises several fundamental challenges.

Prime among them are efficient packaging, i.e. packaging with only minimal volume gaps in the folded package, packaging without exceeding the yield stress of the membrane, and ability to deploy the membrane to a flat state with minimal edge forces. This paper presents a packaging scheme that addresses all of these challenges in a novel way.

The current practice in membrane packaging is to use localized bending deformation, known as *creasing*, as the basic mechanism for compaction. An alternative approach is proposed, based on the removal of material along the fold lines. This approach provides additional deformation mechanisms and hence enables a new class of packaging solutions.

This paper is organized thus. Section II presents a brief survey of the state of the art on the packaging of membrane structures. A new concept for packaging, deploying, and prestressing is presented in Section III, Section IV, and Section V. Finally, Section VI describes the packaging and deployment tests that were conducted to demonstrate and verify the proposed concept, and Section VII presents and discusses their results.

II. Background

This section reviews existing membrane packaging solutions. These can be divided into two categories: those that compact the membrane along one dimension, and those that compact the membrane along two dimensions.

II.A. 1D Compaction

Three well-known techniques are used for packaging large-area space structures along one dimension: z-folding, wrapping (or rolling), and fan-folding. These techniques provide efficient packaging and easily accommodate for membrane thickness; plastic deformation can be avoided by choosing a suitably large radius of wrapping or folding. However, compaction occurs in one dimension only, and hence these techniques are not applicable when both dimensions of the deployed structure exceed the available packaging envelope.

II.B. 2D Compaction

Miura-ori[1] is a well-known scheme for biaxially packaging a membrane. It modifies the standard map folding technique (i.e. double z-folding) by skewing one set of parallel fold lines. Both map folding and Miura-ori have been used for packaging space structures;[2,3] however, neither map folding nor Miura-ori accommodate for membrane thickness.

It is also possible to compact membranes along two dimensions by first folding and then wrapping. Both z-folding and wrapping,[4] and star folding and wrapping[5] have been used to package membrane space structures. Folding and wrapping requires curved creases to accommodate the thickness of the membrane;[6,7] however, curved creases do not preserve the flatness of the membrane. In fact, it is impossible for any membrane that has been creased plastically to be pulled completely flat.[8,9]

Techniques for wrapping a membrane around a polygonal hub using straight creases have been proposed.[11,12] These techniques generate crease patterns by modeling the wrapped membrane as a collection of straight line creases intersecting at vertices. By placing the vertices set distances apart in the folded state, the crease lengths and angles can be computed. Although these patterns provide, on average, the required accommodation for the thickness of the membrane, the solution is not exactly correct near the fold lines or at the vertices.

It is possible to make these solutions exact by trimming away material. As seen in Figure 1a,[10] an ideal zero-thickness fold pattern, denoted by the red line, can be applied to a finite thickness membrane, denoted by the black outline, by trimming away material close to the fold lines and vertices. However, as the final fold angle decreases, more and more material must be trimmed away; in the limit as the final fold angle goes to zero, all material must be removed. In practice, because it is impossible to decrease the thickness of the membrane to zero, the packaging efficiencies achievable are limited. This technique also requires panels of non-uniform thickness, which may be troublesome for engineering applications.

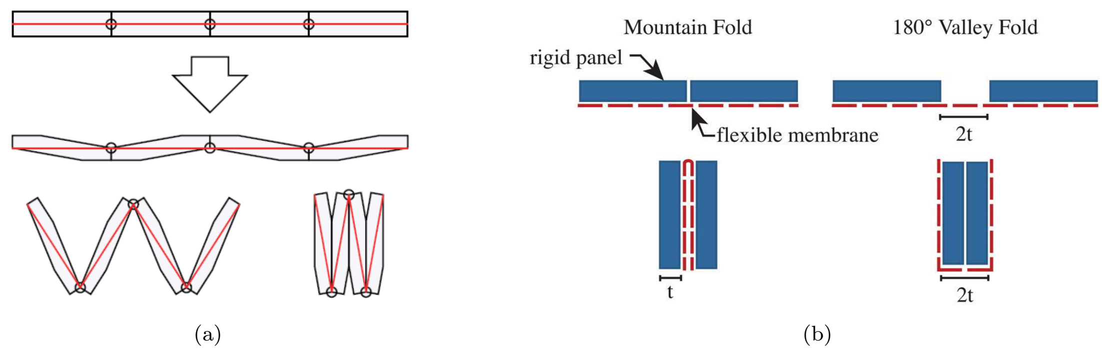

Figure 1: (a) Thickness reduction near the fold lines allows packaging using the ideal zero-thickness crease pattern denoted by the red line.[10] (b) An alternative method is to widen the creases; the width of the crease depends on the final folded angle.[12]

Instead of removing material, it has been proposed to widen and reduce the thickness of the crease regions.[12,13] However, this results in the presence of large voids in the packaged membrane. Crease widths of 10 to 14 times the panel thickness were required in previous studies to enable packaging.[12]

Hoberman's modifications[14] of Miura-ori allow for the folding of thick membranes. However, these modified patterns also result in gaps between membrane faces in the folded state, and the size of these gaps grows with the size of the membrane, leading to loss of packaging efficiency.

Trautz and Künstler[15] propose a degree-4 vertex in a thick membrane enabled by sliding hinges along the crease lines. Their scheme requires the creases to slide by an infinite amount as the crease angle tends to zero. For this reason, their method does not result in tight and efficient packaging.

In concluding this brief review, it should be noted that there have been several proposals for packaging techniques for thin shell structures that use either radial or spiral cuts.[16,17,18] Cuts introduce additional deformation mechanisms that enable efficient packaging schemes that accommodate thickness, which is a theme central to the present paper.

III. Packaging Concept

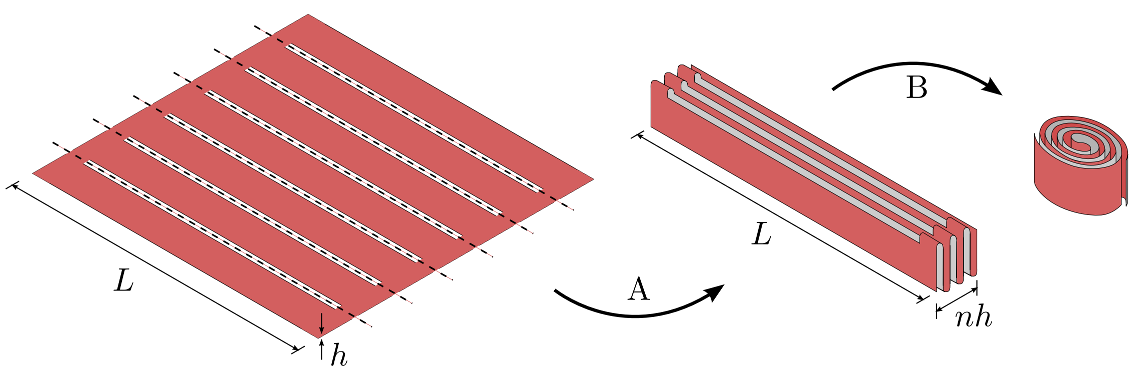

Figure 2: Packaging concept consisting of two steps: (A) z-folding and (B) symmetric wrapping. First, the square membrane is z-folded using $n-1$ slipping folds. Then, the resulting stack of n strips is wrapped in a rotationally symmetric fashion. For clarity, only a single strip is shown in the wrapped configuration.

To illustrate the basic concept, consider the problem of packaging a square membrane of side length L and thickness h as shown in Figure 2. The membrane is divided into n strips by $n-1$ slipping folds. A *slipping fold* allows for rotation about the fold line as well as slip along the fold line. In Figure 2 the slipping folds are realized by cutting a series of parallel slits in the membrane, but the continuity of the membrane is maintained at either end of each fold line.

The packaging concept has two compaction steps, each compacting the membrane along a single dimension. For the first step, the membrane is z-folded using parallel slipping folds, which produces a stack of n

strips. For the second step, this stack of strips is wrapped in a rotationally symmetric fashion.

The slipping folds are needed to accommodate the incompatibility created by wrapping the thick membrane strips around different radii. The symmetric wrapping scheme ensures that the ends of the strips can remain connected. The following two subsections will explain in detail the two enabling concepts of slipping folds and symmetric wrapping.

III.A. Slipping Folds

The proposed packaging concept relies on material removal along fold lines to create *slipping folds*. The membrane can be folded and unfolded at such slipping folds without straining the material. In some sense, a slipping fold is an extreme case of a score; whereas a score weakens the membrane to localize bending strains, a slipping fold removes material entirely.

The two degrees of freedom of a slipping fold are shown in Figure 3. In addition to the fold angle, ρ, slipping folds have a slip degree of freedom, ξ, which is the linear displacement of the material on one side of the fold with respect to the material on the other side, in the direction of the fold line. An ideal slipping fold has zero stiffness associated with both these degrees of freedom.

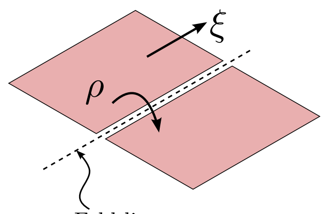

Figure 3: Slipping folds have two degrees of freedom: fold angle ρ and slip ξ.

Because material removal along the fold lines leads to a reduction in the continuity and hence in the stiffness of a structure, several realizations of slipping folds have been considered that are not simple cuts. These realizations include connections that allow for the transmission of tension forces and the limited transmission of shearing forces across fold lines. Figure 4 illustrates two possible methods for forming these connections.

Hinged fold A cylindrical rod is located at the fold line. This rod is attached to the material on one side of the fold using tabs. The material on the other side is attached to the rod using a loop. This loop can rotate about the rod and slip along the rod. Maximum slip is reached when the loop contacts a tab. A hinged fold transmits tension across the fold line. In the maximum slip state, a shearing force may also be transmitted.

Ligament fold To create a ligament fold, one or more thin strips of material are left uncut at the fold line. The length of the ligament is chosen to allow for the required deformation along the fold line. Like the hinged fold, a ligament fold has state of maximum slip beyond which the ligament will deform plastically. A ligament fold allows for the transmission of tension and shear across the fold line.

The slip degree of freedom is crucial; it enables the second compaction step of wrapping. Wrapping the z-folded stack of n strips leads to the outer strips going around larger radii than the inner strips because each strip has thickness $h > 0$. Thus, for the same arclength, outer strips traverse smaller wrapping angles than inner layers. If the strips cannot slip against each other, wrapping the stack of strips will result in straining of the membrane.

In addition to areas where the membrane strips can slip against each other, it is also advantageous to constrain the slip to be zero at certain locations, which allows the strips to be connected at the ends. This condition can be achieved by using a rotationally symmetric wrapping.

III.B. Symmetric Wrapping

Symmetric wrappings are a class of wrappings that result in a configuration that has two-fold symmetry. Using these wrappings, it is possible to enforce zero slip, for example, at the two ends of the z-folded stack, which enables the edges of the membrane to remain uncut and able to transmit tension. The ability of

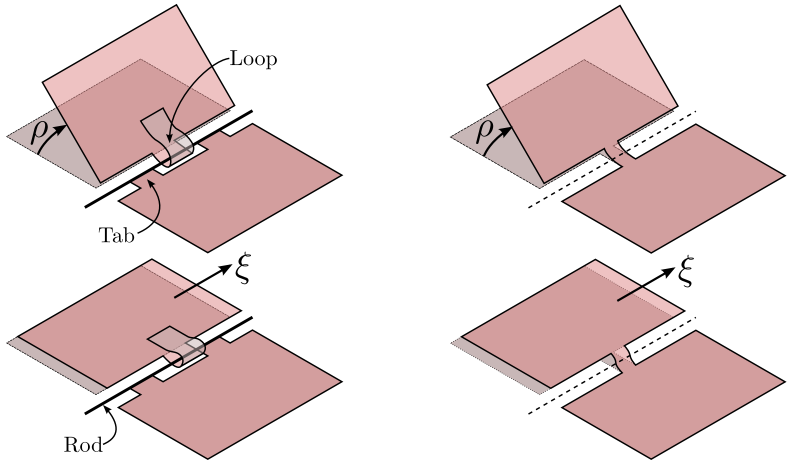

(a) Hinged fold. (b) Ligament fold.

Figure 4: Two examples of slipping folds with connections across the fold lines that still allow for the rotation and slip degrees of freedom.

the edges to transmit tension will be useful when a concept for prestressing the membrane are discussed in Section IV.

The membrane strips in the wrapped stack are modeled as a set of curves offset from a *base curve*. (If the number of strips n is odd, the base curve corresponds to the middle strip.)

The base curve $\mathbf{r}(s) : [-L/2, L/2] \to \mathbb{R}^2$ is parametrized by its arclength s. As shown in Figure 5, the i^{th} strip is offset from the base curve by $q(i)\mathbf{n}(s)$, where $\mathbf{n}(s)$ is the normal to the base curve and $q(i)$ is a separation distance. (If n is odd, $q(i) = ih$.) Thus the i^{th} strip follows the offset curve $\mathbf{r}(i; s) = \mathbf{r}(s) + q(i)\mathbf{n}(s)$.

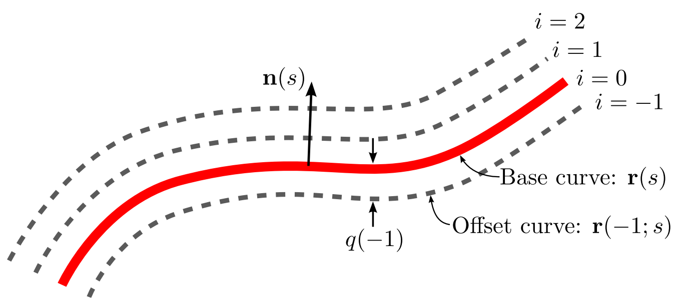

Figure 5: Offset curves separated by a normal distance $q(i)$.

For the ends of the strips to be connected, the length of the i^{th} strip L_i must equal the length of the base curve L for all i. This is possible when the integral of the signed curvature $\kappa(s)$ of the base curve is zero. To see this, consider the formula for the length L_i of the i^{th} strip:

$$L_i = \int_{-L/2}^{L/2} \|\mathbf{r}'(i; s)\| \, \mathrm{d}s \tag{1}$$

$$\|\mathbf{r}'(i; s)\| = \|\mathbf{r}'(s) + q(i)\mathbf{n}'(s)\| \tag{2}$$

Now the derivative of the normal vector $\mathbf{n}'(s)$ is parallel to the tangent vector $\mathbf{r}'(s)$ and has length $|\kappa(s)|$:[19]

$$\mathbf{n}'(s) = -\kappa(s)\mathbf{r}'(s) \tag{3}$$

Substituting this into the expression for $\|\mathbf{r}'(i; s)\|$ and noting that $\|\mathbf{r}'(s)\| = 1$ gives

$$\|\mathbf{r}'(i; s)\| = 1 - q(i)\kappa(s) \tag{4}$$

$$\Rightarrow L_i = \int_{-L/2}^{L/2} [1 - q(i)\kappa(s)] \, \mathrm{d}s = L - q(i) \int_{-L/2}^{L/2} \kappa(s) \, \mathrm{d}s \tag{5}$$

Thus, for $L_i = L \, \forall \, i$ the following condition must be satisfied:

$$\int_{-L/2}^{L/2} \kappa(s) \, \mathrm{d}s = 0 \tag{6}$$

A simple way to meet this condition is to have $\kappa(s)$ be an odd function of arclength, i.e. $-\kappa(-s) = \kappa(s)$. A base curve that has this may be defined in a piecewise manner, using a *generator curve* $\mathbf{p}(s) : [0, L/2] \to \mathbb{R}^2$ and a copy of the generator curve rotated by 180°:

$$\mathbf{r}(s) = \begin{cases} -\mathbf{p}(-s) & \text{if } s \in [-L/2, 0) \\ \mathbf{p}(s) & \text{if } s \in [0, L/2] \end{cases} \tag{7}$$

For $\mathbf{r}(s) \in C^2$, $\mathbf{p}(s) \in C^2$, $\mathbf{p}(0) = \mathbf{0}$ and $\mathbf{p}''(0) = \mathbf{0}$ are needed.

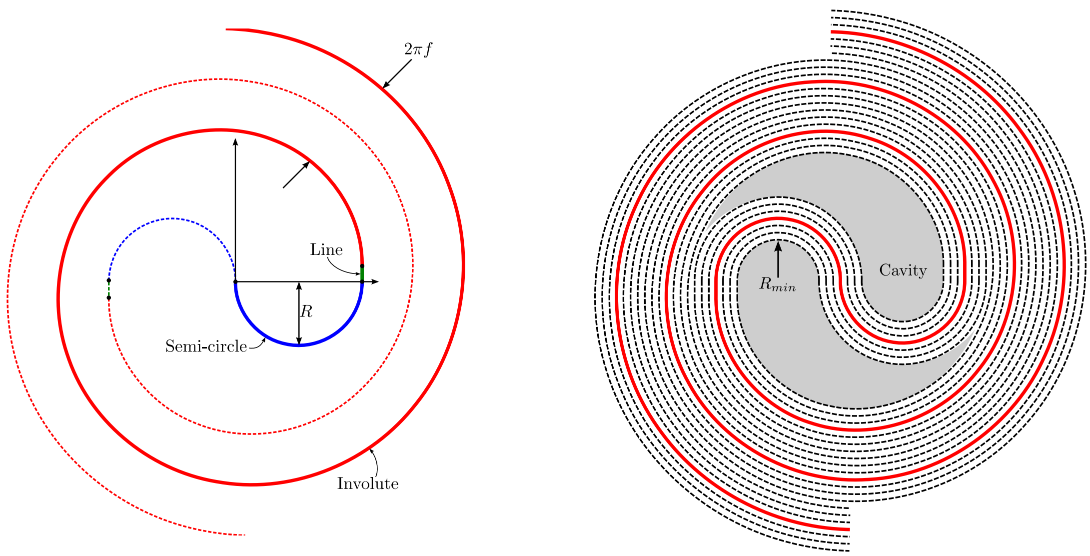

(a) Generator curve (b) Offset curves

Figure 6: Wrapping curve for efficient packaging. The shaded areas in (b) are the only cavities that result from this curve, and their size depends mainly on the minimum radius of curvature R_{min}.

A generator curve that allows for compact wrapping is shown in Figure 6. It is a piecewise curve consisting of a semi-circle of radius R, a vertical line of length f, and an involute of a circle with pitch $2\pi f$:

$$\mathbf{p}(s) = \begin{cases} R\,\{1 - \cos{(s/R)}, -\sin{(s/R)}\} & \text{if } s \in [0, \pi R] \\ R\,\{2, (s/R) - \pi\} & \text{if } s \in (\pi R, \pi R + f) \\ \begin{array}{l} f\,\{\cos{(\alpha - \theta)} + \alpha \sin{(\alpha - \theta)}, \\ \quad \sin{(\alpha - \theta)} - \alpha \cos{(\alpha - \theta)}\} \end{array} & \text{if } s \in (\pi R + f, L/2) \end{cases} \tag{8}$$

$$\alpha^2 = \frac{2}{f}\,(s - \pi R - f) + \left(\frac{2R}{f}\right)^2 \tag{9}$$

$$\theta = \frac{2R}{f} - \frac{\pi}{2} \tag{10}$$

Note that this particular generator curve has discontinuous curvature at all points where two pieces meet. Therefore it is not expected that a wrapped membrane will follow this curve exactly; however, it is a simple curve that may be used to estimate the size of the packaged membrane, which will be contained within a cylinder of radius R_p and height H_p.

A strip thickness multiplier $\phi \geq 1$ is included to account for the fact that in the packaged configuration the strips may be separated by some distance $\phi h \geq h$. The pitch of the involute $2\pi f = 2n\phi h$ accounts for the thickness of the z-folded stack of strips. The radius of the semi-circle $R = R_{min} + \phi hn/2$ is such that the curvature limit $1/R_{min}$, dictated by the material modulus E and yield stress σ_y, is not exceeded:

$$\frac{1}{R_{min}} = \frac{2\sigma_y}{Eh} \tag{11}$$

III.C. Packaging Efficiency

The packaged radius is $R_p = \max \|\mathbf{r}(i;s)\|$ and the packaged height is $H_p = L/n$. Using these, the packaging efficiency η, which is the ratio of the packaged volume to the material volume of the membrane, can be estimated.

$$\eta = \frac{L^2 h}{\pi R_p^2 H_p} \tag{12}$$

The packaging efficiency is a function for four non-dimensional parameters: n, $\psi \equiv R_{min}/h$, $\lambda \equiv L/h$, and ϕ. It has the following expression:

$$\eta = \frac{n\lambda}{\pi\gamma^2} \tag{13}$$

$$\gamma^2 \equiv \left(\frac{R_p}{h}\right)^2 = \phi^2\left[\left(\frac{n}{\pi}\right)^2 + \left(\frac{n\alpha_{max}}{\pi}\right)^2 + \left(\frac{n-1}{2}\right)^2 + \frac{n(n-1)}{\pi}\alpha_{max}\right] \tag{14}$$

$$\alpha_{max}^2 = \frac{\pi\lambda}{n\phi} + \frac{2\pi^2\psi}{n\phi} - 2 + \left(\frac{2\pi\psi}{n\phi}\right)^2 \tag{15}$$

Figure 7 shows the variation of the packaging efficiency with λ, ψ, and ϕ. The effect of n on the packaging efficiency is minimal, since as n increases, the packaged height decreases, but the packaged radius increases, and thus the packaged volume varies minimally.

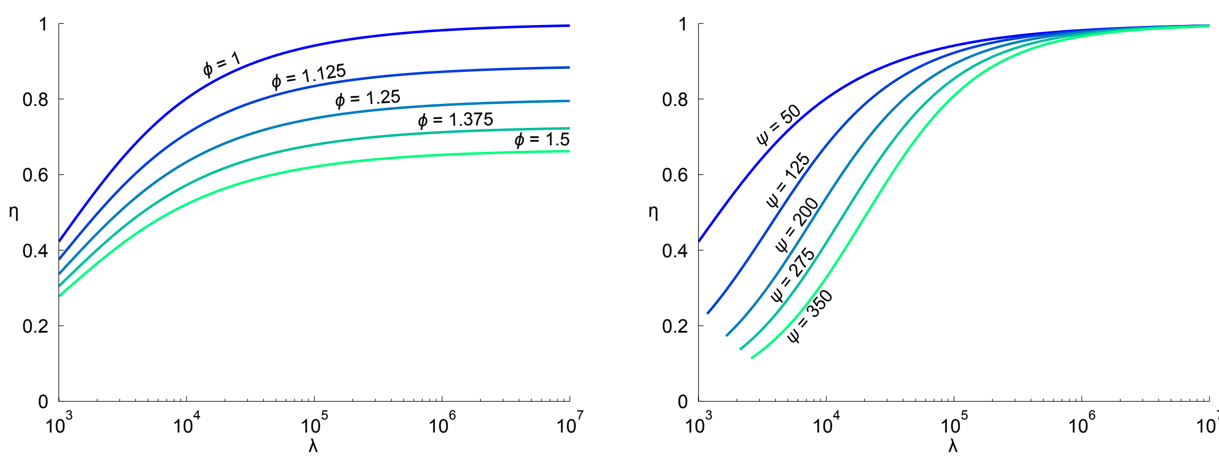

(a) $n = 100, \psi = 50$

(b) $n = 100, \phi = 1$

Figure 7: Packaging efficiency η as a function of the dimensionless deployed length $\lambda = L/h$, the dimensionless minimum bend radius $\psi = R_{min}/h$, and the strip thickness multiplier ϕ. For (a), n and ψ are held constant, and for (b), n and ϕ are held constant.

Figure 7a shows that the strip thickness multiplier ϕ has the greatest effect on the packaging efficiency for large λ. In fact, in the limit of $\lambda \to \infty$, $\eta \to 1/\phi$. This means that for very large or very thin membranes, the global packaging efficiency depends only on the local, per-strip packaging efficiency. Figure 7b shows that the minimum bend radius of the material $R_{min} = h\psi$ has the greatest effect for small λ. As λ increases, the size of the two cavities (which is determined by R_{min}) shown in Figure 6 shrinks in relation to the membrane volume and the effect of ψ decreases.

IV. Prestressing Concept

A membrane with slipping folds is anisotropic; the stiffness parallel to the slipping folds is much higher than the stiffness perpendicular to them. This anisotropy must be taken into account when prestressing the membrane. This section presents one particular solution to the problem of prestressing membranes of this type.

Consider a membrane as shown in Figure 8a with slipping folds parallel to the y-axis, length a along the x-axis and length b along the y-axis. When prestressed, it is desired that each strip has equal tension in the y-direction, i.e. parallel to the slipping folds, and no tension in the x-direction, i.e. perpendicular to the slipping folds.

Consider applying global tensioning forces F_x at $[\pm a/2, 0]$ and F_y at $[0, \pm b/2]$ (using suitable external compression members e.g. booms or masts); the membrane edges can be shaped such as to distribute these tensioning forces to uniaxial tensile loading P, which is a force per unit length. Since the symmetric wrapping ensures that the edges of the membrane remain continuous and uncut, they can transmit tension. It is easy to show that for P uniform, the edge profile $f(x) : [0, a/2] \to \mathbb{R}$ must be parabolic:

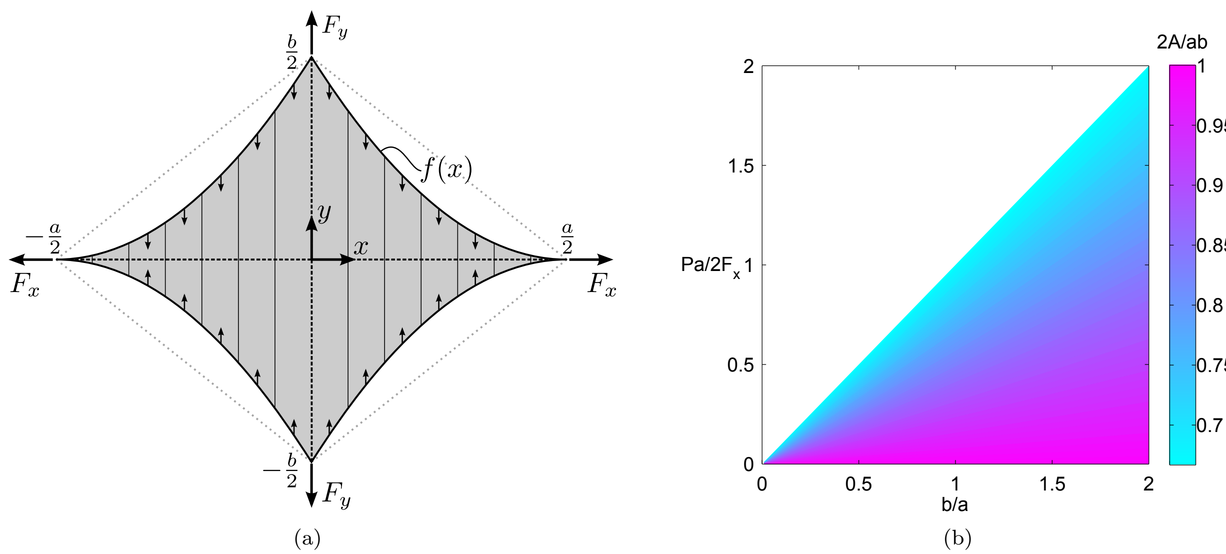

Figure 8: (a) Membrane with parabolic edges tensioned uniformly and uniaxially by four radial forces. (b) Membrane area A normalized by the rhombus area $ab/2$ as function of the aspect ratio b/a and the normalized loading $Pa/2F_x$. The white triangle is inaccessible due to $f'(a/2) \leq 0$.

$$f(x) = \left(\frac{P}{F_x}\right) x^2 - \left(\frac{Pa}{2F_x} + \frac{b}{a}\right) x + \frac{b}{2} \tag{16}$$

The edges of the membrane can be constructed by taking $f(x)$ and mirroring it about the x and y axes. To ensure $f(x) \geq 0$, it is insisted that $f'(a/2) \leq 0$, and hence

$$\frac{Pa}{2F_x} - \frac{b}{a} \leq 0 \tag{17}$$

Two non-dimensional parameters, the loading parameter $Pa/2F_x$ and the aspect ratio b/a, determine key aspects of this structure. The membrane area A normalized by the rhombus area $ab/2$ is a function of these parameters, as is the ratio of the global tensioning forces F_y/F_x:

$$\frac{2A}{ab} = 1 - \frac{1}{3}\frac{a}{b}\frac{Pa}{2F_x} \tag{18}$$

$$\frac{F_y}{F_x} = \frac{Pa}{2F_x} + \frac{b}{a} \tag{19}$$

Figure 8b plots the dimensionless area as a function of these two parameters.

V. Deployment Concept

This section discusses a particular concept for deploying a slip-wrapped membrane with parabolic edges. The deployment concept, shown in Figure 9, consists of an unwrapping stage followed by an unfolding stage.

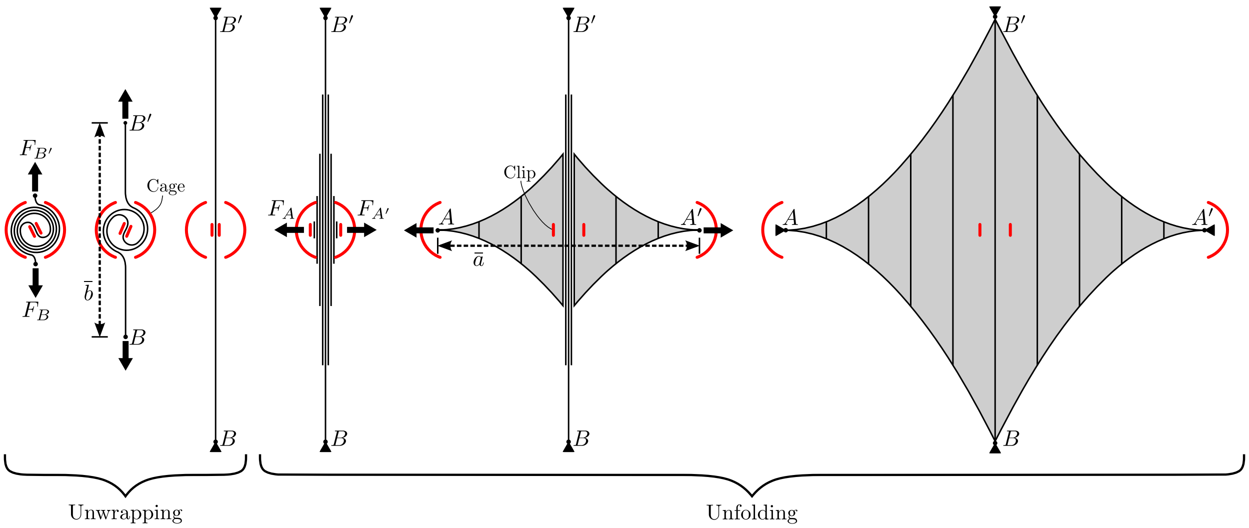

Figure 9: The two stages of deploying a slip-wrapped membrane with parabolic edges. For clarity, just one strip is shown during the unwrapping stage.

In the unwrapping stage, the two ends B and B' of the wrapped stack are pulled in opposite directions by applying forces F_B and $F_{B'}$. The separation $\bar{b}$ between B and B' increases until $\bar{b} = b$.

In the unfolding stage, the stack of strips is unfolded by applying forces F_A and F'_A at points A and A'. The separation between these points $\bar{a}$ grows to a at the end of deployment.

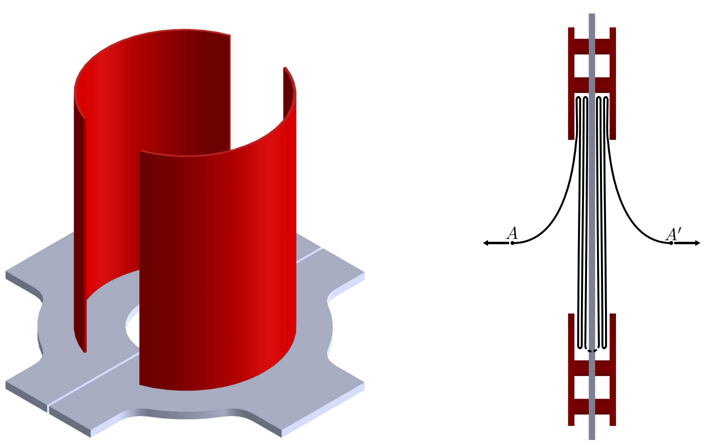

(a) Cage (isometric view)

(b) Clip (section view)

Figure 10: Deployment restraints.

A "cage", shown in Figure 10a, is used to manage the unwrapping process. It is a cylindrical tube with two slots. The endpoints B and B' of the folded membrane stack are pulled out through these slots. During the unfolding stage, the two halves of the cage must separate and move apart, see Figure 9.

A "clip", shown in Figure 10b, holds the folded stack of the strips together at its midpoint. It manages the unfolding stage; it ensures that when the endpoints A and A' of the folded stack are pulled outwards, the strips deploy one at a time. The wrapped membrane rotates with respect to the cage during the unwrapping stage, and hence the clip has to rotate as well.

An experimental implementation of this concept is presented in the following section.

VI. Test Apparatus and Procedures

VI.A. Packaging Tests

To wrap a membrane according to the technique described in Section III, a "wrapping plug" can be used to guide the folded membrane stack along the designed curve and prevent the membrane from exceeding the maximum curvature limit as provided by Equation (11). Figure 11a shows a conceptual plug; it consists of two halves shaped like the cavities in the wrapping curve of Figure 6.

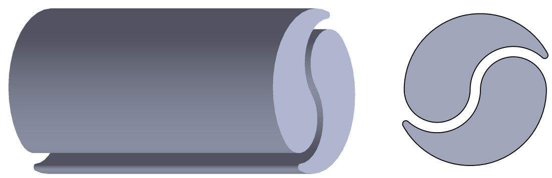

(a) Conceptual design

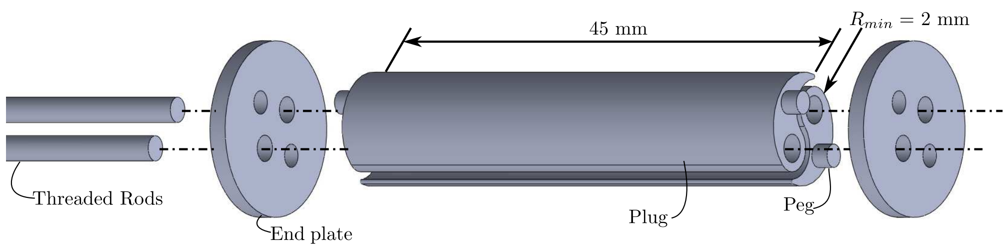

(b) Design details

Figure 11: Wrapping plug.

A wrapping plug suitable for polyester films of thickness of up to 50.8 µm was designed. Assuming $E = 3.50$ GPa and $\sigma_y = 100$ MPa for polyester films, Equation (11) gives R_{min} of 0.89 mm. However, fabrication constraints imposed an upper bound on R_{min} of 2 mm, and therefore there was a margin of safety of 2.25 against plastic deformation in the membrane. A detailed design of the wrapping plug with $R_{min} = 2$ mm and a length of 45 mm is shown in Figure 11b.

The two halves of the plug were fabricated from UV-curable acrylic plastic using stereolithography. Each half of the plug has a lengthwise hole to accept a threaded rod. Each half also has small pegs at either end that mate with two end plates. These end plates hold the two halves of the plug in alignment. Two threaded rods are passed through the lengthwise holes in the plugs and the end plates, and are held in place by nuts.

Two square models were made from aluminized polyester film and wrapped around this plug. Table 1 lists the relevant parameters of these models. These models had ligament slipping folds made using a computer-controlled laser cutter (Universal Laser Systems® ILS9.75). There were 7 ligaments per fold line. The ligaments had widths of 1.5 mm, lengths of 8 mm, and rounded corners.

Model	h (µm)	L(m)	$\log_{10}(\lambda)$	n	ψ
1	25.4	0.5	4.3	13	78.7
2	50.8	0.5	4.0	13	39.4

Table 1: Packaging models

To package the membrane, it was first folded into a stack of strips. The strips were then pre-slipped with respect to each other at the middle of the stack by 1.1 mm and 1.7 mm respectively for models 1 and 2. This pre-slip was induced before the membrane stack was inserted into the plug. When packaging without a plug, this step of pre-slipping is not required, since the strips are free to slip during packaging. However, the plug tightly clamps the strips against each other and prevents slip from developing during packaging. Therefore, it was necessary to pre-slip the strips.

The strips were then manually wrapped tightly against the plug. A loop of string was used to hold the membrane wrapped while a digital caliper was used to measure the packaged diameter at the middle of the wrap. Figure 12 shows model 2 wrapped around the plug.

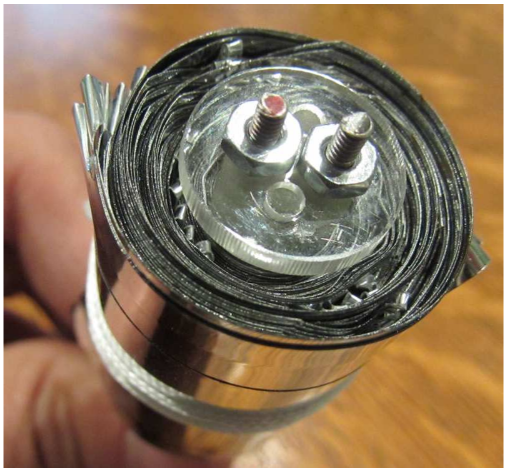

Figure 12: Model 2 wrapped around the plug. The packaged diameter was 23.92 mm.

VI.B. Prestressing Test

To demonstrate the feasibility of the prestressing concept, an aluminized polyester film model with $b/a = Pa/2F_x = 1$, $a = 0.8\,\mathrm{m}$, $h = 50.8\,\mu\mathrm{m}$ was made. The parabolic edge and the ligament slipping folds were made using the laser cutter. Since $b/a = Pa/2F_x = 1$, $F_y/F_x = 2$.

Figure 13 shows the model hanging on a metal-backed chalkboard using magnets. The tensioning forces were applied by hanging weights: F_y was applied by hanging a 50 g weight and pinning the top corner of the membrane and F_x was applied through a pulley by hanging a 25 g weight and pinning the right corner of the membrane.

Inspection of the model showed that each strip was in a state of tension, and that the model was able to hang flat, though there was some residual transverse curvature of the strips from the film having been stored on a roll.

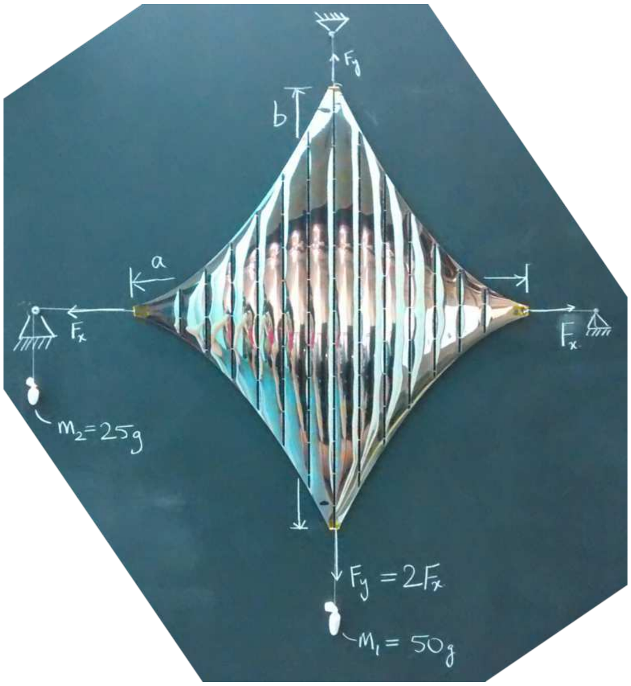

Figure 13: Hanging model test of prestressing concept.

VI.C. Deployment Test

To test the deployment concept presented in Section V, a membrane model with parabolic edges and ligament slipping folds was fabricated. The model had $b/a = Pa/2F_x = 1$, $a = 1\,\mathrm{m}$, $h = 25.4\,\mu\mathrm{m}$, and was made from aluminized polyester film. Because the laser cutter allowed a maximum part size of $0.91\,\mathrm{m} \times 0.61\,\mathrm{m}$, the model was fabricated in three separate pieces, which were joined together using polyimide tape.

The deployment rig shown in Figure 14 was used to test the deployment concept. It consisted of four independent linear actuators to provide the deployment forces $F_B, F_{B'}, F_A, F_{A'}$, four force sensors to record the deployment forces, and a suspension system to partially offload the mass of the membrane.

Each linear actuator consisted of a lead screw coupled to a stepper motor that drives a carriage back and forth along a rail. Each stepper motor is driven by a separate microstepping driver. A micrcontroller synchronized the four motors, as well as providing logic, displacement data logging, and an interface to a PC.

Each carriage had a sensitive six-axis force sensor (ATI Industrial Automation Nano17) that measures deployment force with a resolution of $3.1\,\mu\mathrm{N}$.

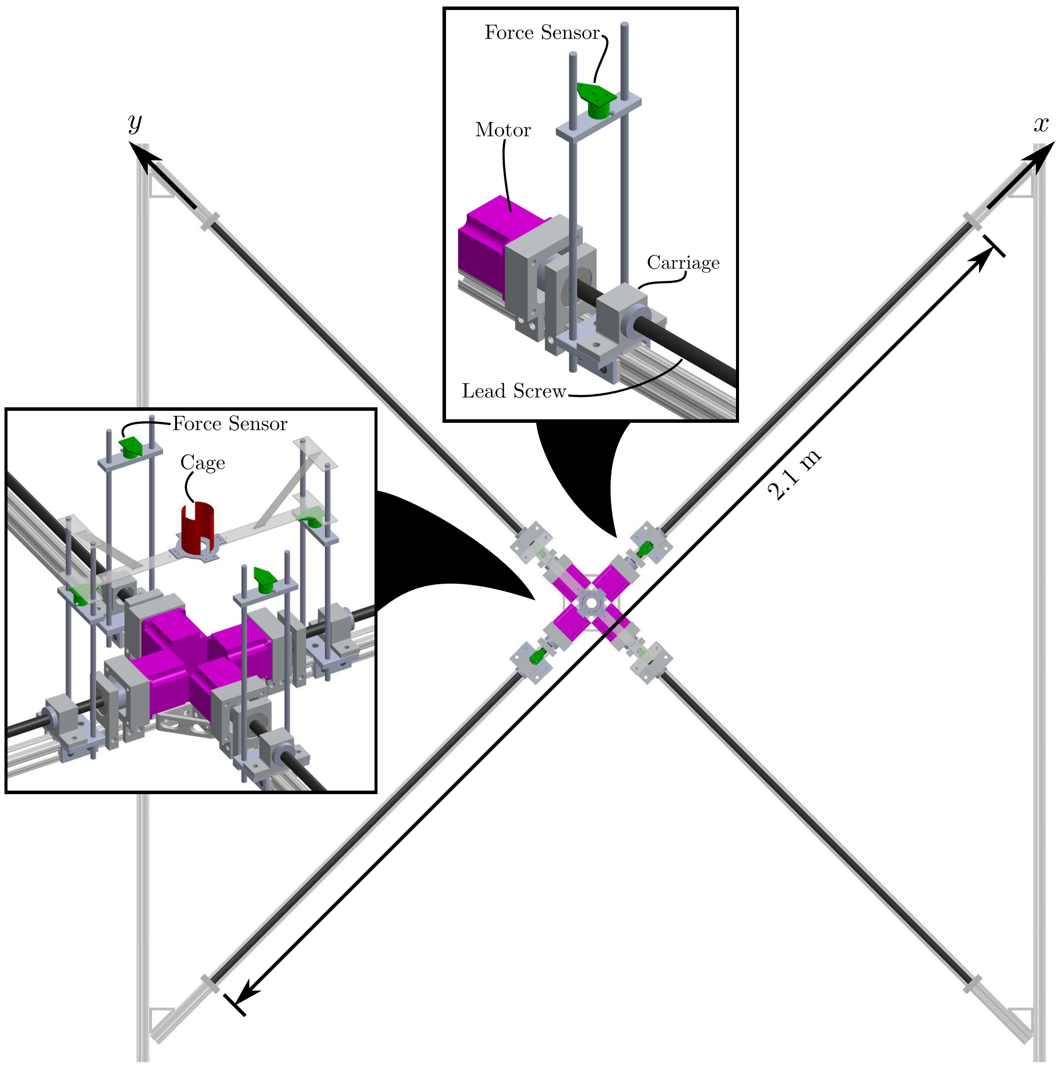

Figure 14: Two-axis deployment rig.

Figure 15 shows the cage and the clip as fabricated. The cage was made of two laser-cut acrylic base plates, $125\,\mu\mathrm{m}$-thick polyimide rectangular plates elastically bent into half-pipes, and threaded rods to attach the half-pipes to the base plates. The cage was constructed in two halves, which need to separate for the unfolding stage of the deployment. The inside faces of the half-pipes were coated with a dry lubricant to reduce friction between the cage and membrane during unwrapping.

A clip prototype was made using two paintbrush heads (7 mm × 4 mm cross section, 11 mm length) connected by a steel rod. The paintbrush bristles were pushed into the middle of the wrapped membrane stack. The membrane strips were spaced apart at this clip insertion point. This separation between the membrane strips ensured that they deployed one by one.

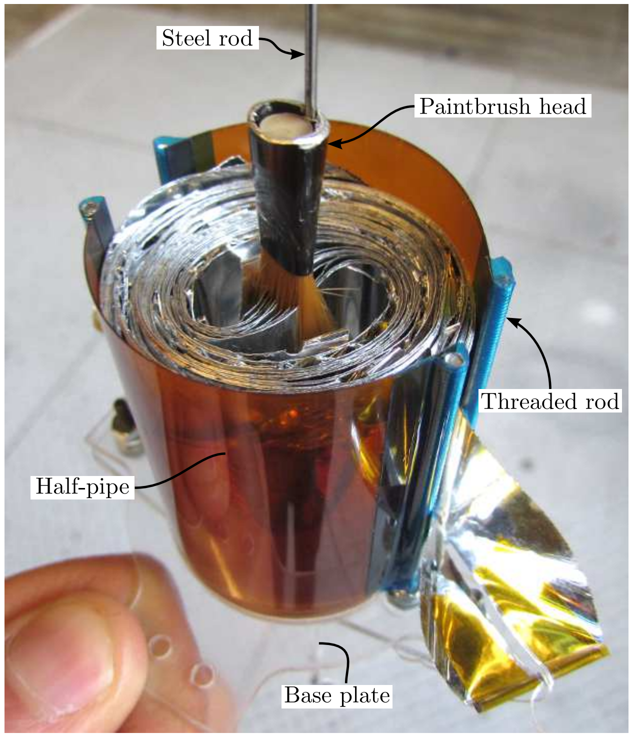

Figure 15: The cage and the clip, as fabricated. The membrane model has been wrapped and inserted into the cage with the clip. The cage half-pipes have a diameter of 37 mm and a height of 49 mm.

To simulate deployment in a 0 g environment, the clip was suspended about 0.25 m above the base of the two-axis deployment rig. Since the clip holds the middle of the membrane during most of the deployment, suspending the clip helped offload some of the weight of the membrane. A 400 g weight was suspended from the bottom of the clip to stabilize its orientation. The membrane weight was also partially offloaded at the attachment to the force sensors. The membrane was deployed in a horizontal plane. However, this setup is only an approximate gravity offload scheme, and it is expected that the measured deployment forces include a component of the membrane weight.

VII. Test Results

VII.A. Packaging Test Results

The two models listed in Table 1 were packaged according to the procedure described in Section VI.A. Their diameters at the middle of the wrapped stack, i.e. away from the ligaments and close to the restraining string, were measured and used to calculate their packaging efficiencies, which are plotted in Figure 16.

Also plotted are lines of varying λ with the same n and ψ values as the models, with ϕ such that these lines pass through the experimental points. These lines represent packaging efficiencies achievable using similar manufacturing and packaging techniques, but scaled to different λ.

VII.B. Deployment Test Results

The membrane model described in Section VI.C was deployed using the two-axis rig. The in-plane radial deployment forces $F_B, F_{B'}, F_A, F_{A'}$ were measured, and are plotted in Figure 17 with respect to the unwrapping deployment fraction $\bar{b}/b$ and the unfolding deployment fraction $\bar{a}/a$. (The in-plane transverse deployment

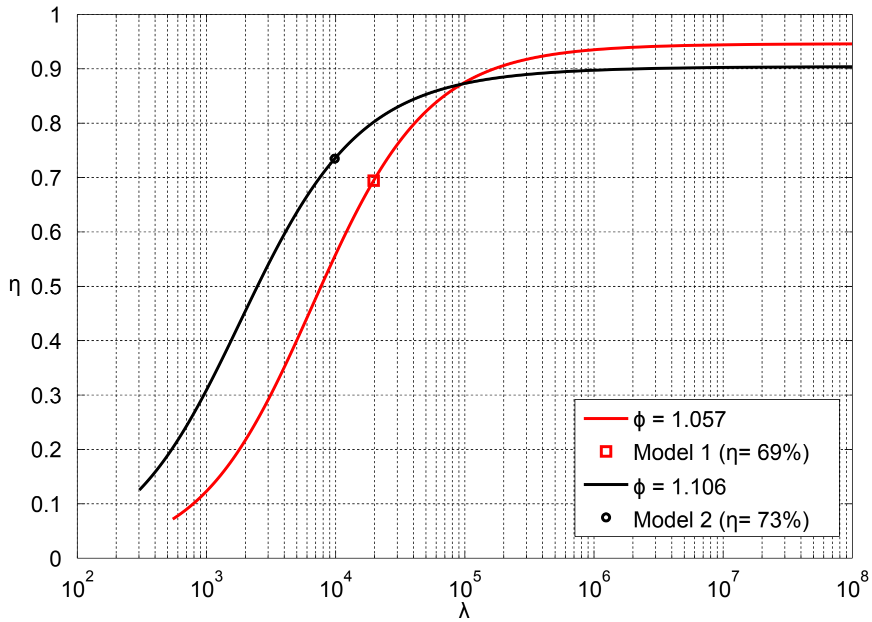

Figure 16: Packaging test results. Packaging efficiency η is plotted with respect to dimensionless deployed length $\lambda = L/h$ for the two packaging models. Also shown are the two packaging efficiency curves with the same values for n and ψ as the packaging models, with the strip thickness multiplier ϕ adjusted such that these curves pass through the experimental points.

forces were about 20 times smaller than the radial forces, and are not shown. The out-of-plane forces are primarily due to the weight of the membrane and are not shown.) The radial component of the deployment forces never exceeded 0.6 N. The deployment was displacement controlled at a rate of about $11.9\,\mathrm{mm\,s^{-1}}$.

During the unwrapping stage, the deployment forces were largely caused by friction between the wrapped membrane rotating inside the cage and rubbing against the walls of the cage. Note that during the initial stages of unwrapping, $F_{B'} \gg F_B$. This is because pulling on one end of the wrapped stack causes the other end to deploy; in a displacement-controlled deployment any lag between the two ends of the wrapped stack is persistent.

During the unfolding stage, the deployment forces F_A and $F_{A'}$ show a snapping behavior as each strip is deployed from the clip. The separation of these snaps indicates the separate (as opposed to simultaneous) unfolding of each strip. Indeed, that is what was observed: each strip was deployed separately and in sequence.

Figure 18 shows views from an overhead camera at the beginning of deployment, at the end of the unwrapping stage, during the unfolding stage, and at the end of the deployment.

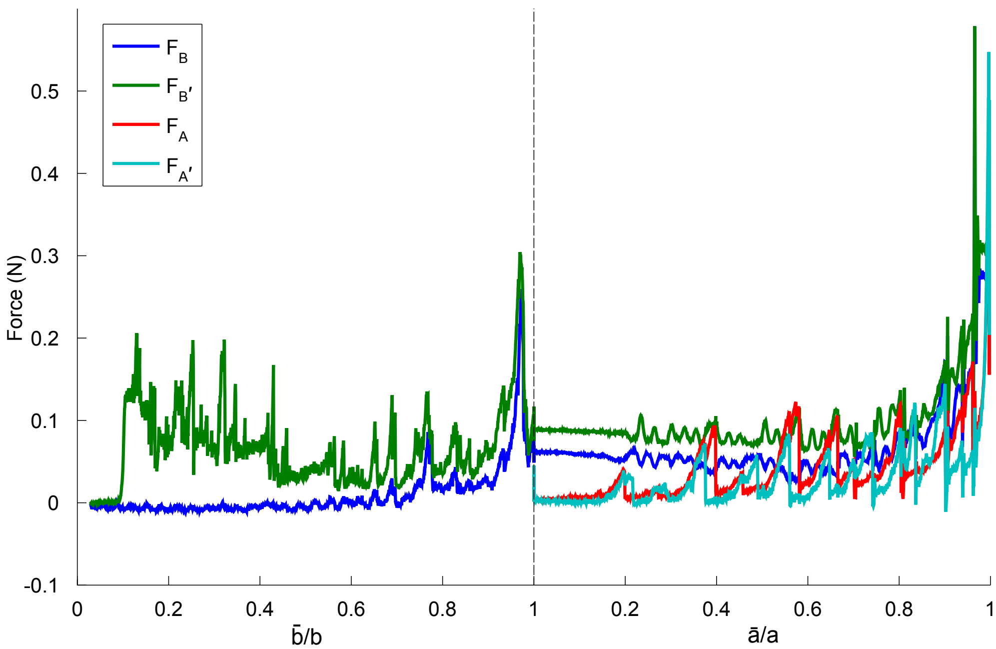

Figure 17: Deployment force profiles. $\bar{b}/b$ is the unwrapping deployment fraction and $\bar{a}/a$ is the unfolding deployment fraction. During the first stage of unwrapping, the unfolding deployment fraction $\bar{a}/a$ is fixed at 0, and during the second stage of unfolding, the unwrapping deployment fraction $\bar{b}/b$ is fixed at 1.

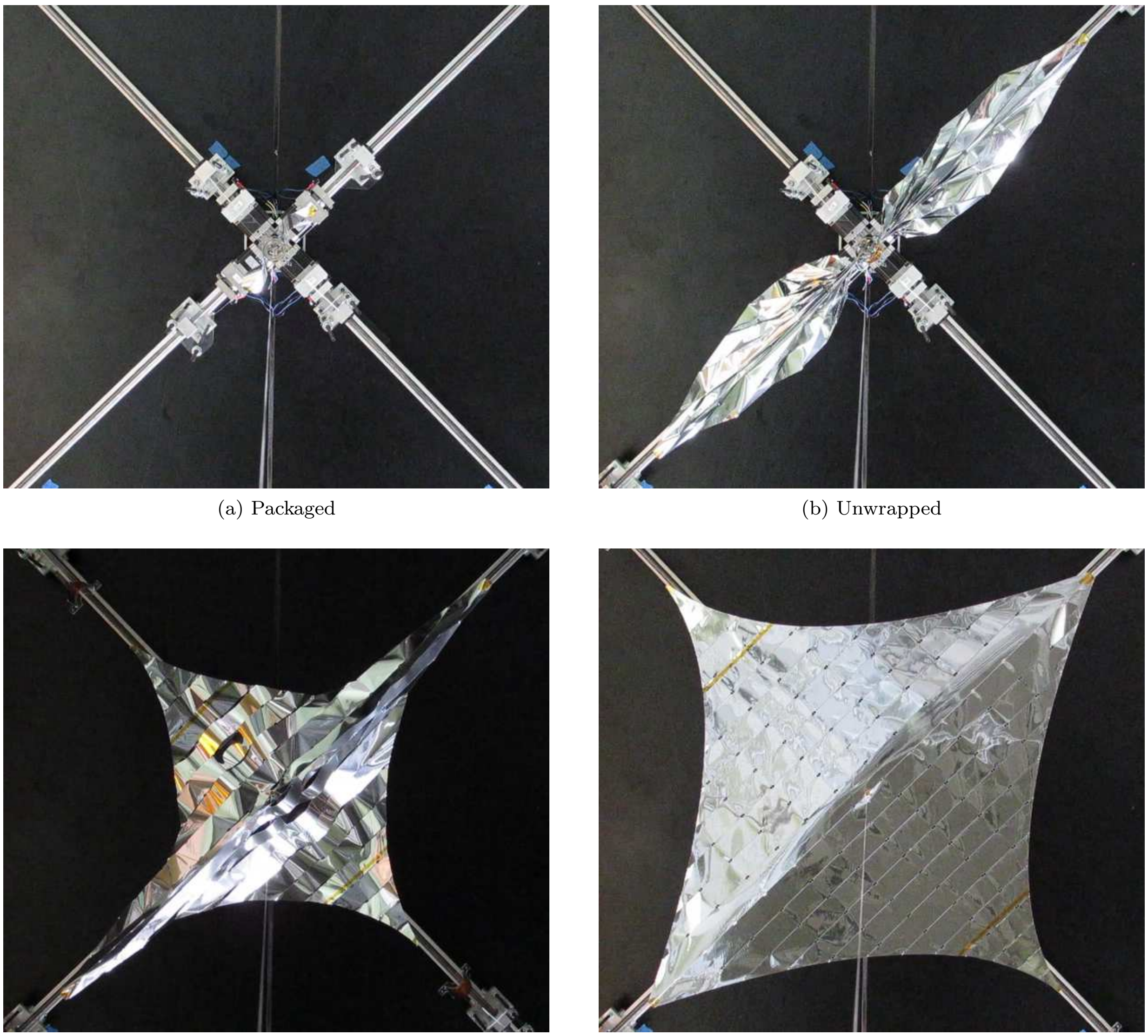

(a) Packaged (b) Unwrapped

(c) Unfolding (d) Deployed

Figure 18: Deployment test for a membrane with $a = b = 1\,\mathrm{m}$, $h = 25\,\mu\mathrm{m}$ viewed from an overhead camera.

VIII. Conclusion

A scheme for packaging thick membranes is presented that compacts the membrane along two dimensions by first folding and then wrapping the membrane. This scheme allows the membrane to be packaged tightly, with very few voids, and without plastic creases. Slipping folds are used to accommodate material thickness.

These slipping folds rely on material removal; however, realizations of slipping folds are described that allow for the transmission of tension forces across the fold lines. A two-fold symmetric wrapping scheme is described that allows for the preservation of continuity at the edges of the membrane.

A kinematic model for the wrapped membrane is used to estimate packaging efficiencies, which approaches 100% for tightly wrapped membranes with large length-to-thickness ratios. Packaging tests on 0.5 m-scale models achieved packaging efficiencies of 69% and 73%.

Also presented is a strategy for prestressing a membrane packaged using slipping folds. This strategy uses the continuous edges of the membrane to distribute radial prestress forces into uniform tension parallel to the fold lines. A 0.8 m-scale prototype was used to demonstrate the feasibility of this prestressing strategy.

A two-stage method for deploying a slip-wrapped membrane is proposed. Initial tests conducted on 1 m-scale models showed successful and controlled deployment with low unfolding forces.

Acknowledgments

Support from the Northrop Grumman Corporation is gratefully acknowledged.

N. Lee was supported through this work by a postdoctoral fellowship from the W. M. Keck Institute for Space Studies.

References

[1] Miura, K., "Method of packaging and deployment of large membranes in space," *Proceedings of the 31st Congress of the International Astronautical Federation IAF-80-A 31 Tokyo*, pp. 1–10, 1980.

[2] Miura, K. and Natori, M. "2-D array experiment on board a space flyer unit," *Space Solar Power Review*, vol. 5, pp. 345–356, 1985.

[3] Biddy, C. and Svitek, T., "LightSail-1 Solar Sail Design and Qualification," *41st Aerospace Mechanisms Symposium*, 2012, pp. 451–463.

[4] Montgomery, E. E. I. and Adams, C. L., "NanoSail-D," *CubeSat Developer's Workshop*, 2008.

[5] Furuya, H., Mori, O., Okuizumi, N., Shirasawa, Y., Natori, M. C., Miyazaki, Y., and Matunaga, S., "Manufacturing and Folding of Solar Sail IKAROS," *52nd AIAA/ASME/ASCE/AHS/ASC Structures, Structural Dynamics, and Materials Conference*, Apr. 2011.

[6] Lee, N. and Close, S., "Curved pleat folding for smooth wrapping," *Proceedings of the Royal Society A: Mathematical, Physical and Engineering Sciences*, vol. 469, issue 2155, 2013.

[7] Satou, Y. and Furuya, H., "Fold Line Based on Mechanical Properties of Crease in Wrapping Fold Membrane," *54th AIAA/ASME/ASCE/AHS/ASC Structures, Structural Dynamics, and Materials Conference*, Apr. 2013.

[8] Murphey, T. W., *A nonlinear elastic constitutive model for wrinkled thin films*, Ph.D. thesis, 2000.

[9] Papa, A. and Pellegrino, S., "Systematically Creased Thin-Film Membrane Structures", *Journal of Spacecraft and Rockets*, Vol. 45, No. 1, 2008, pp. 10-18.

[10] Tachi, T., "Rigid-Foldable Thick Origami," *Origami 5*, edited by M. Yim, 2011, pp. 253–263.

[11] Guest, S. D. and Pellegrino, S., "Inextensional wrapping of flat membranes," *First International Seminar on Structural Morphology*, Sept. 1992, pp. 203–215.

[12] Zirbel, S. A., Lang, R. J., Thomson, M. W., Sigel, D. A., Walkemeyer, P. E., Trease, B. P., Magleby, S. P., and Howell, L. L., "Accommodating Thickness in Origami-Based Deployable Arrays," *Journal of Mechanical Design*, Vol. 135, Nov. 2013, pp. 111005.

[13] Reynolds, W. D. and Murphey, T. W., "Elastic Spiral Folding for Flat Membrane Apertures," *55th AIAA/ASME/ASCE/AHS/ASC Structures, Structural Dynamics, and Materials Conference*, Jan. 2014.

[14] Hoberman, C., "Reversibly Expandable Structures," United States Patent No. 4,981,732, 1991.

[15] Trautz, M. and Künstler, A., "Deployable folded plate structures folding patterns based on 4-fold-mechanism using stiff plates," *Proceedings of the International Association for Shell and Spatial Structures Symposium*, pp. 2306–2317, Oct. 2009.

[16] Greschik, G., "Deployment of Dishes with Surface Discontinuities," *Journal of Spacecraft and Rockets*, Vol. 33, No. 4, 1996.

[17] Tibbalds, B., Guest, S. D., and Pellegrino, S., "Inextensional Packaging of Thin Shell Slit Reflectors," *Technische Mechanik*, Vol. 24, No. 3-4, 2004, pp. 211–220.

[18] Reynolds, W. D., Murphey, T. W., and Banik, J. A., "Highly Compact Wrapped-Gore Deployable Reflector," *52nd AIAA/ASME/ASCE/AHS/ASC Structures, Structural Dynamics, and Materials Conference*, Apr. 2011.

[19] Spivak, M., *A Comprehensive Introduction to Differential Geometry*, Vol. II, 3rd ed., 1999.